FACULTEIT WETENSCHAPPEN

DEPARTEMENT
NATUURKUNDE EN STERRENKUNDE

LABORATORIUM VOOR
VASTE-STOFFYSICA EN MAGNETISME

KATHOLIEKE
UNIVERSITEIT
LEUVEN

Nanoscale Characterization and Modification of the Electronic Properties of Hydrogen Terminated Diamond Surfaces

Promotoren:
Prof. dr. Chris Van Haesendonck
Dr. Alexander Volodin

Proefschrift ingediend tot het
behalen van de graad van
Doctor in de Wetenschappen
door:

Cristina Toma

2008

ISBN 978-90-8649-206-0
D/2008/10.705/53

Acknowledgments

Even though there is only one author on the cover of this book, this thesis is the result of a few years of work, during which I have been accompanied and supported by many people. It is a pleasure to convey my gratitude to all those who helped me to complete this thesis.

First I would like to express my gratitude and appreciation to my supervisor, Prof. Chris Van Haesendonck, whose guidance and encouragement throughout the course of this thesis was invaluable.

I am also indebted to my co-supervisor Dr. Alexander Volodin, whose enthusiasm and ability to explain things clearly and simply made my life so much easier. He was an inspiration and provided great support and company in all these years. I would have been lost without him.

A special thanks goes to Prof. Yvan Brunseraede for giving me the opportunity to come to Leuven for this PhD.

To the members of the jury (Prof. K. Temst, Prof. V. Afanasiev, Prof. C.F.J. Flipse, Prof. M. Nesládek and Dr. K. Haenen), I would like to express my deepest gratitude for their effort in reading this thesis and providing valuable comments and suggestions.

A big thank you goes to Anna, Wim, Vincent, Michaël and Andrada from Institute for Materials Research (IMO) Hasselt for providing me with the diamond samples.

I furthermore would like to thank Bas for his endless support regarding the MBE work. I am very grateful for the administrative assistance from Monique, Liliane and Wim.

There are a number of former colleagues, who have enriched my professional life in many ways, that I would like to thank. My colleagues from Scanning Probe Microscopy group: Alexander, Dieter, Elena, Fernando, Hugo, Jyoti, Johan, Koen, Maarten, Manish, Nele, and specially to my office colleagues Steven, Stijn and Tom and all the others who I have forgotten to mention here.

I can not end these acknowledgments without thanking my family, their encouragement and love have been a constant throughout my life. Mama, tata vă mulţumesc din suflet pentru tot ce aţi făcut pentru mine!

Finally, I want to express my profound gratitude to my dearest Doru for his moral support, patience guidance and love during my work.

To him I dedicate this thesis...

Cristina Toma
October 2008

Contents

Introduction

Diamond is a very special material with many interesting properties, which continue to receive a lot of attention. Hydrogen-terminated diamond is very attractive for devices based on surface electronics due to the presence of a highly conductive *p*-type layer that is confined to the surface. A quasi two-dimensional (2D) hole gas is created with a typical sheet resistance of $100\,\mathrm{k}\Omega$. Electrical characterization of patterned surface structures is crucial to investigate device applications of the hydrogen-terminated diamond surfaces.

The goal of the thesis is to pattern the hydrogen-terminated diamond surfaces and to characterize the electronic properties of the fabricated conductive structures. We combine photolithography and local anodic oxidation, using an atomic force microscope (AFM), in order to pattern hydrogen-terminated diamond surfaces down to the nanometer scale. Local anodic oxidation (LAO), which is induced by the tip of the AFM, is an effective way to modify the electronic properties of various conductive surfaces with nanometer resolution by the local creation of an oxide. Surface transport properties for surface structural and electrical characterization, such as AFM, electrostatic force microscopy (EFM) and scanning tunneling microscopy (STM) are used. Valuable information about local properties of the diamond films and fabricated structures was obtained at wide scale range down to atomic scale.

The thesis consists of four chapters. The first chapter is a general overview of the material studied in this work. First, we analyze the structural properties of bulk diamond and of its surface. Next, we consider the hydrogen terminated diamond surface and its properties as a semiconductor material. Finally, we discuss the specific properties of diamond and its industrial applications.

In the second chapter the experimental techniques used to modify and to characterize the hydrogenated diamond samples are reviewed. The techniques used in this thesis for creating submicrometer structures on the conductive diamond surface (photolithography and local modification with an atomic force microscope) are considered in detail. The last section is devoted to describing the technique used to study the electric transport properties of the created patterns.

Chapter 3 presents the experimental results we have obtained using scanning probe microscopy techniques. We have used STM in ultra-high vacuum as an ideal tool for studying the properties of the hydrogenated diamond surface at the atomic level. We have characterized the hydrogenated diamond surface in order to optimize the preparation procedure of the samples suitable for large and small scale lithography, and for creating submicrometer structures used for further electrical characterization.

In the last chapter we describe the fabrication of conductive structures on hydrogen terminated diamond surfaces. By combining photolithography and local AFM modification submicrometer structures have been created. The conductive properties of the obtained structures have been investigated using EFM. Finally, electric transport measurements have been performed in order to study the electronic properties of the created structures and 2D hole gas characteristics at the diamond hydrogenated surface.

Chapter 1

Diamond from carbon to semiconductor

1.1 Introduction

Diamonds were formed thousands of years ago deep in the earth, under huge heat and pressure conditions. Then the volcanic eruptions brought the diamonds to the surface and scattered them along rivers. Apparently, the first river bed diamonds were discovered in India, around 800 B.C.

Nowadays, diamond is not only a famous gemstone, but also a very promising 'wide band gap' semiconductor that may one day rival silicon as the material of choice for high power and high frequency electronics. The mechanical, optical and electronic properties of diamond are in many respect outstanding. Its thermal conductivity of $20\,\mathrm{Wcm^{-1}K^{-1}}$ at room temperature is the highest known for any material, and many of its electronic properties (electric breakdown field, dielectric constant and saturation drift velocity) make it an ideal semiconductor. The surfaces of diamond exhibits a number of features that are unique among all semiconductors. The rarity of diamond largely prevents its exploitation as a technical material. With the invention of synthetic diamond growth techniques at high pressure and temperature (HPHT) in the 1950s, diamond became available in large quantities and was used mainly for mechanical applications. But it was the discovery of a chemical vapor deposition (CVD) process in 1981 that laid the basis for diamond as a material for electronics.

The basic requirements for diamond electronics have now been met and progress in growth, doping and characterization of diamond has provided the tools for an efficient further development as a semiconductor.

1.2 Diamond as carbon

Carbon (C) is the sixth most common element in the universe. It is a very special element because it plays an essential role in the chemistry of life. We can find carbon in nature in three allotropic forms: amorphous, graphitic and diamond. A fourth allotrope of carbon was produced in the late 60's. It is a transparent material and it is called “white carbon” [1]. Each allotropic form has very different physical and chemical properties. E.g., graphite is soft, opaque and electrically conducting, while diamond is hard, transparent and electrically insulating. This makes carbon very special and fascinating.

1.2.1 The amorphous carbon structure

The amorphous structure is characterized by the absence of long range order. In this structure there is no periodicity at long range, hence its symmetry is broken, giving isotropic characteristics to the structure. However, there is a short range order present, which can be seen in bond length, number of nearest neighbor atoms and in the angle between two bonds. Because the atoms in the amorphous structure are not bonded ideally, the energy of the amorphous structure is higher than that of a pure crystal.

There are two specific forms of amorphous carbon that can appear. They can be identified by their microscopic and macroscopic properties:

1. Diamond-like amorphous carbon (DLC), is characterized by a mean number of nearest neighbors $z = 3.5 - 3.8$, mean bond angle of $110 - 115\,^\circ$ and density of $2.9 - 3.5\,\mathrm{g/cm^3}$. It is usually denoted by *ta*-C. Because of the sp^3 fraction present within the amorphous matrix, it exhibits several interesting properties: high mechanical hardness, infrared transparency and chemical inertness. In the case of sp^3 rich *ta*-C, this amorphous structure has the hardness and elastic modulus comparable to crystalline diamond [2, 3].

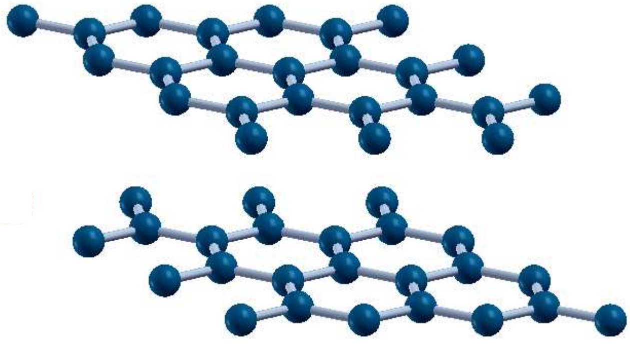

Figure 1.1: Graphene layers of the graphite structure

2. Graphite-like amorphous carbon, which is denoted by *a*-C, is characterized by a high percentage ($\approx 70\% - 98\%$) of sp^2 bonds. As a result it has a mean number of nearest neighbors, $z = 2.9 - 3.2$, a bond angle of around 120° and a density of $2.0 - 2.7\,\mathrm{g/cm^3}$. This amorphous form of carbon is soft, opaque and is mostly made of distorted sp^2 bonds [4].

1.2.2 The graphite structure

Graphite is an allotropic form of carbon consisting of layers of hexagonally arranged carbon atoms (graphene layers) in a planar condensed ring system (Fig. 1.1). The layers are stacked parallel to each other with three-dimensional crystalline long-range order. The chemical bonds within the layers are covalent with sp^2 hybridization (see Fig. 1.2). The layers are held together by weak van der Waals forces. The bond between the atoms within a layer is stronger than the bond of diamond, but the force between two layers of graphene is weak. Therefore, layers can slip over each other, making it soft. Graphite is a semimetal [5]. At absolute zero its valence band is filled, its conduction band is empty, but the energy gap is zero. However, at higher temperatures there are mobile electrons in its conduction band and mobile holes in its valence band. These charge carriers are not responsible for its bonding, as in a metal, but they are responsible for the semimetallic luster of graphite. The layered structure of graphite allows electrons to move easily within the layers and this permits graphite to conduct electricity and heat and also to absorb the light of

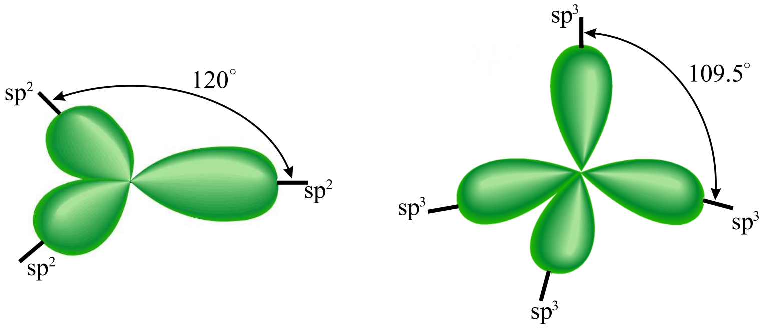

Figure 1.2: sp^2 and sp^3 hybrid orbitals

all wavelengths (giving its black color).

In 2004, K. Novoselov and co-workers [6] developed techniques to separate individual graphene flakes from graphite crystals. Since the first reports of experiments on stand-alone, single layer graphene crystals, this remarkable two-dimensional material has attracted great scientific interest. Graphene sheets offer extraordinary electronic, thermal and mechanical properties and are expected to find a variety of applications.

1.2.3 The diamond structure

The crystal structure that diamond adopts is named after it. In the diamond lattice (Fig. 1.3), each carbon atom has four valence electrons in the s and p orbitals. The s orbital mixes with the three p orbitals (p_x, p_y, and p_z) forming sp^3 hybridization (Fig. 1.2). The four valence electrons of the carbon are equally distributed among the sp^3 orbitals, each orbital pointing to one of the corners of a tetrahedron. This tetrahedral structure gives strength and stability to the bonds. The diamond structure can be viewed as two interpenetrating face-centered cubic (FCC) structures displaced by $(1/4, 1/4, 1/4)\,\mathrm{a}_0$, where a_0 is the cubic lattice constant. For carbon diamond $\mathrm{a}_0 = 3.567\,\text{Å}$ [7]. The distance between nearest neighbors is 1.545 Å. In the diamond structure all valence electrons contribute to the covalent bond. Because the valence electrons are not free to move through the crystal, diamond is a poor conductor with a band gap of 5.48 eV [8].

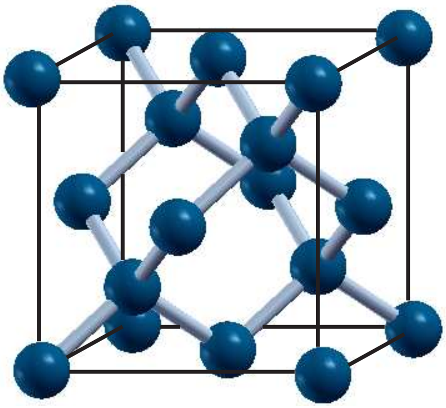

Figure 1.3: The diamond structure

Diamond can also adopt a (2H) hexagonal crystal structure, called lonsdaleite. However, this polymorph, discovered in 1967 [9], is extremely rare in nature.

1.2.4 Classification of diamond

The gemstone diamonds are classified according to "the four Cs": cut, clarity, color, and carat. The diamond samples can be classified according to their content and type of nitrogen impurities. "Type I" diamonds contain a significant amount of nitrogen impurities. This type represents the large majority of all natural diamonds. "Type II" diamonds contain a very small amount of nitrogen impurities, which is not detectable by ultraviolet or infrared absorption measurements. There are four types of natural diamond:

98% of natural diamond is *Type Ia*. It contains up to 0.1% nitrogen in small aggregates or platelets that strongly absorb ultraviolet light below 320 nm. This type of diamond has a thermal conductivity less than 9 W/(cmK) at 25°C and its electrical resistivity is greater than $10^{14}\,\Omega$m. The industrial synthetic diamond is usually of *Type Ib*. It contains up to 0.2% nitrogen dispersed throughout the crystal. That is why this type has a yellow color in case of low nitrogen concentrations or shades of green for higher concentrations. *Type IIa* diamond is almost free of nitrogen. It is colorless and has the best optical and thermal properties of all diamond types. This type transmits light at all wavelengths longer than 225 nm (except for some absorption in the $3-5\,\mu$m region) and has a thermal conductivity near 20 W/(cmK) at 25°C. *Type IIb* diamond is also free of nitrogen, but contains small quantities of boron. Because of this it has a blue color and *p*-type conductivity, with a resistivity of $0.1-100\,\Omega$m.

1.2.5 Properties and applications of diamond

Diamond is material that exhibits a large number of exceptional properties (Table 1.1). As a result, it has a great potential for use in many industrial and commercial applications. In the following we will describe some of the applications where the properties of diamond play a key role.

Table 1.1: Properties of bulk diamond.

Property	Value	Units	Reference
Hardness	10000	kg/mm^2	[10]
Density	3.52	g/cm^3	[10]
Thermal conductivity	2000	W/(m·K)	[10]
Dielectric constant	5.7	–	[10]
Electronic bandgap (300 K)	5.45	eV	[11]
Electron mobility (300 K)	2200	$cm^2/(V\cdot s)$	[10]
Hole mobility (300 K)	1600	$cm^2/(V\cdot s)$	[10]
Resistivity	$10^{13}-10^{16}$	Ω/cm	[10]

Diamond is an extremely hard material. This makes it an ideal candidate for use in *cutting tools* for machining non-ferrous metals, plastics, chip-board and composite materials. By coating CVD diamond directly onto the surface of the tungsten carbide tool-pieces, one can obtain tools that have a longer life and cut faster than the conventional cutting tools [12, 13]. Furthermore, the new composite metals used in aerospace and automobile industries (such as Al/Si), being extremely difficult to shape with conventional materials, are very good candidates for diamond-coated cutting tools.

When designing modern high power electronic devices one faces the problem of overheating, due to the production of large amounts of heat in a small area. For cooling these devices it is essential to be able to spread the heat flux. This is done by placing a layer of high thermal conductivity between the device and the cooling system, such as a fan or heat sink. Since diamond has a thermal conductivity (due to phonons) better than copper over a wide temperature range and it has the advantage of being an electrical insulator, this material can be used for a variety of *thermal management applications.* These include submounts for integrated circuits [14], heat spreaders for high-power laser diodes [15], or as a substrate material for multi-chip modules [16].

Due to its special optical properties, diamond is also used for *optical applications.* Conventional infrared materials, especially in the $8-12\,\mu$m wavelength range (such as ZnS, ZnSe and Ge), have the disadvantage of being brittle and being easily damaged. On the contrary, diamond with its high transparency, durability and resistance to thermal shock, is an excellent material for such applications.

The surface acoustic wave (SAW) devices are electronic devices that can use impure, thin polycrystalline CVD diamond. E.g., using a SAW filter one can transform radio frequency electronic signals into mechanical vibrations, and vice versa [17]. They are used in the communications industry, where high frequency radio waves need to be generated by electronic circuits, and subsequently broadcasted by a transmitter. The limiting factor in the SAW devices is the maximum speed of propagating the signals through the device. This depends mainly upon the speed of sound (the acoustic wave) along the surface of the device material. For high-performance devices, a SAW material which can operate at 10 GHz or higher frequencies is needed. Diamond is therefore a good candidate.

Diamond can be also used in *particle detectors* for ultraviolet (UV) light and high energy particles, such as alpha- and beta-particles or neutrons. Moreover, diamond can be used as a replacement for Si to detect high energy particles in the next generation of particle accelerators [18, 19]. Since diamond has a similar response to damage by X-rays and gamma-rays as the human tissue, it can be also used for *medical applications*, e.g, as a dosimeter for radiation exposure.

1.3 Diamond surface reconstructions and surface states

The (100) and (111) surfaces are the two most important surfaces for diamond, because they constitute the exposed crystal faces of polycrystalline CVD diamond films and can be selectively grown by CVD when process parameters are controlled appropriately.

1.3.1 The diamond (100) surface

One of the most important crystallographic surfaces of CVD diamond is the (100) surface. Quasi-heteroepitaxial diamond films with smooth (100) surfaces can be deposited on silicon [20], silicon carbide [21] or iridium [22]. Moreover, the homoepitaxial growth of diamond is much less susceptible to incorporation of stacking faults or creation of twin crystals in case of the (100) surface when compared to the (111) surface.

The clean diamond (100) 2×1 surface

The bulk terminated (100) surface has two dangling bonds per surface carbon atom and because of this fact the (100) surface is unstable. The energy of the clean surface is lowered by forming π-bonded dimers between nearest neighbors [23]. The new surface exhibits two (2×1) reconstructed domains that are rotated by $90\,^\circ$ (Fig. 1.4-(a)). The surface dangling bonds couple to π-bonded dimers and this induces a bonding-antibonding splitting between occupied and unoccupied (dimer) π-orbitals. The dimers are arranged in rows, along the [011] direction and interact with each other. This leads to a further weaker splitting of the dimer orbitals, and finally the surface band structure with an occupied band originating from the π-(bonding) orbital and an empty band originating from the π^*-(antibonding) orbital is formed. Because of the rather large distance of 2.52 Å between the surface dimers, their mutual interaction, which broadens the π- and the π^*-bands, leaves a gap of 1.3 eV between occupied and unoccupied surface states. As a result, the surface is semiconducting [24]. The occupied and unoccupied surface states are placed energetically within the valence band, they do not extend into the band gap of diamond. Therefore, they are electronically inactive, since they are not able to exchange electrons or holes with the diamond bulk. The surface band structure of the occupied surface states of the diamond (100) surface was also measured by photoemission spectroscopy [25] and found to be in good agreement with theory.

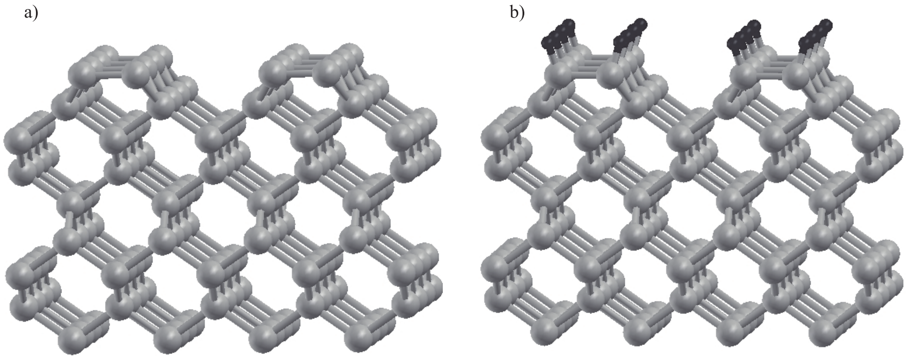

Figure 1.4: Perspective views of the atomic geometries for: (a) the clean (100) 2×1 reconstructed surface; (b) hydrogenated (100) 2×1 reconstructed surface.

The hydrogen terminated diamond (100) 2×1:2H surface

Hydrogen is the most important adsorbate by which diamond surfaces can be terminated and is the dominating species in the CVD growth process of diamond. CVD diamond surfaces can be found in the hydrogen terminated state if the deposition process is appropriately ended. However, in the case of diamond hydrogen does not lead to a stabilization of the bulk terminated 1×1 structure as in the case of other group IV semiconductors. It has been shown from total energy calculation [26, 27] that this is because of the steric repulsion of the hydrogen atoms due to the tight diamond lattice, which prevent the complete saturation of all surface dangling bonds. Consequently, in the case of diamond, the surface atoms remain arranged in dimer rows and only the π-bond between the dimer atoms is replaced by a covalent bond to one hydrogen at each surface atom (Fig. 1.4-(b)). The change in bonding structure leads to the replacement of the π and π^*-states of the clean surface by bonding and antibonding states of the carbon-hydrogen bonds. Moreover, the corresponding surface state bands are shifted in energy further into the valence band and towards the conduction band, respectively. Density functional theory calculations [24] have found that the occupied states are found more than 2 eV below the valence band maximum (VBM), while the unoccupied surfaces states are predicted between 3.3 eV and 6.0 eV above the VBM. The fact that the occupied surface states are not present in the band gap of diamond (100) 2×1:2H is also confirmed

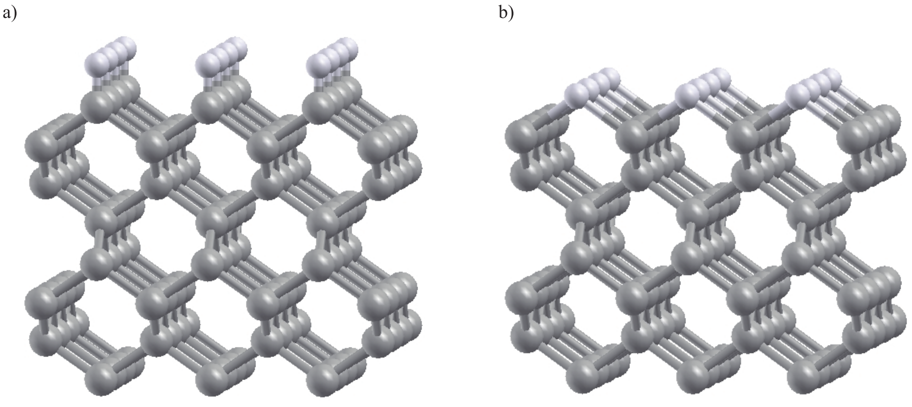

Figure 1.5: Perspective views of the atomic geometries for: (a) Kethone (C=O) configuration; (b) Ether (C−O−C) configuration

by photoemission spectroscopy [25].

The oxygen terminated diamond (100) 1×1:O surface

Another important adsorbate termination of diamond surfaces is by oxygen. Oxygen induces significantly different electron affinities and work functions compared to hydrogen. It is often used to locally remove the high surface conductivity (SC) of hydrogenated diamond. Being a divalent atom, oxygen can saturate two surface dangling bonds simultaneously. Therefore, for a full covalent termination of the surface only half the density of adsorbates atoms than for hydrogen is required. In the case of oxygen atoms steric repulsion does not hinder the stabilization of the bulk terminated 1×1 structure, found experimentally by Reflection High Energy Electron Diffraction (RHEED) [28] and by Low Energy Electron Diffraction (LEED) [29] measurements.

Two theoretical models have been proposed in order to explain the bonding structure of the diamond (100) 1×1:O surface. The first model, called *ketone* or top side model (Fig. 1.5-(a)), assumes that one oxygen atom is double bonded to each carbon surface atom. On the other hand, the *ether* or bridge side model (Fig. 1.5-(b)) claims that the oxygen atoms connect adjacent surface carbon atoms. The oxygen chemisorption energy obtained from total energy calculations is very similar for both models (8.57 vs. 8.43 per atom) [30]. However, the LEED I-V characteristics [29] and the electron affinity [31] fit clearly better to the ether model. Moreover, photoemission spectroscopy reveals no occupied surface states in the gap, but clearly one at about 3 eV below the Fermi level of a boron doped type *IIb* single crystal. This experimental result fits better the ether than the ketone model when compared to the density functional theory calculations [28].

1.3.2 The diamond (111) surface

The (111) surface of diamond can be bulk terminated with either one or three dangling bonds per surface atoms. The one dangling bond surface is the natural cleavage plane of diamond, while the three dangling bond surface cannot be prepared from volume crystals because of the high formation energy needed for breaking three bonds. Although in one scanning tunneling microscopy (STM) experiment it was observed that a 1×1 methyl saturated one dangling bond surface (which is equivalent to a trihydride passivated three dangling bond surface) may occur locally during heteroepitaxial growth or after plasma hydrogenation [32], theoretical calculations have shown that the three dangling bond surface should undergo characteristic reconstructions depending on the degree of hydrogen coverage [33].

The clean diamond (111) 2×1 surface

Because the bulk terminated structure is not stable for the clean diamond (111) surface, it undergoes a rather complicated 2×1 reconstruction (Fig. 1.6-(a)). This reconstruction was first suggested in the case of Si (111) [34]. However, in contrast to the Si (111) surface, in the case of diamond (111) the surface atoms do not dimerise along the chains and also there is no buckling within the surface and between the second layer atoms [35]. The reconstructed surface has a lower symmetry compared to the bulk terminated one, only one reflection plane is maintained.

The occupied surface states extend into the gap up to 0.4 eV above the VBM, but leave a gap of at least 0.5 eV to the unoccupied surface states, in contrast to the clean diamond (100) 2×1 surface. The occupied, donor-like surface states of the perfect C(111) 2×1 surface are expected to create hole depletion and a weak downward surface band bending or *p*-type bulk material.

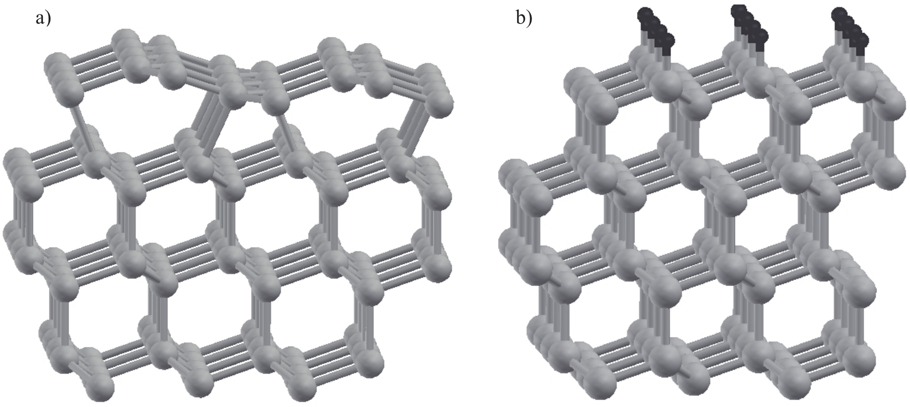

Figure 1.6: Perspective views of the atomic geometries for: (a) the clean (111) 2 × 1 Pandey chain surface, where the top two rows of C atoms form zig-zag chains; (b) hydrogenated (111) 1 × 1 surface without reconstruction.

The hydrogen terminated diamond (111) 1 × 1:H surface

The hydrogen termination of the surface dangling bonds stabilizes the diamond (111) surface without any noticeable relaxation of the carbon atoms (Fig. 1.6-(b)), in contrast to the (100) surface. Due to the formation of the covalent carbon-hydrogen bonds, which have a length of 1.1 Å, bonding states appear inside the valence band at around 4 eV below the VBM. Photoemission experiments show no occupied surface states within the gap in agreement with the calculations. Regarding the unoccupied, acceptor-like surface states, theoretical calculations predict antibonding C-H bands between 3.6 and 6.0 eV above the VBM [35].

The oxygen terminated diamond (111) 2 × 1:O surface

There are few results concerning the oxygen terminated surface reported so far [36]. Oxygen can be chemisorbed on the clean as well as on the hydrogen terminated diamond (111) surface. However, the oxidation of a hydrogenated surface is much easier than vice versa, i.e., the hydrogenation of an oxidized surface [36]. Even at monolayer coverages oxygen does not cause the de-reconstruction of the surface. In contrast to hydrogen, it keeps the 2 × 1 ge-

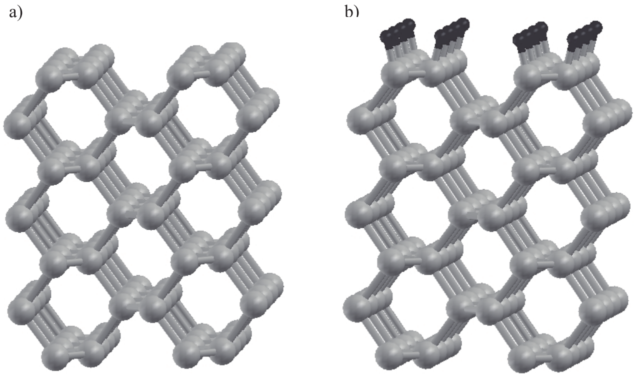

Figure 1.7: Perspective views of the atomic geometries for: (a) the clean (110) 1 × 1 surface without reconstruction; (b) hydrogenated (110) 1 × 1 surface without reconstruction.

ometry of the clean surface. Although ultraviolet photoemission spectra show no indication for donor-like surface states in the gap, clear surface resonances can be found at 4.2 and 8.4 eV below the VBM [36].

1.3.3 The diamond (110) surface

The bulk terminated (110) surface consists of zigzag chains of surface atoms. Each atom carries one dangling bond and forms one back bond to a second layer zigzag chain running parallel to the chain of surface atoms.

The clean diamond (110) 1 × 1 surface

The first two atomic layers of the bulk terminated (110) surface are very similar to the 2 × 1 reconstructed (111) surface. The zigzag chains present in the case of the (110) surface replace (Fig. 1.7-(a)) the Pandey chains of the 2 × 1 reconstructed (111) surface. Moreover, the interatomic distances between the surface atoms are similar. Within a chain the nearest neighbor distance and thus the separation between the surface dangling bonds is just the bond length 1.545 Å of the diamond lattice.

Total energy calculations have shown that only a slight relaxation of the surface occurs. This relaxation straightens the surface chains and reduces the distance between surface atoms by about 7%, which is almost the same values as for diamond (111) 2×1 [37].

The hydrogen terminated diamond (110) 1×1:H surface

Although the hydrogen termination of the diamond (110) surface maintains the 1×1 geometry [38], it reduces the relaxation of the clean surface significantly (Fig. 1.7-(b)). The distance between surface atoms is reduced by 1.7% when compared to the bulk-terminated structure. Band structure calculations and photoemission did not find occupied (donor-like) surface states in the gap. Similar to the case of the other diamond surfaces, hydrogen provides the passivation of the (110) surface for p-type bulk material, but leaves electronically active surface states on n-type diamond.

1.4 Diamond as a semiconductor

The properties of the diamond surface are of fundamental importance for its potential electronic applications. These properties depend on the kind of passivation of the surface dangling bonds, which can be done either by chemisorbed adsorbates or by the formation of mutual chemical bonds as a consequence of surface reconstruction. Specific surface states in the gap of the semiconductor are formed at the surface, depending on the kind of surface termination. They have the capability of accommodating extra electrons or holes extracted from the bulk of the material. As a result, we can distinguish two different kind of surface states. On one hand, there are the surface states, which are capable of capturing valence band holes, and are called donor-like. These states are present in the case of an intrinsic bulk material. On the other hand, we have the surface states which are normally unoccupied. They are electronically inactive for p-type material, but can act as electron traps at the surface in n-type devices. These surface states are called acceptor-like.

Another category of important electronic states within the band gap of a semiconductor are the surface defects. They are in general not only localized perpendicular to the surface, but also to a certain extent laterally. A typical example of such a surface defect is the dangling bond which may exist as an isolated species within the neighborhood of adsorbate-saturated surface bonds.

A special feature of diamond is related to the charge carriers. The carriers can not only be depleted in a subsurface region of p-doped diamond by the presence of the surface, but also the opposite effect can be observed in the case of hydrogen terminated surfaces: a hole accumulation layer. This hole accumulation layer leads to a very pronounced surface conductivity.

1.4.1 Electron affinity

The diamond surfaces have the ability to show a negative electron affinity (NEA) when appropriately terminated. The concept of electron affinity (EA), which is caused by a polarization of surface bonds, and its dependence on the surface properties can be easily mixed up with the phenomenon of surface band bending (see next section), which appears due to an exchange of free charge between states at the surface and a space charge layer extending into the bulk.

If we ignore the electron-electron interaction inside the semiconductor and consider a semi-infinite semiconductor lattice together with a semi-infinite vacuum, we define the electron affinity as the energy separation between the lowest unoccupied state with a delocalized wavefunction inside the solid, and the lowest unoccupied state with a wavefunction delocalized inside the vacuum part of the heterosystem. The eigenstate with the higher energy will have a delocalized wavefunction both in vacuum and semiconductor. The eigenstate with the lower energy will have a wavefunction exponentially decaying in one of the two components. In the case of positive electron affinity (PEA) the state with the lower energy corresponds to a state at the conduction band minimum (CBM) with a wave function decaying exponentially into vacuum, while for the case of negative electron affinity it corresponds to a free electron with zero kinetic energy (i.e. the vacuum level) and a wave function exponentially decaying into the semiconductor.

The appearance of an electrostatic dipole layer at the interface of the heterosystem vacuum/semiconductor will induce an additional step potential. One can see from basic electrostatics that the energy step ΔE of that potential is

$$\Delta E = \frac{enp}{\varepsilon_0}, \tag{1.1}$$

where n, p, e and ϵ_0 are the lateral density, the moment of the dipoles, the elementary charge and the vacuum permeability, respectively. In first order perturbation theory ΔE is identical to the change in electron affinity induced

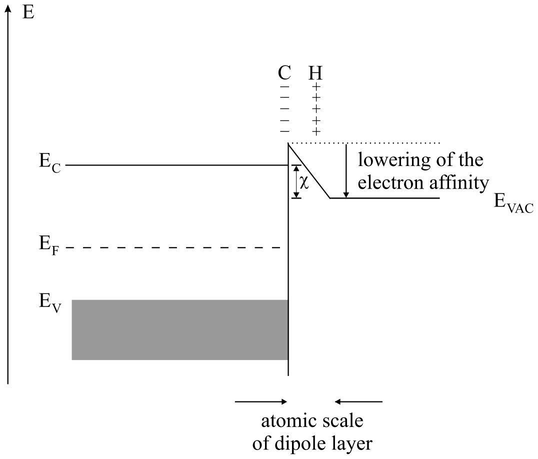

Figure 1.8: Surface band diagram illustrating the electron affinity modification by the polarization of C−H surface bonds.

by the dipole layer. Therefore, the changes in the electron affinity are determined by the electrostatic properties of the responsible surface dipoles. In Fig. 1.8 one can see the change of the electron affinity by surface dipoles for the case of hydrogen terminated surfaces. A systematic and quantitative study of the relation between surface termination and electron affinity of diamond surfaces can be done by combining work function measurements and the determination of the surface Fermi level position relative to the VBM and CBM in the same UHV experiment. Using this technique the continuous transition in electron affinity from a fully hydrogen terminated to a clean surface was measured for the diamond (111) surface [39] and the diamond (100) surface [31]. The same experiment was also performed starting from a fully oxygen terminated (100) surface [31]. Finally, a gradual oxidation of a hydrogen terminated homoepitaxial diamond (100) surface was studied by total photoelectron yield spectroscopy [40]. The work function $\Phi = E_{VAC} - E_F$ was measured with a Kelvin probe and the surface Fermi level position $E_F - E_V$ by photoemission. The electron affinity χ could be readily calculated, knowing the band gap energy $E_G = 5.5\,\mathrm{eV}$ of diamond, from the relation:

$$\chi = \Phi + (E_F - E_V) - E_G \tag{1.2}$$

In the case of hydrogen terminated diamond (100) surface the electron affinity was found to be $-1.3\,\mathrm{eV}$ and was almost identical with that of diamond (111) 1×1:H. For the fully oxygen terminated (100) 1×1:O surface a PEA $\chi = +1.7\,\mathrm{eV}$ was found . Theoretical calculations of the electron affinity of clean as well as hydrogen and oxygen terminated (100) and (111) diamond surfaces have been performed [41]. The theoretical results are in good agreement with experiment, especially for the case of clean surfaces.

1.4.2 Band bending

The presence of defect states in the bulk material and surface states at the edges promotes electron transfer. This leads to the formation of electric fields. These electric fields can either help or prevent the electrons from approaching the surface, in other words the energy bands are lowered or raised towards the surface. This phenomenon is called *band bending.* Surface band bending occurs as a result of hole depletion or due to the formation of a hole accumulation layer. The first mechanism is important for boron doped diamond where surface states or surface defects induce a downward band bending (Fig. 1.9). The second mechanism is reflected in an upward surface band bending and is responsible for the hydrogen related surface conductivity of diamond (see Sec. 1.4.3).

As we have seen, the electron affinity and the surface band bending are two independent phenomena. Exchanging the terminating adsorbates (e.g., hydrogen by oxygen) without inducing or removing surface states or surface defects in the gap results in a change in the electron affinity, while the band bending profile and the surface Fermi level remain unchanged. On the other hand, reducing or increasing the surface density of states in the gap without changing the termination of the surface atoms causes a change in band bending, while the electron affinity is not modified. However, since the change of surface termination and the modification of the surface density of states are usually both consequences of a surface preparation step, one can incorrectly conclude that electron affinity and band bending are related to each other. Surface band bending of diamond has important consequences for the electronic properties of devices.

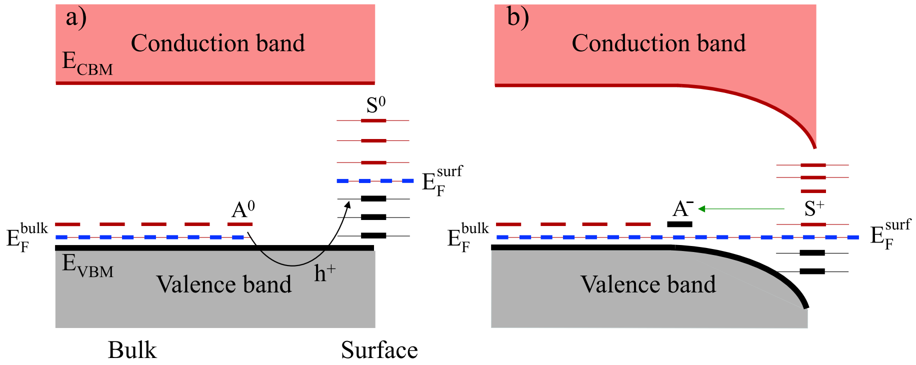

Figure 1.9: The mechanism of band bending for boron doped p-type diamond. (a) The Fermi energies (E_F) of the bulk and surface do not coincide, enabling hole transfer from the neutral acceptor impurities (A^0) to the occupied surface states (S^0). (b) The electric field, which appears during the charge transfer (between the positively charged surface states (S^+) and the negatively charged acceptors (A^-) from the bulk) causes downward band bending towards the surface. The process continues until $E_F^{bulk} = E_F^{surf}$.

1.4.3 The effect of hydrogen on the diamond surfaces

High surface conductivity was first observed on diamond samples in 1989 [42]. Already in that original work the appearance of this conductance was correlated with a hydrogenation of the diamond surface. The SC has been detected on both natural diamond treated by hydrogen plasma [43] and diamond films obtained using the chemical vapor deposition (CVD) technique. The electrical resistance near the surface region of diamond films has been observed to decrease by four orders of magnitude (from $10^8\,\Omega$ to $10^4\,\Omega$) within ten minutes of exposure of the sample to air, after its removal from the CVD chamber [44].

At room temperature the surface conductivity has been measured to be of the order of $10^{-4} - 10^{-5}\,\Omega^{-1}$ [45]. Hall effect measurements show that the areal density of the charge carriers is around $10^{13}\,\mathrm{cm}^{-2}$ [46, 47] and does not change significantly between 60 K and room temperature, but strongly decreases at higher and lower temperatures [48]. Also from Hall effect data, the Hall mobility of these carriers varies slightly with temperature [49] and typical values are in the range $10 - 30\,\mathrm{cm}^2\mathrm{V}^{-1}\mathrm{s}^{-1}$ [47]. A maximum Hall mobility of $70\,\mathrm{cm^2V^{-1}s^{-1}}$ has been reported for a lower carrier density of $1.2 \times 10^{12}\,\mathrm{cm^{-2}}$ [50]. Because the measured mobilities are similar to those found in boron-doped (i.e. p-type) diamond, it has been suggested that the relevant carriers are the holes residing in an accumulation layer at the surface [51]. The p-type surface conductivity was also confirmed by the Hall effect measurements [52–54].

Interestingly, the surface conductivity is only observed on hydrogen-terminated diamond surfaces [45] and disappears after the de-hydrogenation or oxidation of the surface. Therefore, it is believed that the role of hydrogen is critical in the formation of the hole accumulation layer [55]. There have been several models proposed to explain this phenomenon. In the following we will discuss two of these models, which are the most widely accepted: the formation of shallow, hydrogen-related acceptor states [52] or the transfer doping model based on a surface layer of adsorbate material [44, 45, 49, 56].

The shallow-acceptor model

This model assumes that the high conductivity is attributed to holes generated by additional shallow-acceptor levels related with hydrogen incorporated in the surface region [43]. The model was initially supported by the observed ideal rectification properties of Al-Schottky contacts to the CVD diamond, which indicates the existence of the depletion layer at the Al-diamond interface [57].

The depth distribution of the acceptors responsible for the hole accumulation is controversial. It has been proposed that they are close to the surface [49, 51] or that they are distributed in layers extending up to 10 nm into the bulk diamond [57] and even that they could be present in a layer 30 nm below the surface [58]. However, recent studies on Al-based Schottky contacts to hydrogen terminated diamond have reported capacitance measurements that are much too low to be compatible with such a model [47].

The transfer doping model

The transfer doping model, illustrated in Fig. 1.10, assumes the introduction of some foreign species (adsorbates) onto the surface of a material. These adsorbates, acting like dopants, can either add or extract electrons from the substrate. The high p-type surface conductivity on diamond surface exposed to air has also been attributed to this transfer doping mechanism [44, 45, 49, 56].

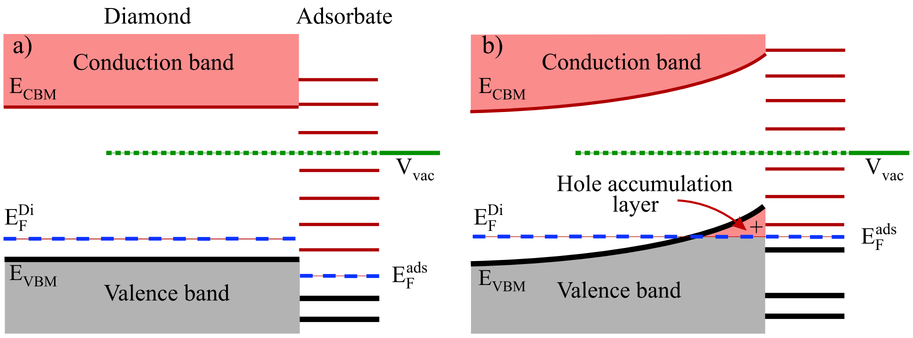

Figure 1.10: Schematic illustration of the transfer-doping mechanism. (a) Before the electronic transfer, the Fermi level (E_F) of the adsorbate is lower than the one of diamond. (b) After the electron transfer, the two Fermi levels are equal and a hole accumulation layer is formed at the surface.

The surface Fermi level after charge equilibration has to be situated at or even slightly below the VBM. As a consequence, the electron affinity of the adsorbates acting as surface acceptors has a lower limit. This is because their lowest unoccupied orbital has to be lower in energy than the Fermi level of the diamond of surface. Considering an electron affinity of hydrogenated diamond $\chi_{Di} = -1.3\,\text{eV}$ and a band gap energy of $E_G = 5.5\,\text{eV}$, from the relation

$$\chi_{ads} = E_G + \chi Di \tag{1.3}$$

the minimum electron affinity of the adsorbates equals 4.2 eV. However, this value can not be reached by any molecular atmospheric adsorbate. Therefore, direct electron transfer from diamond into an atmospheric adsorbate is impossible.

Instead, the thin water layer, which forms naturally on all surfaces exposed to atmosphere, provides an electron system that can act as a surface acceptor for diamond. As long as there are no empty states available in the energy range of the VBM of diamond, the neutral species from the air are not able to act as an electron acceptor. However, if by any ionization process, neutral adsorbates from the air become positively charged, new acceptor states in the required energy range provide an electron transfer from diamond to the ionic species. Although the ionization process does not take place for free adsorbates, for species dissolved in water the presence of ions is a typical situation. Therefore, protons, which are screened by water molecules (H_3O^+), are good candidates to act as acceptors.

Although the situation present in this case, a thin water overlayer (or just isolated water clusters) adsorbed at the diamond surface, is very different from the situation of diamond in contact with an electrolyte of macroscopic dimensions, the latter one can be used as a first approximation in order to describe the fundamental processes involved. It is assumed that the electron exchange from diamond to the water layer is governed by the reduction of protons to molecular hydrogen [59]:

$$2\mathrm{H_3O} + 2\mathrm{e}^- \leftrightarrow \mathrm{H_2} + 2\mathrm{H_2O}, \tag{1.4}$$

where the electrons stem from the diamond valence band. The reaction is driven by the difference in the chemical potential of the liquid phase μ_e and that of diamond, E_F. As long as μ_e is below E_F, electrons are being transferred from diamond to the water layer and thereby reduce H_3O^+ to H_2 and H_2O. This is a self-limiting process since it leaves behind the positive space charge of the holes in the diamond and uncompensated negative ions (for example HCO_3) as space charge in the wetting layer. Due to the electrostatic potential the residual holes in the diamond accumulation layer, and thus the associated surface space charge, lower E_F with respect to μ_e. As shown in Fig. 1.11, at equilibrium μ_e and E_F become equal at the interface.

The stability of hydrogen termination of diamond surfaces is very different in air and in vacuum (where it is stable up to 700 °C) [60], a fact that is attributed to the oxygen content of the air. Using a combination of photoelectron yield spectroscopy, surface sensitive IR spectroscopy and conductivity measurements the influence of surface hydrogenation and adsorbates on the SC has been demonstrated [45]. By annealing the sample at 410 °C in UHV the SC decreased more than six orders of magnitude from $10^{-4}\,\Omega^{-1}$. Then half of the sample was masked in UHV and the surface termination by hydrogen was removed from the unmasked half by electron beam desorption. The conductance and the total photoelectron yield spectrum were measured on both halves of the sample. It has been observed that in UHV SC is virtually removed on both parts of the sample, i.e. also where the hydrogen termination is still intact. After exposing the sample in air the hydrogenated half becomes again conductive (reaching the initial value after 3 days), while for the irradiated half SC remains below $10^{-10}\,\Omega^{-1}$. In conclusion, hydrogen termination is not

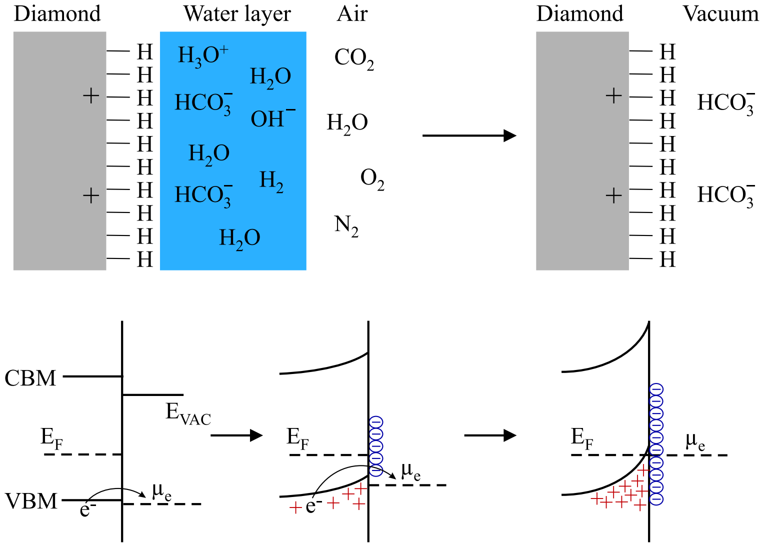

Figure 1.11: Schematic picture of the hydrogenated diamond surface in contact with a wetting layer in air and after it is introduced in vacuum. The lower part illustrates the evolution of the band bending during the electron transfer process [45].

sufficient for establishing the SC, but it is necessary to have also some species from the atmosphere involved.

The essential idea of the doping model described above is the charge exchange balance between hydrogenated diamond and an atmospheric electrochemical redox system. Moreover, very recent experiments [61] indicate that electron exchange systematically occurs between diamond and the aqueous redox couple

$$O_2 + 4H^+ + 4e^- \rightleftharpoons 2H_2O, \tag{1.5}$$

which results in the consumption or formation of oxygen. This charge transfer is responsible for the SC.

1.5 Doping of diamond

Diamond is a semiconductor with a large gap between the conduction and valence bands (5.5 eV). The large energy needed to promote one electron from the valence band into the conduction band makes diamond an electrical insulator under normal conditions, with a resistivity of typically $10^{16}\,\Omega$cm.

By incorporating other atoms having a different electronic configuration into the diamond lattice, new energy levels in the band structure are obtained. These new energy levels can eventually enable conduction. The atoms can be included into the diamond lattice either during growth or afterwards (by ion implantation or diffusion). However, one has to take care that the dopants remain active after the incorporation into the diamond structure.

Diamond is a good candidate for high-power electronics applications that can operate under extreme circumstances, such as high temperature and radioactive irradiation. Moreover, due to its large band gap, diamond is expected to form deep ultraviolet (UV) light emitting devices with wavelength shorter than 250 nm. For these applications, *p*- and *n*-type semiconducting diamonds are needed.

1.5.1 p-type doping

By introducing a *p*-type dopant into the diamond lattice, discrete acceptor energy levels above the valence band of diamond are formed. These energy levels become accessible for electrons from the valence band. When an electron from the valence band occupies one of these levels, delocalized positive holes in the valence band are formed, and this way the conduction appears.

When boron is incorporated into diamond a (shallow) *p*-type semiconductor with a donor level of 368.6 ± 2.5 meV is created [62]. By adding small amounts of B during the growth process boron doped diamond can be obtained. B atoms have been incorporated into both (100) and (111) diamond surfaces.

If boron is added in small quantities in the gas-phase ($<$ 500 ppm) the quality of CVD diamond samples increases. Moreover, faster growth rates and better crystal morphology are obtained. Intermediate B concentrations ($1000-5000$ ppm) produce diamond with characteristics similar to pure carbon CVD growth, but *p*-type. When high boron concentrations are used ($>$ 4000 ppm) crystallinity is lost and the quality of the sample becomes poor [63, 64]. It has been shown that boron may help in the migration of carbon species across a growing diamond surface [65]. Other studies have pointed to the preferential incorporation of boron in the (111) growth sectors [65–67]. The effects of the boron incorporation on the CVD diamond crystallinity is highly dependent on the surface morphology [68, 69].

Boron doped diamond is used for both passive and active electronic devices. In passive electronic devices, highly boron-doped polycrystalline thin films are used as high temperature and high pressure detectors [70]. More recently, pn junctions were obtained by deposition of homoepitaxial films with a boron concentration of $2 \cdot 10^{17}\,\mathrm{cm}^{-3}$ and with a phosphorous content of $8 \cdot 10^{18}\,\mathrm{cm}^{-3}$, with thicknesses of about 1 and $2\,\mu$m, respectively. [71]. Also, highly boron-doped ($> 10^{19}\,\mathrm{cm}^{-3}$) polycrystalline films are used as electrodes for various electrochemical reactions. In 2004, using a very high boron concentration of $2 \cdot 10^{21}\,\mathrm{cm}^{-3}$, superconductive diamond has been obtained at 2.3 K [72].

1.5.2 n-type doping

The *n*-type doping is a result of the inclusion of an atom that creates a donor level into the diamond lattice. A first possibility would be to use nitrogen as a *n*-type dopant for diamond, because N has one more electron than carbon. It has been shown that nitrogen addition into the gas-phase mixtures improves the quality of the diamond samples [73, 74]. However, nitrogen provides a deep donor level (1.9 eV) below the conduction band, which prevents conductivity at room temperature [75].

Sulphur has been suggested theoretically as a prime candidate for a shallow *n*-type donor [76], having growth mechanisms [77] and CVD gas-phase chemistry [78] that are well known.

Phosphorus has been incorporated into the (111) surface of diamond as a substitutional donor [79]. Although the as-grown films exhibit *n*-type properties, they also show poor carrier characteristics. The activation barrier of about 0.6 eV [80–82] is deeper than theoretically predicted. Moreover, theoretical studies predict that phosphorus is insoluble in bulk diamond [83]. However, studies on the (111) surface reconstruction indicate that local near surface solubility is greatly enhanced [84]. The maximum doping concentration is about $5 \cdot 10^{19}\,\mathrm{cm}^{-3}$. Over this concentration, hopping conductivity is observed at room temperature (RT) as dominant carrier transport mechanism. Clear thermal activation of the carriers has been observed for lower P-concentration films. The activation energy was in this case 0.6 eV [85, 86]. A clear diode characteristic has been observed from the pn junction formed with a P-doped n-type diamond thin film grown on a B-doped *p*-type diamond thin film [71, 87]. In

2005, (001) oriented single crystalline P-doped films were grown [88], resulting in a highly efficient UV-emitting pin-junction [89].

Other species have been considered to act as n-type dopants, like Li or Na. Although they looked theoretically promising as interstitial donors [90], no n-type properties were experimentally observed [91, 92]. Also, high-conductivity n-type diamond was achieved by deuteration of particularly selected homoepitaxially grown (100) boron-doped diamond layers [93]. Deuterium diffusion through the entire boron-doped layer leads to the passivation of the boron acceptors and to the conversion from highly p-type to n-type conductivity due to the formation of shallow donors.

1.6 Diamond/metal interfaces

Diamond is the only wide band gap representative of the elemental semiconductors and its surface properties are of fundamental importance.

The interface between semiconductor and metals plays an essential role in technological applications. This interface determines the properties of the contacts. As a result, we can have two types of contacts: rectifying contacts (or Schottky contacts) with finite barrier for charge transfer and ohmic contacts with vanishing barrier for the transfer of charge. By choosing the right metal deposited on hydrogenated diamond surfaces, one can obtain either Schottky or ohmic contacts. In the case of a p-type semiconductor, the energy barrier for charge transfer, also called the “Schottky barrier height” (SBH) is given by the energy difference between the Fermi level and the maximum energy of the valence band (VBM) at the interface.

If the semiconductor and the metal are separated from each other, the common vacuum levels determine the band alignment [94], see Fig. 1.12. On the other hand, when the semiconductor and the metal are joined a space charge region, which extends into the semiconductor over tens to hundreds of nanometers, is formed. This induces a surface charge layer at the metal surface. As a result the two Fermi levels align (Fig. 1.12).

Within the Schottky limit [95] the SBH is the same as derived in the case of the vacuum interface and is given by the work function ϕ of the metal and

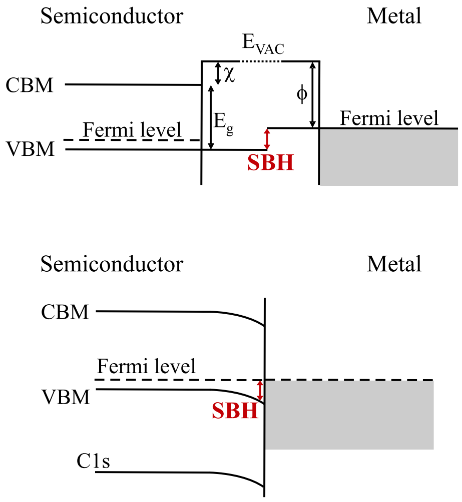

Figure 1.12: The formation of the Schottky barrier for p-type semiconductor (see text for details).

the electron affinity χ of the semiconductor:

$$\begin{aligned} SBH &= E_F - E_{VBM(interface)} \quad (1.6) \\ &= E_g + \chi - \phi, \quad (1.7) \end{aligned}$$

where E_g is the gap energy of the semiconductor. This approach assumes that both surfaces remain unchanged when brought into contact. Therefore, no modification of the initial surface dipole densities is present. The full contact potential between metal and semiconductor drops over the semiconductor by band bending. The electric field can not penetrate into the metal because of the small screening length in metals [7].

An ohmic contact between the diamond surface and the metal can be obtained by using a metal with a work function ϕ that cancels the first two terms in Eq. 1.7, leading to a zero SBH. For the hydrogenated diamond surface, which has an electronic affinity $\chi = -1.3$ eV the minimum work function is $\phi \approx 4.2$ eV ($E_g = 5.48$ eV). In other words, all metals with work functions larger than 4.2 eV should exhibit ohmic contacts on p-type hydrogen terminated diamond. A number of metals that fulfill this condition has been investigated on hydrogenated diamond [96]. Surprisingly, it has been found that not all these metals obey this rule. The only metals which form ohmic contacts on hydrogen terminated diamond are the noble metals (Pt, Au, Ag, Cu), while the more reactive metals (Ni, Al, Sn) form Schottky barriers on hydrogenated diamond surfaces, although their work functions are larger than 4.2 eV. The explanation for this fact is that noble metal deposition maintains the hydrogen termination at the interface in contrast to the more reactive metals.

Another approach for obtaining ohmic contacts on hydrogenated diamond is to reduce the barrier height by using carbide-forming metals such as Ti, Mo and Ta as metal contacts. Although Ti shows higher resistivity on as-grown (hydrogenated) surfaces, TiC formation after annealing reduces the contact resistivity to almost the same value as in the case of Au contact without heat treatment. The carbide formation on diamond leads to good ohmic contacts, which can be explained using the defect formation model on the diamond side of the interface [97].

A third approach depends on recombination in the depletion region of surface defects induced by intentionally damaging the surface of diamond. Consequently, simple metal-semiconductor field effect transistor (MESFETs) devices with enhancement and depletion operation have been fabricated from the thin surface p-type layer, with the coexistence of Schottky and ohmic contacts on the same surface [98–102].

1.7 Properties and applications of the diamond surface

Although diamond is basically an insulating material, the control of conductivity allows for *electronic applications*. The feasibility of these applications is based not only on the bulk properties but also on the unique surface properties of diamond.

E.g., field effect transistors (FETs) have been fabricated by using p-type semiconductor diamond obtained by boron doping [103]. However, the acceptor level for boron, which is the only dopant available for practical use, is deep (0.37 eV) and therefore the density of activated carriers remains low. As a result, the drain current and the operation frequency of conventional device structures, such as metal-semiconductor field effect transistors (MESFETs) and metal-insulator-semiconductor transistors (MISFETs) using low doped p^-

channel, are restricted. In order to improve the properties of diamond devices, different types of device structure have been proposed: p-i-p type FET [104–106], delta-doped FET [107,108], and hydrogenated surface channel FET [102, 109]. Single hole transistors or FET have also been fabricated on undoped H-terminated diamond surface using an electrolyte solution as a gate [110], combining e-beam lithography and a plasma oxidation treatment [111] or by local anodic oxidation process [112, 113]. The latter process will be discussed in detail in the next chapter.

However, the devices performance was much lower than expected from the physical properties of diamond.

The first reason for that is the too low carrier density. Consequently, it is impossible to realize transistor operation even in p-type diamond because of the deep acceptor level of boron. Second, the control of channel carriers is very poor. This is because of the high density of surface states on the diamond surface when it is clean or oxidized. The third reason is the high Schottky barrier height, more than 1 eV. Because of this fact good ohmic contacts are very difficult to form.

Polycrystalline CVD diamond could be used as an electron emitter in flat-panel displays. The idea is based on the diamond property of ejecting electrons from its surface when it is biased negatively in vacuum. Diamond has negative electron affinity, in other words the barrier which electrons have to overcome to escape from the surface is very small, maybe even negative [114]. In practice, this means that devices based on the electron emission properties of diamond could be low energy consuming, therefore very efficient. Using a positively biased grid, the emitted electrons are accelerated towards a phosphorous screen, which causes light to be emitted. Each emitting diamond crystal, or group of crystals, would form a pixel on a flat-panel display screen.

The doped CVD diamond films can also be used for *electrochemical applications*, especially in harsh or corrosive environments. It has been shown that conducting diamond electrodes, made of boron-doped CVD diamond films have a very large potential window in water [115]. This is an advantage when compared to other electrode materials, such as Pt, which dissociate water at higher electrode potentials, resulting in the unwanted evolution of hydrogen and oxygen. The hydrogen evolution rate is much slower when diamond-based electrodes are used, implying much higher electrode potentials can be used.

As a consequence the chemistry of redox couples can be studied, which would otherwise be inaccessible [116]. Finally CVD diamond is a very promising material for biosensor fabrication due to its chemical inertness and the ability to make it electrical semiconducting that enables the connection with integrated circuits [117, 118].

In this thesis we have investigated the electronic properties of the hydrogenated diamond surface by modifying its conductivity. We have developed a method for creating submicrometer scale patterns used for fabricating the electronic devices. We combine the photolithography technique using a double layer positive photoresist, and the local anodic oxidation using a conductive cantilever of AFM on undoped H-terminated diamond surface.

Chapter 2

Experimental techniques

2.1 Introduction

In this chapter we introduce the most important experimental techniques used to fabricate and to study the H-terminated CVD diamond film. For the sample growth, the microwave plasma enhanced chemical vapor deposition (MW PE CVD) technique plays an important role and it is briefly described in the next section. Then, an overview of the thin metal film deposition and the lithography techniques used to pattern and to locally modify the sample are given. Finally, the measuring techniques are described.

2.2 Sample preparation techniques

In order to create submicrometer patterning used for electronic applications on hydrogenated diamond surface, the sample surface needs to be very flat and perfectly hydrogenated. In order to achieve this a combination of techniques is needed for sample growth, surface characterization, metal deposition and lithographic patterning (photolithography and local anodic oxidation).

2.2.1 Microwave (MW) Plasma Enhanced (PE) Chemical Vapor Deposition (CVD)

Chemical vapor deposition (CVD) is a generic name for a group of processes that involve depositing a solid material from a gaseous phase.

In 1953 it was proved that diamond showed homoepitaxial growth from carbon-bearing gas under low pressure [119]. Fifteen years later, Derjaguin [120] successfully synthesized diamond by the CVD method. The research in this direction continued and in 1982 the hot filament CVD method was discovered [121, 122], followed by development of a microwave CVD method. This method drew attention, as it was reproducible and able to produce crystals of good quality [123].

Nowadays, the most used techniques are high pressure, high temperature (HPHT) and chemical vapor deposition CVD. HPHT method is based on the imitation of the natural circumstances under which natural diamond is formed. The CVD method uses a small and simple device and it can be used for coating in any form with polycrystalline diamond. The most common CVD techniques are hot filament (HF)CVD and microwave (MW)CVD. Due to their advantages like high growth rate, high quality, and large area deposition, the (MW)CVD has become the most preferable deposition technique for electronic applications.

In Fig. 2.1 the complex chemical and physical processes, which occur during diamond chemical vapor deposition, are illustrated. First, the process gases mix in the chamber. Subsequently they diffuse towards the substrate surface. On their way they pass through an activation region which provides energy to the gaseous species. As a result, molecules fragment into reactive radicals and atoms, ions and electrons are created, and the gas is heated up to temperatures of a few thousand K. After the activation region these reactive fragments continue to mix and undergo a complex set of chemical reactions until they strike the substrate surface. Here, the species can either adsorb and react with the surface, desorb again back into the gas phase, or diffuse in the vicinity of the surface until an appropriate reaction site is found. If all required conditions are fulfilled, the result of a surface reaction is the formation of diamond. There have been several studies of the gas phase chemistry and it has been shown [124] that independent of deposition system or gas mixture, diamond grows when the gas composition was close to and just above the CO tie-line (see Fig. 2.2). This implies that the diamond growth is independent of the

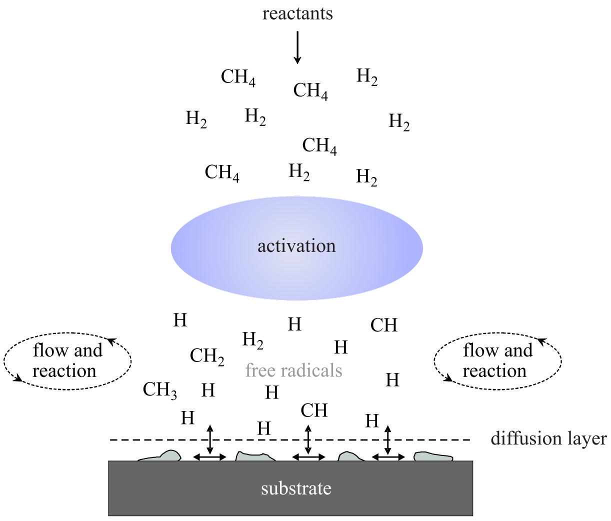

Figure 2.1: Schematic of the physical and chemical processes occurring in the CVD diamond growth

nature of the gas phase precursors. The gas phase chemistry is so rapid that it simply brakes down the constituent gases to smaller and reactive components.

The essential component in the gas phase mixture is atomic hydrogen, which drives the whole chemical system. In a plasma system H is created by electron impact dissociation of H_2. The hydrogen plays an important role in several processes. First, H keeps the sp^3 diamond lattice stable. Although the bulk of diamond is fully sp^3 bonded, at the surface there are dangling bonds, which needs to be terminated in some way in order to prevent cross-linkage and subsequent reconstruction of the surface to graphite. This surface termination is performed by hydrogen (or sometimes OH groups). Second, it is known that atomic H etches graphitic sp^2 carbon many times faster than diamond-like sp^3 carbon. This way, the H atoms serve during the growth to remove back to the gas phase any graphitic clusters that may have formed on the surface, leaving the diamond clusters behind. Third, H atoms break long-chained hydrocarbons up into smaller pieces. As a result, the build-up of polymers or large ring structures in the gas phase, which would inhibit diamond growth, is prevented. Finally, H reacts with neutral species such as CH_4 to create reactive radicals

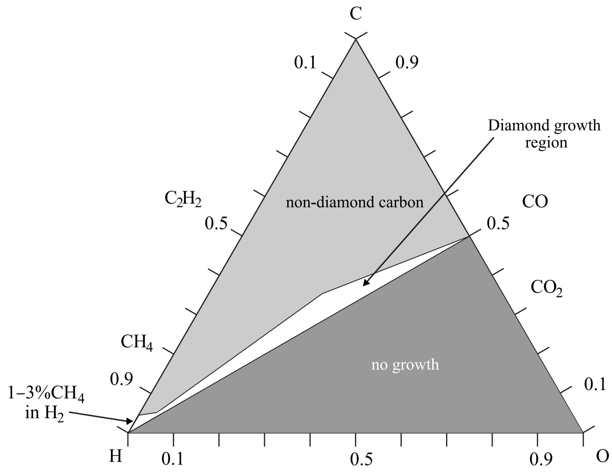

Figure 2.2: Schematic drawing of the Bachmann triangle C−H−O diamond deposition phase diagram [124].

(such as CH_3), which can then attach to suitable surface sites.

Our samples were deposited and hydrogenated by the microwave plasma enhanced chemical vapor deposition (MW PE CVD) technique in an ASTeX PDS-17 reactor at the Institute for Materials Research (IMO) at the Hasselt University, Belgium (Fig. 2.3). The conditions used for the sample growth and the hydrogenation procedure will be described in detail in Sec. 3.2. Apart from CVD samples, we have also used $2 \times 2\,\mathrm{mm}^2$ samples grown by HPHT technique from Element Six.

2.2.2 DC magnetron sputtering

In order to create the electronic devices on the CVD hydrogenated diamond surface we need to prepare first the metal contacts (Ti/Au or Ti/Al). The metal contacts are used as ohmic electrodes. Then, using optical lithography, a micrometer lithographic pattern on the sample surface is created. The device isolation is achieved by eliminating the surface conductive layer during exposure of the surface with an Ar^+ ion beam, while a metal (usually Au) works as a stopping mask for the Ar^+ ions.

Although it is a very old technique, the sputtering process enables with the advent of modern vacuum technology the deposition of thin films of very high

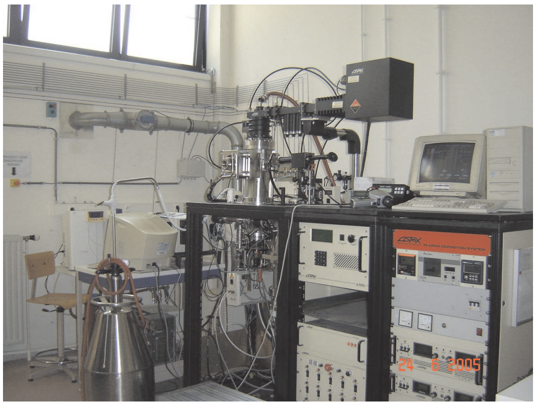

Figure 2.3: Photo of the ASTeX PDS-17 reactor at the Institute for Materials Research (IMO), Hasselt University, Belgium.

quality.

In Fig. 2.4 a schematic drawing of our Microscience DC magnetron sputtering chamber is shown. The sputter chamber has a base pressure of $5 \cdot 10^{-8}$ mbar. During deposition, the chamber is filled with a very low pressure atmosphere of Ar gas (up to a partial pressure of 10^{-3} mbar), which is ionized, forming a glow discharge plasma. Permanent magnets behind the electrode form a toroidal field which confines the plasma in a ring close to the target. Positive Ar ions in the plasma are pulled down towards the electrode by the applied voltage and strike it with a kinetic energy of several hundreds eV. This powerful impact removes material from the target. During this process secondary electrons are also produced, causing further ionization of the Ar gas.

Because the ejection of the atom involves a cascade of collisions, only a small fraction of the energy of the incident particle will reappear as the energy of the sputtered atom. An important parameter is the sputtering yield S, defined as the number of target atoms ejected per incident ion:

$$S = \frac{3\alpha}{4\pi^2} \frac{4m_a m_i}{(m_a + m_i)^2} \frac{E}{U_0}, \tag{2.1}$$

with m_i, m_a the mass of the target atom and of the incoming Ar atom, respectively. α is a monoatomic function of m_i/m_a, U_0 is the surface binding energy of the target and E is the energy of the ion (up to $E = 1\,\text{keV}$).

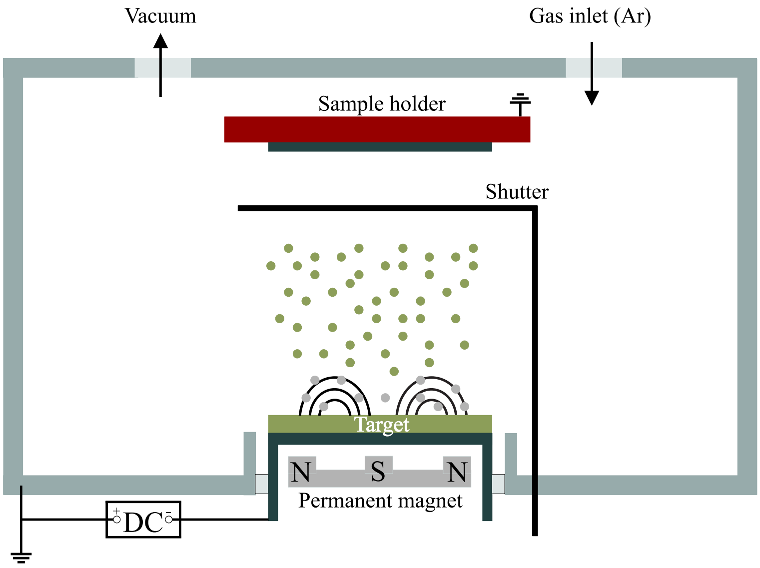

Figure 2.4: Schematic diagram of the DC magnetron sputtering chamber

The current, which is proportional to the sputter rate, is used as the sputter parameter, while the voltage is adjusted automatically and keeps the current at its set-point value. Therefore, the sputter parameters that influence the rate of sputter deposition are the current, the partial Ar pressure and the height of the sample above the target. By choosing carefully all these parameters one can have a finer degree of control over film growth than is possible with evaporation techniques. The deposition of Ti and Au film, which is discussed in this thesis is done with a current of 50 mA and 20 mA, respectively, in an Ar pressure of $2 \cdot 10^{-3}$ mbar. The height of the sample above the target material was set at approximately 3 cm.

2.3 Characterization of the homoepitaxial CVD diamond surface

Scanning Probe Microscopy (SPM) includes a range of microscopy techniques, which involves scanning a sharp tip across the sample surface while monitoring the tip-sample interaction to create a high-resolution image. The most widely used techniques from the SPM family are atomic force microscopy (AFM) and scanning tunneling microscopy (STM). However, many other SPM techniques have been developed, providing information on differences in friction, adhesion, elasticity, hardness, electric fields, magnetic fields, carrier concentration, temperature distribution, spreading resistance, conductivity, etc.

In this thesis, the atomic structure, defects and surface reconstruction of the hydrogenated diamond surface are analyzed with an ultra high vacuum (UHV) STM technique. We also use the AFM in order to characterize the diamond surface (morphology, roughness) and to visualize and locally modify the hydrogenated pattern obtained by the photolithography technique. Additionally, for the characterization of the electrical properties (surface potential, conductivity) of the p-type layer we use the electrostatic force microscopy (EFM).

2.3.1 Scanning tunneling microscopy (STM)

Scanning Tunneling Microscopy (STM) is a technique that was invented in the early eighties of the previous century [125, 126]. This technique enables us to image surfaces with atomic resolution [127]. The operational principle of an STM is illustrated in Fig. 2.5. Using a tip, the microscope scans the sample surface. The tip is moved in the x, y and z directions (with an accuracy down to one percent of an angstrom) with the aid of a piezo-electric actuator that shrinks, expands or bends, depending on the electrical potentials applied to its electrodes. By applying a small voltage bias between tip and sample a tunneling current appears. This is due to the fact that at a few atomic spacings distance between the tip and the sample their electronic wavefunctions will start to overlap and the electrons can tunnel through the vacuum barrier. The tunneling current I is exponentially dependent on the distance s between tip and sample and varies linearly with the applied bias V_t. For small tunneling voltages, the tunneling resistance R_t is given by the following equation:

$$R_t = \frac{V_t}{I} = \frac{h}{e^2}\frac{2\pi s l_0}{A}e^{\frac{2s}{l_0}} \tag{2.2}$$

where l_0 is the decay length for the wave function (of the order of 0.1 nm), A the effective tunneling area (typically of the order of several nm^2) and h/e^2 is the quantum resistance. Because the tunneling current depends exponentially on the tip-sample distance s, the increase of this separation by 0.1 nm implies

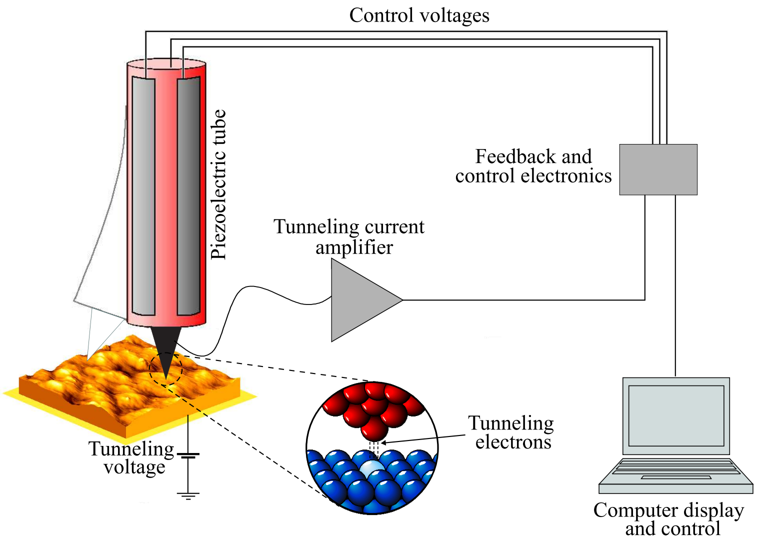

Figure 2.5: Schematic drawing of an STM. When a bias voltage is applied to the sample, a tunneling current will flow. In order to keep the tunneling current constant, a feedback circuit continuously adjust the height of the tip as it is scanned over the surface. This way, a topographic map of the surface is obtained.

a current decrease of one order of magnitude [128]. This makes the STM a very sensitive instrument, with high spatial and vertical resolution.

The STM system operates in two different modes: constant current mode and constant height mode.

In constant current mode a feedback circuit regulates the z position in order to keep the current constant when the tip is moved in x and y directions. This way, by recording the z coordinate as a function of x and y, a topographic map of the surface is obtained. Since the tunneling current measures the overlap between wavefunctions, by STM one does not measure pure topography. Instead, the electronic and topographic information is mixed in the resulting image. The image that comes from the tip topography across the sample gives a constant charge density surface. This means that contrast on the image is due to variations in charge density. In the case of simple metals this is usually not so important, but in other cases (e.g. oxides) one should also take this fact into account when interpreting atomic scale images. The dependence of the tunneling current on the distance between the tip and the sample has a strong influence on the resolution of the STM. Although the overall radius of the tip may be relatively large, the local protrusion that is closest to the surface will completely dominate the tunneling current. Therefore, STM images of flat surfaces have very good spatial resolution. However, when the surface is not flat, the macroscopic size of the tip may become important, because it broadens the high features in an image.

In constant height mode, the probe is scanned at a fixed height above the sample without using a feedback loop. As a result, the voltages controlling the z-movement are kept constant. While the tip is scanning at a fixed height, the tunneling current is recorded and displayed on the computer screen.

Nowadays (UHV)STM is a standard analysis method for the study of surfaces. STM images provide a significant added value to other well-known vacuum analysis techniques. By using ultra-high vacuum one can achieve atomic-resolution imaging of atomically clean surfaces, which would otherwise be contaminated immediately in air. Another advantage of (UHV)STM is the possibility of studying the surfaces without changing (oxidizing) them.

Our measurements were performed with a commercially available STM (Omicron NanoTechnology, see Fig. 2.6) which operates under ultra high vacuum (UHV) conditioins at a base pressure in the 10^{-11} mbar range and at low temperatures (down to 4.5 K).

It is also possible to monitor the tunneling current as a a function of the applied voltage, while keeping the tip at a fixed distance from the sample surface at a particular location. This results in an I(V) curve from which the local density of states (dI/dV) can be obtained. This technique is referred to as *scanning tunneling spectroscopy* (STS) [129]. Additional to measuring the local density of states of a sample at one particular location, STS can also perform spatially resolved mapping. This way, it is possible to image simultaneously the sample topography and to record I(V) curves at every location of the predefined grid [130]. This technique is called *current imaging tunneling spectroscopy* and allows to correlate differences in the surface electronic structure to the sample morphology.

In the case of diamond the STM and STS techniques have been used to

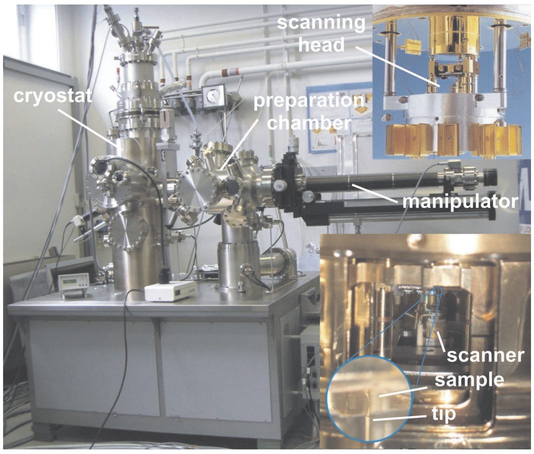

Figure 2.6: Photo of the commercially available STM system (Omicron NanoTechnology) which was used for our measurements.

determine the surface morphology and quality as well as the local surface electronic properties. E.g., atomically resolved STM pictures visualizing the 2 × 1 surface reconstruction of the (001) have been obtained [131–134]. A typical STM image showing the surface reconstruction is shown in Fig. 2.7. Additionally, it was shown using STM that exposure to atomic hydrogen is able to improve the surface reconstruction and etch away the amorphous regions, providing the mechanism for the growth of smooth diamond (100) films [135].

2.3.2 Atomic force microscopy (AFM)

The atomic force microscope (AFM), or scanning force microscope (SFM) was invented in 1986 by Binnig [136]. In Fig. 2.8 a schematic drawing of a typical AFM setup is given. Nowadays, the AFM is an essential tool for measuring surface topography on a scale from angstroms to 100 microns. The main component of the AFM is the cantilever. A tip, positioned at the end of the cantilever, is used to sense a force between the sample and tip. The tip is held several nanometers above the surface and it is able to measure interactions of the order of nN.

The AFM can record the force felt by the tip when brought close to and/or

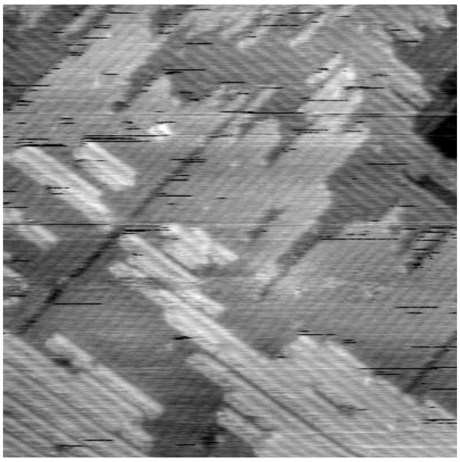

Figure 2.7: UHV STM image of diamond (100) (2 × 1):H surface exposed to atomic hydrogen acquired using a sample bias of 1.5 V [135]

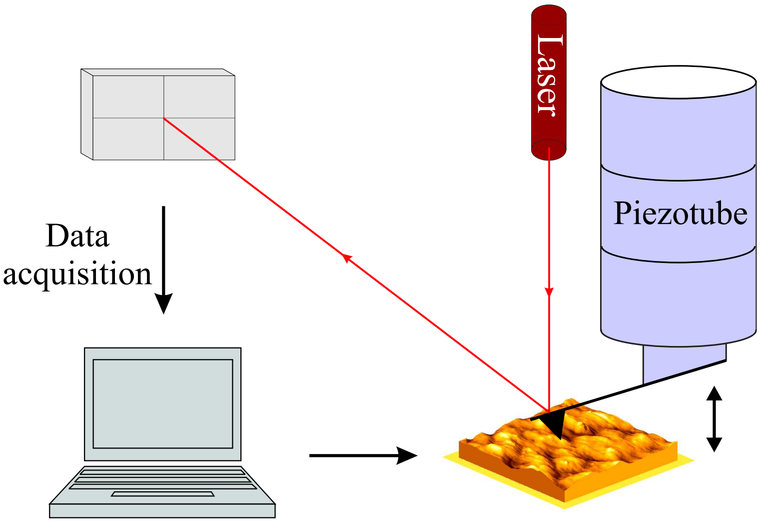

Figure 2.8: Schematic overview of a typical atomic force microscope (AFM).

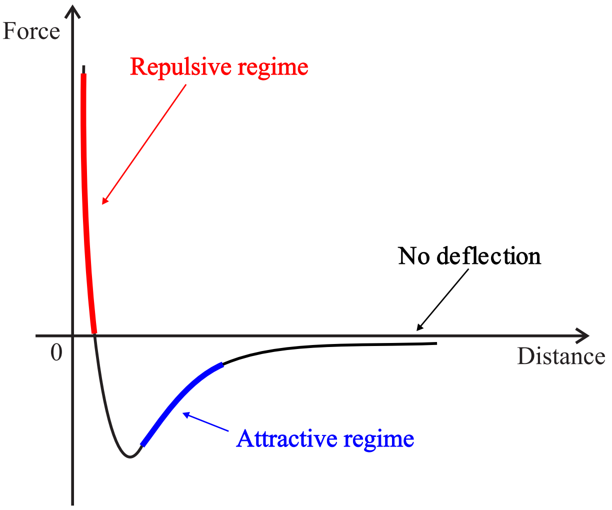

Figure 2.9: Interaction force as a function of distance (tip-to-sample separation).

indented into the sample surface and then pulled away. The force is measured as a function of the deflection of the tip on the cantilever. There are two main contributions to the measured force. The first contribution consists of polarization forces and the second contribution consists of quantum-mechanical forces, which give rise to covalent bonding and to repulsive exchange interactions. Using this technique, both attractive and repulsive forces between the tip and the sample surface can be measured. At small distances between the tip and the sample the force is repulsive, it drops to zero around 0.3 nm and than becomes attractive. The phenomenological Lennard-Jones potential combines the attractive and repulsive potentials:

$$U(r) = 4U_0 \left[\left(\frac{\sigma}{r} \right)^{12} - \left(\frac{\sigma}{r} \right)^{6} \right]. \tag{2.3}$$

In Fig. 2.9 the dependence of the interaction force on the tip to sample distance is shown. When the tip is scanned across the surface, the tip deflection will be the result of a change in topography. Therefore, by measuring this deflection, the topography can be obtained (constant height mode). This method works only for surfaces with limited corrugation. Another possibility is the constant force mode. In this case the force between tip and sample is always kept constant by adjusting the height of the tip. This can be done by changing the z-voltage, which is applied to the piezo and moves the sample up and down. Plotting this voltage during the scan provides the topography of the sample.

There are three distance regimes: the contact regime (C-AFM), where the tip is touching the surface and the force is repulsive (typically, $10^{-6}\,\mathrm{N} < F < 10^{-9}\,\mathrm{N}$), the non-contact regime (NC-AFM) and intermittent-contact (I-AFM).

The C-AFM regime has the disadvantage that the tip can be easily damaged when working with (very) hard samples. Moreover, the samples can be mechanically or chemically modified.

In the NC-AFM regime the cantilever is oscillating in the attractive regime (due to the attractive van der Waals force). The tip is very close to the surface of the sample (a few nanometers), but it does not touch the sample, hence "non-contact". The forces between the tip and sample are quite low, on the order of pN ($10 \times 10^{-12}\,\mathrm{N}$). This regime is based on measuring changes to the resonant frequency or amplitude of the cantilever.

The third method, I-AFM, is a combination of the first two regimes. It is also known as the "tapping mode" or the "intermittent contact mode". The cantilever oscillates closer to the sample than in the NC-AFM mode. Part of the oscillation extends into the repulsive regime, hence the tip intermittently touches (or "taps") the surface. Using I-AFM, the lateral forces, which are present in the C-AFM mode, are eliminated. Therefore in the I-AFM mode the lateral resolution is much improved. This fact can be clearly seen for poorly adsorbed specimens on a substrate surface.

We use the AFM for the CVD diamond surface characterization. Using contact AFM mode was not possible in this case because it involves continuous surface-tip contact, which leads to parasitic adhesive and shear forces between the tip and the diamond film surfaces. Besides, the AFM tip becomes practically unusable after a few scans over the diamond film surface due to an "abrasive" effect. The surface-tip contact is absent in non-contact mode, but spatial resolution is restricted by the surface-tip separation. These problems were avoided using the "tapping mode", in which surface-tip contact is intermittent. Also, tapping parameters were optimized to avoid the switching effects observed in Ref. [137], by checking the correspondence with the contact AFM images.

The AFM can also be used for characterizing other properties of the sur-

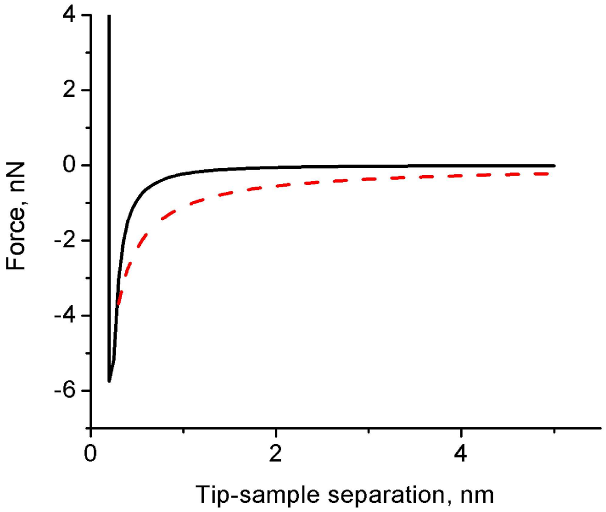

Figure 2.10: Comparison between variation of the force given by Eq. (2.3) (black solid curve) and the electrostatic force (red dashed curve) for a spherical Si tip and a diamond surface. Tip radius and bias voltage are 100 Å and 2 V, respectively.

face such as elasticity and friction and to measure electrical properties (by electrostatic force microscopy) and magnetic properties (by magnetic force microscopy).

In order to distinguish the electrostatic force from the van der Waals attraction, one can rely on the different distance dependence of these forces: the different dependence is illustrated in Fig. 2.10. At larger distance the van der Waals force drops to zero much more rapidly than the electrical force. As one can see from the graph at a distance of 4 nm the electrical force is 200 pN, while the van der Waals force is 40 pN. Moreover, the AFM technique can be used as a local probe to modify the surface. This will be discussed in more detail in Section 2.4.

2.3.3 Electrostatic force microscopy (EFM)

The Electrostatic Force Microscope is a modified AFM, where the conductive cantilever is connected to an independently controlled bias voltage. The bias voltage is used to create an electrostatic field between the tip and the substrate.

The EFM can simultaneously measure the morphology of the surface and the electrostatic force as a function of position. Using a nanoscale proximal probe gives the ability to measure both topographic and electrostatic information with nanometer lateral resolution. Because of its high resolution capability the EFM is a powerful tool for characterizing electronic properties at the nanometer scale.

The contact potential difference

The total electrostatic field near the surface of a sample is the result of many different effects. One of the most significant contributions is from the contact potential difference (CPD). A CPD appears when crystalline objects are placed in the vicinity of each other so that they form a junction. This potential difference results from the equilibrium of both the temperature and the chemical potential throughout the junction [138].

The presence of defects near the surface of a metal or semiconductor lead to the formation of areas with a net charge [7]. This net charge produces an electric potential, V_{vac}, just outside of the solid's surface. As a result, in order to escape the metal, an electron must have a certain amount of energy. The energy required to bring the electron from its highest occupied energy state (the Fermi level) to a position just outside of the metal's surface is equal to the difference between the Fermi energy and the electrostatic potential energy:

$$E_{vac} = -eV_{vac} \tag{2.4}$$

This energy is defined as the work function ϕ of the metal.

When crystalline solids are connected together so that the transfer of electrons is possible, the electrons will reach thermal and diffusive equilibrium. Therefore, the temperature and Fermi level (chemical potential) of the solids become uniform throughout the junction [138]. By a transfer of charge from one solid to the other, the two Fermi levels are aligned. This charge creates an electrostatic field between the surfaces of the junction. The potential difference that now exists across the junction is referred to as the CPD. Since the magnitude of the work function is constant and independent of the position of the Fermi level, the CPD can be described as a difference between the work functions of the two solids.

For instance, let us consider the case of two different metal electrodes with

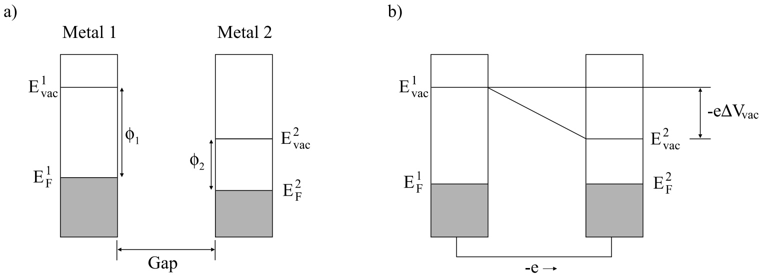

Figure 2.11: Energy band diagram of two metal electrodes (a) before and (b) after an electrical connection is made between them.

different work functions, ϕ, and Fermi levels, E_F. The initial energy levels of the electrodes prior to the formation of the junction are (Fig. 2.11(a)):

$$\phi_1 = E^1_{vac} - E^1_F, \tag{2.5}$$

and

$$\phi_2 = E^2_{vac} - E^2_F. \tag{2.6}$$

A contact potential difference (CPD) appears when the two metals are connected together in a way that allows the electrons in the metals to reach thermal equilibrium [139] (Fig. 2.11(b)). In order to bring the electrons into equilibrium, some charge will flow from one metal into the other. As a result, each electrode has a net surface charge. This charge causes the Fermi levels in each metal electrode to shift until they coincide: $E^1_F = E^2_F$. The net transferred charge resides on the surface of the electrodes and creates an electrostatic potential difference ΔV_{CPD} between them.

When an electron is removed from the Fermi level of one electrode (with work function ϕ^1) and placed into the other one (with work function ϕ^2) at the same Fermi level, the required work W is:

$$W = \phi^1 - \phi^2. \tag{2.7}$$

In order to conserve the system energy, the work done by moving the electron across the potential difference, $-e\Delta V_{CPD}$ and the difference between the work functions must be equal:

$$-e\Delta V_{CPD} = \phi^1 - \phi^2. \tag{2.8}$$

Therefore, by measuring the CPD one can determine the difference in the work functions of the metal electrodes.

In addition to the electric field produced by thermodynamic equilibrium, regions of trapped charge could also exist on the surface of the electrodes. The trapped charge will create its own electrostatic fields. In this case, the overall net field between the electrodes will be a superposition of the electric fields produced by the different charge densities. However, the trapped charge can be treated as a modification of the work functions of the electrodes, allowing the CPD to be expressed as a difference in work functions.

A device used to measure the CPD is referred to as a Kelvin probe [140]. The Kelvin probe technique is based on measuring the potential difference between a sample with an unknown work function and a reference electrode that has a known work function. This technique has proven to be a very valuable tool for probing the work functions of metals and semiconductors [141–144].

Similar to the macroscopic Kelvin probe method, one of the variants of EFM, which is known as a Kelvin probe microscope (KPM), balances the potential difference that exists between a sample and a conducting AFM tip using an applied bias voltage.

Operational Principles

There are two different types of measurements that an AFM can perform in EFM mode. The first one maps electrostatic forces on the surface of the sample, and the second (which is known as Kelvin probe microscopy) images the surface potential of the sample using Kelvin probe method. The first method measures the changes in the internal electric field of a sample by monitoring the force on the scanning tip. The surface potential method measures the surface voltage on the sample by adjusting the voltage on the tip. The voltage applied to the cantilever is adjusted in such a way that a constant oscillation amplitude or deflection is maintained.

In order to understand how an EFM works, let us consider a conducting cantilever tip with radius $\approx 20\,\mathrm{nm}$ at a distance of about $10 - 100\,\mathrm{nm}$ from the sample. The tip is vibrating with a frequency ω_r near its resonance frequency ω_0 (Fig. 2.12). By connecting the cantilever to a controlled bias voltage, one can modify the tip-sample potential difference. A force detector located behind the cantilever detects the electrostatic force created by the modification of the

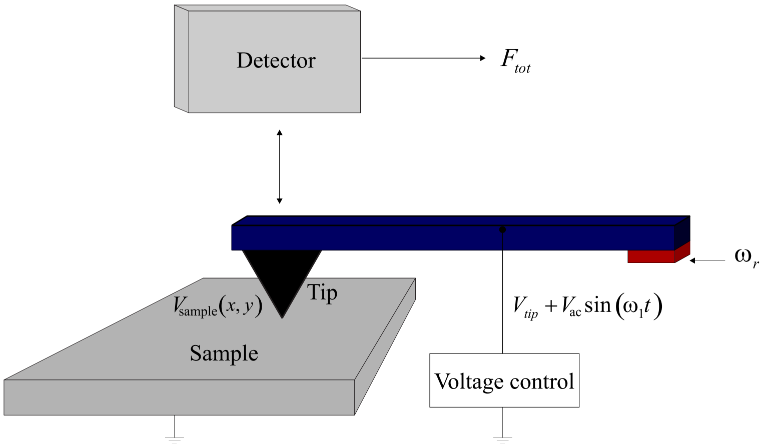

Figure 2.12: Schematic drawing of an EFM

tip-sample potential difference, as well as additional surface forces. The total force acting on the tip-cantilever system has at least three contributions: the mechanical force due to the piezovibrator, the van der Waals force and the electrostatic force [145]:

$$F_{tot}(z_0, t) = k(z - z_0) \sin \omega_r t - F_{VdW} - \frac{1}{2} \frac{dC}{dz} \Delta V^2, \tag{2.9}$$

where z_0 is the equilibrium separation distance between the sample and substrate and the third term represents the component of the electrostatic force that the EFM measures. There may also be a Coulomb force due to the interaction of the tip's trapped charge with its image (F_{image}). Hence, the total force acting on the tip can be written as [145]:

$$F_{tot}(z_0, t) = k(z - z_0) \sin \omega_r t - F_{VdW} - F_{image} - \frac{1}{2} \frac{dC}{dz} \Delta V^2. \tag{2.10}$$

There are well established techniques which measure the $\frac{dC}{dz}$ term in Eq. 2.10 [146–148]. We know that the electrostatic force probe monitors the component of the force due to the capacitance gradient of the tip-sample system. In order to eliminate the electrostatic force acting on the tip, a bias voltage is placed on the tip to modify the ΔV that exist between the tip and the sample. This bias voltage is a combination of a DC offset voltage (V_{tip}) and AC modulation voltage driven at ω_1. The contact potential difference between the tip and the sample becomes:

$$\Delta V = V_{sample}(x, y) - (V_{tip} + V_{ac} \sin \omega_1 t), \tag{2.11}$$

where $V_{sample}(x, y)$ is the potential of the surface and V_{ac} is the amplitude of the dither voltage. Note that V_{sample} is composed from the term corresponding to the tip-sample work-function difference $(\phi_{sample} - \phi_{tip})/e$ and the voltage $V(x, y)$ within the sample which can be induced on the sample surface, for example, by current flow from an external source, (see below). As a result, the force due to capacitance gradient of the tip-sample system can be written as:

$$\begin{aligned} -\frac{1}{2}\frac{dC}{dz}\Delta V^2 = -\frac{1}{2}\frac{dC}{dz}\Big[&(V_{sample}(x, y) - V_{tip})^2 \\ &+2\,(V_{sample}(x, y) - V_{tip})\,V_{ac} \sin \omega_1 t + \frac{{V_{ac}}^2}{2}(1 - \cos 2\omega_1 t)\Big]. \end{aligned} \tag{2.12}$$

The easiest and simplest way of performing electrostatic surface measurements is to keep the voltage applied to the tip, V_{tip}, constant. By scanning the surface with this constant voltage we can obtain the electrostatic force and topography as a function of position. The maps obtained in this way display the relative changes in the electrostatic force due to the varying surface potential of the sample. The electrostatic force measured in this type of EFM imaging is a combination of interactions of the tip and cantilever with the substrate. The nanometer-size variations in the EFM image are due to the local interaction of the surface with the tip. This is because the dimensions of the cantilever are several orders of magnitude larger than the actual tip and therefore, the electrostatic force acting on the cantilever results from the interactions with a large area of the substrate, masking any nanometer-sized variations in the surface potential. The relative polarity of the surface potential is determined by monitoring the phase of the ω_1 component. In this way one can obtain information on the polarity of charge densities on the surface of the sample [148–151]. One has to be aware of the fact that this method of recording the electrostatic potential variation cannot provide an accurate measure of the surface potential.

In order to achieve a more reliable map of the potential of the surface, a controlled modification of the electrostatic force acting on the tip is required (similar to the Kelvin probe). This is done by a feedback circuit which measures the magnitude of the electrostatic force and actively modifies the tip bias voltage V_{tip} in such a way that the amplitude of the ω_1 component is zero. One can then record V_{tip} as a function of position and in this way the map of the actual $V_{sample}(x, y)$ can be obtained. However, in this method the lateral resolution is reduced. This is because of the large area interaction of the cantilever with the substrate. The electrostatic force acting on the cantilever can dominate the forces experienced by the tip. When the feedback system eliminates the ω_1 component, the applied voltage will mostly be the measured potential of a large area of the sample's surface.

It is possible, using these methods, to perform simultaneous measurements of both the surface topography and the electrostatic force. This way one can correlate the surface potential with topography [152].

One can also perform EFM using the two pass technique. The first scan is performed to obtain the topography by scanning the tip near the surface, in the region where the van der Waals forces are dominant, as it is done in non contact AFM. Before the second scan, the system lifts the tip and increases the tip-sample distance in order to place the tip in the region where electrostatic forces are dominant. The tip is then biased and scanned without feedback, along the topography line obtained from the first scan. During the second scan tip-sample distance is maintained constant. The topography line is the line of constant van der Waals force, i.e., the van der Waals forces applied to the tip during the second scan are constant. Therefore, the only source of the signal change is the change in the electrostatic force. As a result, a topography free EFM signal can be obtained from the second scan.

Another method to produce a higher resolution measurement of the surface potential is the EFM-phase mode [153]. Analytical calculations and experimental results have shown that EFM-phase mode can achieve improved resolution by measuring the force gradient induced phase shift, which is a function of the local surface potential. The phase shift is related to the surface potential indirectly, therefore quantification of the EFM-phase measurement is needed. During an EFM measurement, the main scan records the surface topographical data in an intermittent contact (tapping) mode [154]. Then the tip is lifted, kept at a fixed height above the surface, and biased with respect to the sample. At distance z from the sample, the tip experiences an electrostatic force:

$$F(z) = \frac{1}{2}\frac{dC}{dz}(\Delta V)^2, \tag{2.13}$$

where C is the capacitance between the probe and the sample, and ΔV is the potential difference between the tip and the sample.

During the interleave scan, the tip is mechanically driven in oscillation and the tip's resonant frequency and the phase shift due to the electrostatic force gradient dF/dz are measured. For small force gradients, the resonant frequency and phase shift are respectively [155]:

$$\begin{aligned}\Delta\omega &= -\frac{\omega_0}{2k}\frac{dF}{dz}, & (2.14)\\ \Delta\phi &= -\arcsin\left(\frac{Q}{k}\frac{dF}{dz}\right), & (2.15)\end{aligned}$$

where k is the spring constant and Q is the quality factor of the cantilever. In parallel with the conventional topography image the EFM electronics also record the phase shift. From Eq.(2.13) we can infer that

$$\frac{dF(z)}{dz} = \frac{1}{2}\frac{d^2C}{dz^2}(\Delta V)^2, \tag{2.16}$$

and therefore the phase shift can be written as:

$$\Delta\phi = -\arcsin\left(\frac{Q}{k}\frac{d^2C}{dz^2}(\Delta V)^2\right) \tag{2.17}$$

In other words, the phase or frequency shift is a function of the potential difference ΔV between the tip and the sample, and the resolution of the EFM-phase method is determined by the lateral distribution of d^2C/dz^2. This phase shift will always be negative, because d^2C/dz^2 is positive. The electrostatic force between the tip and surface is attractive because dC/dz is negative. In order to calibrate quantitatively the EFM-phase measurement one has to relate the phase shift directly to the local surface potential. Moreover, the calibration has to be performed on a flat sample with known surface potential.

It has been shown that the EFM can be used for the accurate detection of the electrostatic forces and therefore is a sensitive tool for imaging surface dielectric properties and for potentiometry [156]. A very convenient method to measure the tip sample capacitance is to apply an ac voltage at a frequency ω_1 to the tip and using an interferometer to detect the induced oscillations. The tip sample distance z is fixed by a feedback loop and can be adjusted by changing the set point which determines the oscillation amplitude at the resonant frequency ω_0. This way, the stability of the experiment is increased as well. By choosing the frequency of the bias voltage ω_1 to be at a cantilever resonance, the induced oscillation amplitude is increased and this way very small capacitance changes can be detected. The sensitivity is comparable to that of a scanning capacitance microscope [157] with enhanced resolution. In the case of both ac and dc detection the signal depends only on the part of capacitance that varies with the tip sample distance. However, the ac method has the advantage that it can simultaneously provide measurements of capacitance and topography. This method can also be used to map the spatial variation of voltage on a sample. A similar potentiometry has been performed with the tunneling microscope [158], but it is then limited to samples with conductive path exposed in order to allow the tunneling current to flow.

Lateral EFM measurements

The standard EFM can be adapted to perform lateral electrical measurements rather than the sample work function distribution $\phi_{sample}(x, y)$. A device usually containing two electrodes is used [159,160]. One contact is grounded while the other one is biased with V_{dc}, as shown in Figure 2.13. Hence, a voltage distribution $V(x, y)$ is produced due to current flow on the sample surface, in addition to the sample work function distribution $\phi_{sample}(x, y)$ (in standard EFM). An ac voltage V_{ac} is applied to a conductive tip. The tip is then scanned across the sample surface, while the variations of the local electrostatic interactions between the current-carrying sample and tip are recorded. The changing of first harmonic component (the term proportional to $\sin(\omega_1 t)$ in Eq. (2.12)) of the electrostatic force is proportional to both V_{ac} and $V_{sample}(x, y) - V_{tip}$. Here

$$V_{sample}(x, y) = \frac{\phi_{sample} - \phi_{tip}}{e} - V(x, y) \tag{2.18}$$

is the local dc voltage applied between the tip and the sample. The tip then acts as a local voltmeter. Local changes in this voltage distribution can then be correlated to local conductivity differences. Using this mode of operation of the EFM set-up, it becomes possible to simultaneously map the topography, the voltage distribution $V(x, y)$ over a current-carrying film, as well as the work function distribution of the film, allowing to directly compare morphological structure and local electrical properties

The surface potential difference between an H-terminated surface and a locally oxidized diamond surface produced by an atomic force probe has been investigated using Kelvin probe force microscopy [161,162]. It has been shown that the potential of the H-terminated diamond surface is $0.1\,\mathrm{V}$ higher than

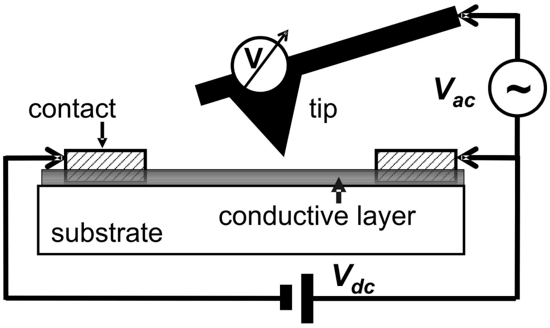

Figure 2.13: Set-up for the lateral EFM measurements on current-carrying conductive film.

that of the oxidized diamond surface. The surface potential difference can be interpreted in terms of the positions of the vacuum level, the Fermi level, and the conduction and valence band edges, when negative electron affinity and p-type surface conduction are assumed for the H-terminated diamond surface.

For our work the results of the locally oxidized (highly resistive) and hydrogenated (conductive) diamond regions were obtained with a modified commercial AFM system (Autoprobe M5, Veeco Instruments, see Fig. 2.14), which operates in contact AFM and in dynamic (non-contact) modes and allows us to perform local anodization under controlled humidity conditions as well as imaging of topography and surface potential [163]. Also, EFM was used to map the voltage distribution of a current-carrying H-terminated diamond surface [164]. Finally, the EFM method was also very useful to probe the contact resistance and to locate interruptions in the conductivity of devices that are fabricated on an H-terminated diamond film surface by lithographic patterning.

2.4 The lithographic patterning techniques

The word *lithography* is derived from Greek and literally means “writing on stone”. This process was used for the first time in 1796 by Aloys Senefelder on the Bavarian limestone (which is still considered the best material for art printing). Nowadays, this word is used in a much broader sense, describing all kinds of processes that involve the reproduction of a pattern onto another surface. For patterning a surface (and eventually create devices) one uses

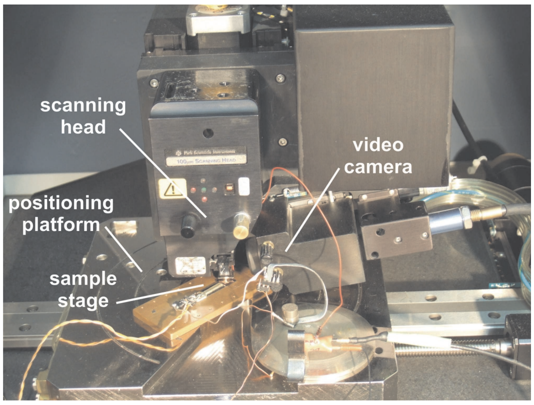

Figure 2.14: Photo of the modified commercial AFM system (Autoprobe M5, Veeco Instruments), which was used for our EFM measurements. The sample is grounded, while a negative bias is applied to the tip.

an exposure tool, mask and resist [165–167]. The process of fabricating very small structures, of order of hundreds of nanometers, is generally referred to as *nanolithography.*

2.4.1 Optical lithography

Optical lithography is the main patterning technique used in the industrial production of semiconductor devices. It is a lithographic process that uses visible or ultraviolet light to create a pattern image on the surface of a wafer coated with a photo sensitive material, called photoresist. For protecting the areas of the photoresist layer that should not get exposed to light, patterned masks are used. These masks are usually made of glass or chromium. The exposure to light and the development of the photoresist in a developer solution afterwards determines which areas of the wafer are exposed for material deposition or removal. There are two types of photoresist materials: negative and positive photoresists.

Negative photoresists are polymers combined with a photosensitive compound. During exposure the photosensitive compound absorbs optical energy and converts it into chemical energy. The chemical energy is used to initiate a polymer linking reaction. This reaction causes cross-linking of the polymer molecules. The cross-linked polymer has a higher molecular weight and becomes insoluble in the developer solution. When introduced in the developer solution only the unexposed areas are removed. However, in the development process the whole resist mass swells by absorbing developer solvent. This is a drawback of using a negative photoresist, since it limits the resolution.

On the other hand, positive resists are resists that become more soluble in the developer when exposed to light, forming positive images of the mask patterns on the wafer. The positive resist consists of three compounds: a photosensitive compound, a base resin, and an organic solvent. Prior to exposure, the photosensitive compound is insoluble in the developer solution. During exposure, the photosensitive compound absorbs radiation in the exposed pattern areas. As a result it changes its chemical structure, and becomes soluble in the developer solution. After development, the exposed areas are removed.

The steps in the transfer of patterns from a masks are the following: the wafer is held on a vacuum spindle, and about 1 cm^3 of liquid resist is applied to the center of the wafer. The wafer is then rapidly accelerated up to a constant rotational speed, which is maintained for about 30 s. The thickness of the resulting resist film, l_R, is given by

$$l_R \sim \frac{(viscosity)(percent\,solid\,content\,in\,resist)}{(spin\,speed)^{1/2}} \tag{2.19}$$

Spin speed is generally between 1000 rpm and 10000 rpm to give a uniform film of about 0.2 μm to 1 μm thick. This procedure can also be applied to multilayer resist systems. After the spinning step, the wafer is given a pre-exposure backing (between 80 °C and 150 °C). This step is done in order to remove the solvent from the photoresist film and to improve resist adhesion to the wafer. Then the wafer is aligned with respect to the mask aligner and the resist is exposed to UV light. The exposed resist is then dissolved in the developer. Finally, the resist is stripped using solvent or plasma oxidation, leaving behind an insulator image (or pattern) that is the same as the opaque image on the mask. For the negative photoresist the procedures described are also applicable, except that the unexposed areas are removed. The final insulator image is the reverse of the opaque image on the mask.

A related pattern transfer process is the lift-off technique presented in Fig 2.15. Also in this case a positive resist is used. The film is deposited over the resist and the substrate. Then, portions of the film on the resist

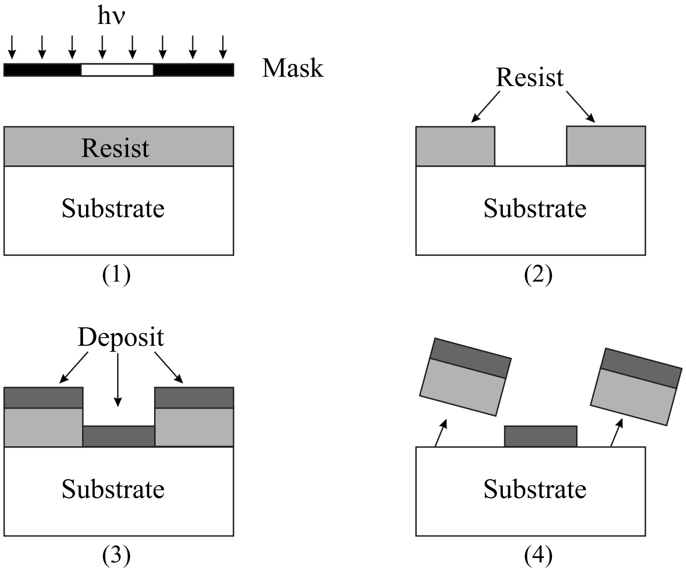

Figure 2.15: The main steps of the lift-off process for pattern transfer.

are removed by selectively dissolving the resist layer in an appropriate etching liquid. This way the overlaying film is lifted off and removed. The lift-off technique is capable of high resolution and is very used for discrete devices, like high-power MESFETs. The minimum feature that can be printed with an optical lithography system is given by the Rayleigh equation:

$$W_{min} = \frac{k_1 \lambda}{NA}, \tag{2.20}$$

where k_1 is a dimensionless scaling parameter, λ is the exposure wavelength and NA is the numerical aperture. In order to pattern devices with smaller feature sizes, photoresist exposure wavelengths have to be reduced and/or numerical apertures needs to be increased. The smallest line patterns, which have been created until now have a width of 29.9 nm and were obtained by IBM in 2006 using deep-ultraviolet ($\lambda = 193\,\mathrm{nm}$) optical lithography [168].

2.4.2 Scanning probe lithography

Scanning probe lithography (SPL) refers to an area of research in which nanometer-scale patterning is achieved using a scanning tunneling microscope (STM) or an atomic force microscope (AFM). One way of patterning the sample is mechanically, by scratching or local heating with a sharp tip. However, a more elegant method uses the tip to oxidize the material in a specific pattern. This can be achieved with an AFM. In this section we will discuss the most relevant scanning probe microscopy (SPM) based lithographic patterning techniques.

Chemomechanical patterning

As we have already mentioned above, one can pattern a sample by exerting mechanical forces on its surface using the AFM tip. However, this method of modifying the surface is not used very much nowadays. This is because the of the poor reproducibility and tip degradation. When scratching the sample the tip is irreversible damaged (blunted). Nevertheless, this approach of patterning the surfaces has been revisited and reapplied [169–172]. The reason for this comes from the fact that, on one hand, state-of-the-art AFM technology allows the modulation of forces with nN accuracy. On the other hand, using soft layers such as self-assembled alkyl thiol monolayers as sacrificial layers allows material removal without tip degradation. Usually mechanical removal is accompanied by the deposition of selected molecules that form covalent bonds with the exposed surface, named chemomechanical patterning.

Dip-pen nanolithography

The dip-pen nanolithography (DPN) process was discovered and developed for nanopatterning purposes by Mirkin et al. [173, 174]. It enables flexible direct deposition of nanoscale materials onto a substrate. By coating an atomic force microscope tip with special types of molecules ("inks"), one is able to deposit well defined lines of the ink in a manner similar to a traditional ink pen.

Field evaporation

Field evaporation is the process whereby atoms are ionized and ejected from a surface due to the action of a high electric field [175]. It is based on the fact that in a sufficiently large electrical field ($\approx 10^{10}\,\mathrm{V/m}$) and a perturbed potential transport of atoms can occur. A perturbed potential is obtained when the tip is brought sufficiently close to a conductive surface. As a result either “mounds” or “pits” are created on the surface.

Parallel processing

The parallel probe approach was successfully applied to surface modification for data storage, using arrays of piezoresistive cantilevers [176–178], or for biological applications using parallel arrays of optical probe devices [179]. Another example is the patterning of a silicon substrate on the centimeter scale by using an array of 50 high-speed probes to perform parallel local oxidation. Nevertheless, strong limitations, including the pattern uniformity and reliability of a large number of probes, represent the main weaknesses for this kind of multi-probe lithography.

2.4.3 Local anodic oxidation of the surface

Using AFM lithography and electrically conductive tips one can create features on the target surface. The process is based on anodic oxidation. Due to atmospheric humidity, an ambient layer of water exists on the surface of the substrate, which provides the oxygen species necessary for oxidation. Because of the small distance between the tip and the sample (around 5 nm) a water meniscus is formed. A bias voltage applied to the tip generates a strong electric field of the order of $10^9\,\mathrm{V/m}$, which causes hydroxide-ion diffusion and drives hydroxide ions from the water meniscus to the surface.

Evidence that the generated electric field plays an important role in this process is given by the dependence of the tip-induced oxidation on tip bias. The fact that water from the ambient is necessary for the oxidation has been interpreted [180] as an indication that the process is analogous to electrochemical anodization.

In Fig. 2.16 the oxidation process using an AFM is schematically drawn. When the tip is in contact with the conductive surface and a voltage V is applied between the tip and the sample, the voltage across the oxide (V_{ox}) is not the same as the applied voltage (V). This is because a small part of the voltage will be across the water layer between the tip and the sample (V_{water}).

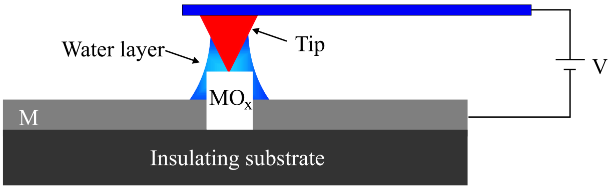

Figure 2.16: Schematic draw of the local anodic oxidation process of a thin electrically conducting film M. When the conducting film is sufficiently thin, the oxide reaches the insulating substrate and two separated conductive regions are obtained.

The applied voltage is a sum of three voltages:

$$V = V_{tip} + V_{water} + V_{ox}, \tag{2.21}$$

where V_{tip} is the voltage across the tip.

This method was applied for the first time on silicon at the beginning of the 90's of the previous century by Dagata et al. [181]. In this work they modified a hydrogen-passivated silicon surface by the application of a bias voltage between an STM tip and the surface. This way surface oxide features were generated.

Subsequently, a slightly different approach, using an AFM with a negatively biased conducting tip (with respect to the sample), was successfully applied to induce oxidation [182–185]. The shape of the oxide pattern depends on a series of parameters, including the writing voltage, the tunneling current, the relative air humidity, tip material and the sample doping concentration and type. The effect of all these parameters can be explained in terms of a field induced process. Understanding the influence of these parameters, one can optimize the process in order to achieve the highest resolution [186]. Applying this method insulating oxide lines as narrow as 10 nm can be produced [184], which enabled the fabrication of nanoelectronic devices [112, 187–196].

On H-terminated diamond surface the results of local anodic oxidation using an AFM, vary between inscribed patterns (creation of pits) and elevated patterns (creation of bumps by oxide formation). Tachiki et al. obtained oxide patterns that stick out of the diamond surface [197]. Rezek et al. obtained patterns with a depth of about 3 nm in the diamond surface by removing thin non-

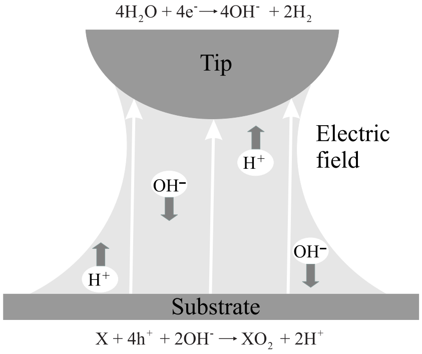

Figure 2.17: The mechanism of anodic oxidation on the diamond surface.

diamond layers from the surface [137]. During the oxidation process of the H-terminated diamond surface the OH^- ions from the water present between the tip and the surface are attracted near the anode, and effectively oxidized with presence of holes (positive charges), as shown in Fig. 2.17. However, the real chemical composition of the surface is yet unknown. The (100) H-terminated diamond surface exhibits 2×1:H structure, while the insulating region changes into a 1×1 structure and the monohydride dimers disappear [112, 198]. The AFM modification technique of the hydrogen-terminated diamond surface has been used for the fabrication of various nanoscale devices. For example, in-plane-gated field effect transistors (FETs) and single-hole transistors (SHTs) have been fabricated. For the in-plane-gated FETs, local oxidation has been used to fabricate the gate separation (insulating) area. For SHTs, the same technique has been used to fabricate both gate separation and narrow tunneling junctions [111–113]. An AFM topographic image of a single-hole transistor is shown in Fig. 2.18. The conducting channel between the source and drain is an H-terminated region (the dark area) and is adjacent to the oxidized insulating region (the bright protruding region). The size of the isolated H-terminated region is $70 \times 80\,\mathrm{nm}^2$.

In our work for modifying the hydrogen-terminated diamond surface we combine photolithography using a double layer positive photoresist and atomic force microscopy based patterning techniques. This recently developed ap-

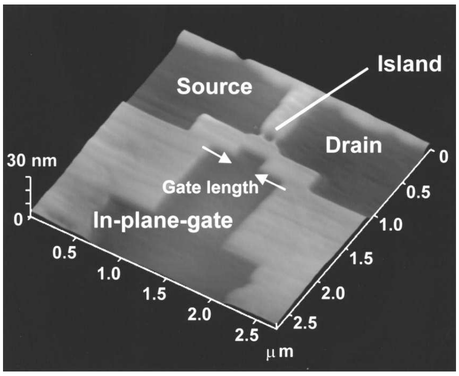

Figure 2.18: AFM image of diamond single-hole transistor [112]. Bright and dark regions represent locally oxidized (O-terminated) and H-terminated regions, respectively.

proach [199], has been successfully applied for obtaining patterns with tens of nanometer linewidth [200, 201]. The details of the patterning conditions will be given in Chapter 4.

2.5 Low-temperature transport properties

Our transport properties measurements have been done in a 4He-flow cryostat using the van der Pauw method [202]. This method, based on the Hall and magnetoresistance effects, is particulary useful for measurements of materials that are not easily fabricated into long, uniform bar shapes, as usually required for reliable transport property measurements. In the van der Pauw method, the thickness of the sample has to be much smaller than the width and length of the sample. In order to reduce the errors, it is preferable that the sample is symmetric. For this kind of measurements one uses a thin-plate sample containing four very small ohmic contacts placed preferably at the corners of the plate. Using this method, properties of the material like sheet resistance, resistivity, sheet carrier density and mobility of the majority carriers can be obtained. Moreover, the doping type of the material can be determined. For determining both the sheet density n_s and the mobility μ, a combination of Hall and resistivity measurements is needed.

The basic physical principle underlying the Hall effect is the Lorentz force.

When the electrons move along a direction perpendicular to an applied magnetic field, they experience a force acting perpendicular to both the magnetic field and the particle's direction of motion. Consequently, the path of the electrons is curved so that moving charges accumulate on one face of the material. This leaves equal and opposite charges exposed on the other face, where there is a lack of mobile charges. The separation of charge results in the Hall voltage, a potential drop across the two sides of the sample. This transverse voltage is the Hall voltage V_H, which is given by

$$V_H = \frac{IB}{qnd}, \tag{2.22}$$

where I is the current, B is the magnetic field, d is the sample thickness, q is the elementary charge and n is the bulk density of the carrier electrons. Sometimes it is more convenient to use the sheet density ($n_s = nd$) instead of the bulk density. To measure the Hall voltage V_H, a current I is fed through the opposing pair of contacts 1 and 3 and the Hall voltage ($V_H = V_{24}$) is measured across the remaining pair of contacts 2 and 4, as shown in Fig. 2.19. Once the Hall voltage V_H is acquired, the sheet carrier density n_s can be calculated from (2.22):

$$n_s = \frac{IB}{q\,|V_H|}. \tag{2.23}$$

Therefore, by measuring the Hall voltage V_H and from the known values of I, B, and q, one can determine the sheet density n_s of charge carriers in semiconductors. The Hall coefficient is defined as:

$$R_H = \frac{V_H d}{IB}, \tag{2.24}$$

and will change its sign, if the sign of the carriers is changed. The sheet resistance R_S of the material can be determined using the van der Pauw resistivity measurement technique. There are two characteristic resistances R_A and R_B, associated with the corresponding terminals, as illustrate in Fig. 2.20. To obtain the two characteristic resistances, one applies a dc current I_{12} between contact 1 and contact 2 and measures the voltage V_{43} from contact 4 to contact 3. In the next step one applies the current I_{23} between contact 2 and contact 3, while measuring the voltage V_{14} from contact 1 to contact 4. R_A

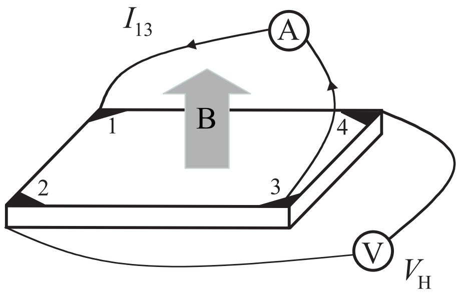

Figure 2.19: Schematic picture of a van der Pauw configuration used for the determination of the Hall voltage V_H.

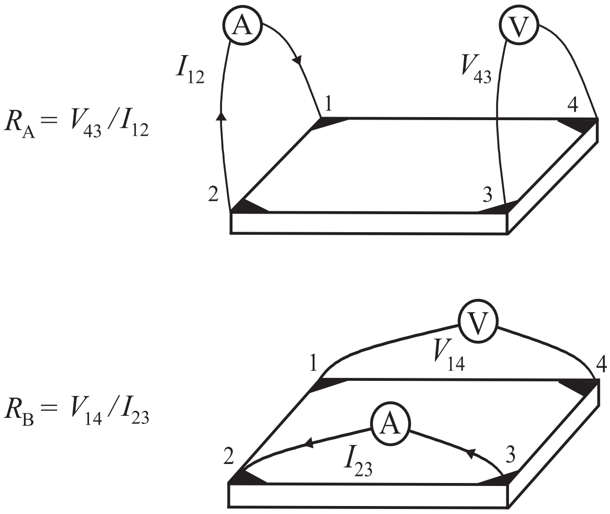

Figure 2.20: Schematic picture of a van der Pauw configuration used in the determination of the two characteristic resistances R_A and R_B.

and R_B are calculated using the following expressions:

$$R_A = \frac{V_{43}}{I_{12}}, \tag{2.25}$$

$$R_B = \frac{V_{14}}{I_{23}}. \tag{2.26}$$

These characteristic resistances are related to the sheet resistance R_S through the van der Pauw equation

$$e^{-\pi \frac{R_A}{R_S}} + e^{-\pi \frac{R_B}{R_S}} = 1. \tag{2.27}$$

This equation can be solved numerically in order to find R_S. The bulk electrical resistivity ρ can be calculated using: $\rho = R_S d$. Since sheet resistance involves both sheet density and mobility, one can determine the Hall mobility from the equation

$$\mu = \frac{|V_H|}{R_S I B} \tag{2.28}$$

$$= \frac{1}{q n_S R_S}. \tag{2.29}$$

When the conducting layer thickness d is known, it is possible to determine the bulk resistivity ($\rho = R_S d$) and the bulk density ($n = n_S/d$).

There are a few practical aspects which must be considered when carrying out Hall and resistivity measurements. First, the ohmic contacts need to be of good quality, the temperature has to be uniform in order to avoid thermomagnetic effects and the environment used has to be dark for minimizing the photoconductive and photovoltaic effects. Second, the sample must be uniform and its lateral dimensions must be very large compared to the size of the contacts and the sample thickness. Finally, the sample temperature, magnetic field intensity, electrical current, and voltage must be accurately measured.

Conductivity and Hall measurements have been performed on CVD hydrogen-terminated diamond. The sign of the Hall coefficient (R_H) in H-terminated sample is positive, indicating p-type conduction of the sample, in other words holes dominate the transport properties. The typical value for the sheet conductivity at room temperature was in the range $10^{-3} - 10^{-5}\,1/\Omega$ [48, 54, 57] and it decreases with decreasing temperature. At lower temperatures the temperature dependence disappears as expected for the conduction of carriers in extended states of a 2D inversion layer [203, 204]. The sheet density varies between $10^{12} - 10^{13}\,\mathrm{cm}^{-2}$ at room temperature and $10^{10} - 10^{11}\,\mathrm{cm}^{-2}$ at low temperatures (around 10 K). It decreases with activation energy ranging from 23 meV for monocrystalline CVD diamond to 0.5 meV for homoepitaxial and natural diamond type IIa, below a critical temperature ($T_c = 70\,\mathrm{K}$). Above this temperature the sheet density is approximately constant [204] or it is independent of the temperature, as expected for 2D transport in extended states in the absence of localization [203].

At room temperature the Hall mobility is in the range $30 - 400\,\mathrm{cm}^2/\mathrm{Vs}$. It has an exponential temperature dependence in the high-temperature regime, with activation energy increasing with decreasing carrier concentration. At low temperature and very high carrier concentration, an almost constant Hall mobility and conductivity is observed [203]. On the contrary, Nebel et al [204] observed a decrease of the mobilities with decreasing temperature below 70 K, following a $T^{3/2}$ law, which indicates scattering at ionized impurities. Below 70 K a strong increase in mobility is detected.

The magnetoresistance of the heteroepitaxial and polycrystalline diamond films was studied using different device structures with a magnetic field ranging from 0 to 5 T. The magnetoresistance changes as a function of magnetic field were more pronounced, and the effects in the heteroepitaxial diamond films were larger than in the case of polycrystalline films [205]. The magnetoresistance of the films at 500 K can still be observed at 5 T, indicating the possibility of a high temperature-operating Hall device application for CVD diamond [206].

The van der Pauw method and a 4He-flow cryostat, which will be described in detail in the next section, were used in order to characterize the electronic transport properties of the submicrometer conductive structure.

2.5.1 Cryogenic set-up for DC magnetic fields

All transport measurements in dc magnetic field have been performed using a 4He-flow cryostat (Oxford Instruments) covering a temperature range from 1.4 K to 320 K and magnetic fields between $-12\,\mathrm{T}$ and $+12\,\mathrm{T}$. The cryostat consists of a vapor shielded dewar, equipped with a variable temperature inset and a superconducting solenoid. A schematic drawing of the setup is presented in Fig. 2.21. The outer vacuum chamber (3) thermally shields the helium reservoir from the surroundings (7). This chamber contains multilayered aluminized

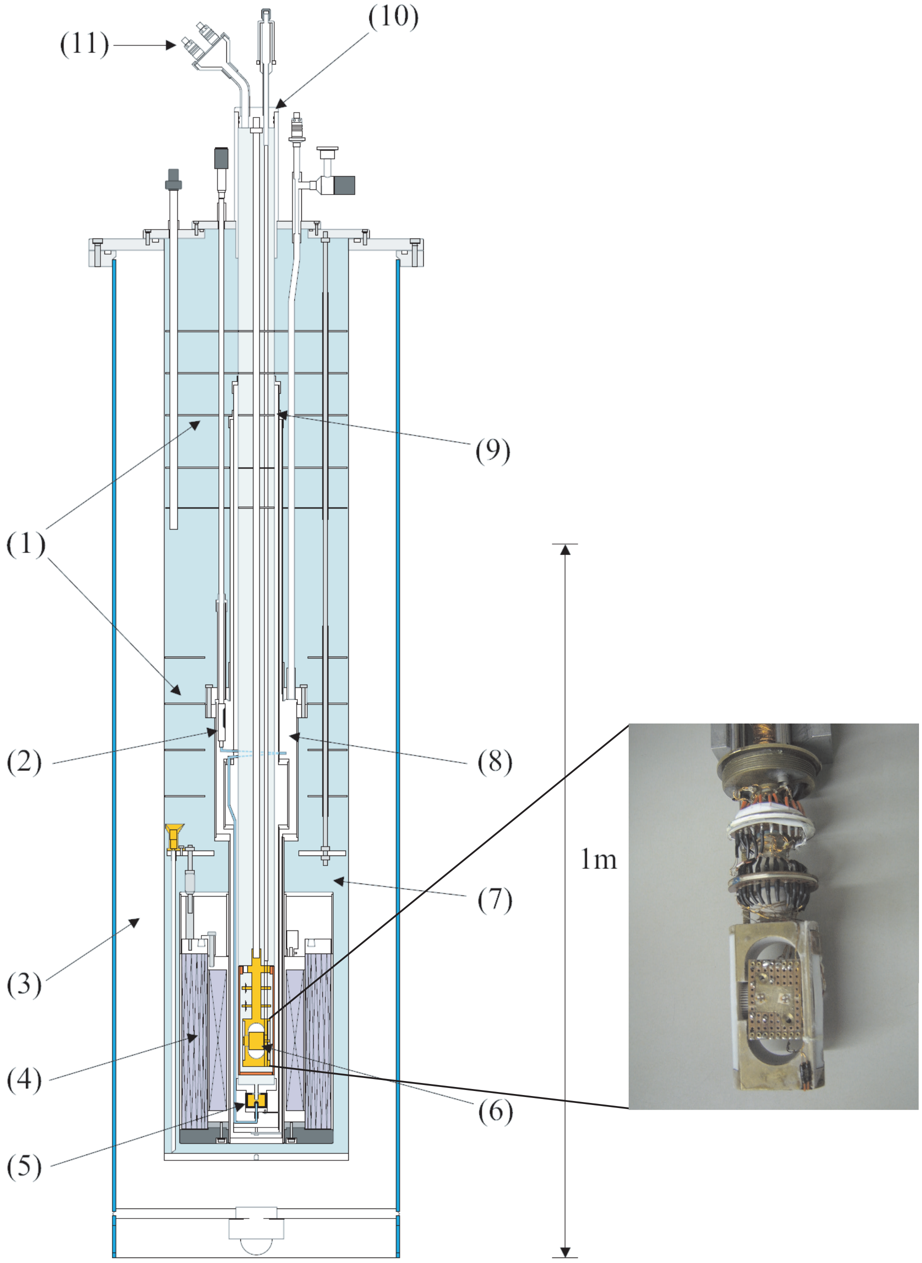

Figure 2.21: Schematic diagram of a cryostat [207] and a zoom photo of the holder with the sample before the insertion into cryostat.

mylar foil to reduce the radiation heat load on the helium reservoir. Inside the reservoir several radiation shields are placed in order to reduce the radiation from the top side of the cryostat. At the bottom of the helium reservoir a superconducting magnet (4) made of Nb_3Sn is located. It consists of different connected coils and produces a vertical magnetic field up to 12 T, which is very homogeneous in the center of the magnet. Relatively large currents (up to 90 A) are produced using an Oxford Instruments PS120 power supply. These currents are needed to generate the magnetic field. The magnet can be brought into the persistent mode at constant field. This is done by short circuiting the magnet with a superconducting wire, so that the field is maintained even when the power supply is switched off. In this mode a stable magnetic field can be kept for many hours and in this way the heat load from the current leads is much reduced. The sample rod (10) contains a sample holder (6) with a temperature sensor and a heater. It is placed in the variable temperature insert or VTI (9), which consists of a long vertical tube inside the cryostat. The tube is isolated from the helium reservoir by the inner vacuum chamber (8). The orientation of the sample relative to the magnetic field can be changed by rotating the sample holder.

Liquid helium can be brought into contact with a heat exchanger (5) at the bottom of the VTI , where it evaporates. This is done through a needle valve (2). Two Oxford Instrument ITC4 temperature controllers control separately the heat exchanger and the sample holder at the bottom of the VTI. By controlling the gas flow and the heater output, any temperature between 1.5 K and 320 K can be reached and stabilized. Even in magnetic fields of 12 T, the error on the temperature sensor is less than 0.1 K for the whole temperature range.

Chapter 3

Growth and characterization of CVD hydrogenated diamond surfaces

3.1 Introduction

Diamond is a wide band gap semiconductor with electronic properties that can vary from insulating (intrinsic) to conductive, using boron (*p*-type) or phosphorous (*n*-type) doping. Additionally, a high surface conductivity has been detected on hydrogen terminated diamond surfaces [42]. The hydrogen termination can be obtained by exposing diamond to a hydrogen plasma at $500 - 850\,^{\circ}$C. The CH dipoles which appear at the surface induce a negative electron affinity [39]. Due to the out-diffusion of electrons into an adsorbate layer of atmospheric species a hole accumulation in the valence band is generated, giving rise to high *p*-type conductivity [45]. In contrast to high conductivity of the hydrogenated diamond surface, the surface terminated by oxygen is strongly resistive. Consequently, by controlling the surface termination, in-plane electronic devices can be realized.

In this chapter we characterize the CVD (100) 2×1:H diamond surface using SPM techniques. First, we present the atomic scale resolution of the hydrogenated diamond surface using an UHV STM technique in order to prove the diamond structure and the good quality of our CVD diamond films. The topography of the surfaces was achieved using an atomic force microscope (AFM). This was done in order to characterize the surface and to optimize the parameters used in the growth process. Finally, the surface conducting properties were measured using the EFM technique.

3.2 Sample growth conditions

CVD diamond films used in this thesis are grown at the Institute for Material Research (IMO) Hasselt or by Element Six company. The CVD films from IMO were grown using the microwave plasma enhanced chemical vapor deposition technique (MWPE-CVD) on (100) Ib orientated HPHT diamond substrates from Sumitomo Electric Ltd., having a misorientation angle less than one degree. Substrates are cleaned and oxidized before the growth using a mixture of sulphuric acid and potassium nitrite at 300 °C for 30 min. The sample is placed in the vacuum chamber that is pumped down to a vacuum of about $6\cdot10^{-9}$ Torr. First, a hydrogen plasma is created at around 700 °C – 850 °C, at a pressure of 60 Torr – 180 Torr, using a power of 500 W – 750 W and a hydrogen flow of 500 sccm. After 5 min the methane is added into the plasma to grow diamond epitaxial layers. This growth is carried out for a few minutes or hours after which the flow of methane is stopped and only the hydrogen plasma is used for another 5 min. After the growth, the diamond surface is oxidized chemically by using the same mixture as described above in order to remove all surface contaminants on the diamond surface. Then, the sample is put back into the deposition chamber and the hydrogenation treatment is carried out in a pure hydrogen plasma. For this hydrogenation treatment, a plasma at a substrate temperature of 700 °C – 750 °C is creating and a pressure between 50 Torr – 75 Torr. A microwave power of 3000 W and a hydrogen flow of 1000 sccm is used and the plasma is kept on for about 30 s after the pressure stabilization (which takes about 2 min) [208]. An overview of the hydrogen terminated diamond samples grown by IMO is given in Table 3.1. Typical growth rate of the CVD diamond film was around 1 μm/h, which allows to estimate the

Table 3.1: Overview of the growth conditions of the CVD films grown at IMO.

Sample	Power (W)	Pressure (Torr)	H_2 (sccm)	CH_4 (sccm)	T (°C)	Time (h)
IMOa	1550	180	500	15	750	5
IMOb	650	180	500	15	750	5
IMOc	750	180	470	47	750	5
IMOd	750	180	470	14	750	5
IMO1	560	180	470	25	700	4
IMO2	500	65	500	0.3	800	5
IMO3	500	62	500	0.4	800	5
IMO4	700	180	495	15	720	6
IMO5	750	180	480	25	730	10

thickness from the growth time. The samples from Element Six are produced by a CVD process from an energized mixture of hydrogen and carbon gases and they are called monodites MCC.

3.3 STM characterization

Scanning Tunneling Microscopy is used for clean characterization of the surface with the highest possible atomic resolution. The technique is used not only for morphologic characterization, but also for local electronic properties of the surface.

Our measurements were performed with a commercially available STM (Omicron). The STM operates under ultra high vacuum (UHV) conditions at a base pressure in the 10^{-11} mbar range and at low temperatures (down to 4.5 K). The UHV is required for stable imaging and for a cleaner environment in comparison to the measurements performed in air, where the surface is contaminated immediately. UHV-STM gives also the ability of studying the surfaces without inducing any oxidation.

Before starting the measurements the $2 \times 2 \times 0.5\,\mathrm{mm}^3$ CVD diamond sample (IMO1 from Table 3.1) was annealed in situ at 450 °C for a few hours. As a result of using a mixture of H_2/O_2 (1% of oxygen) during the hydrogenation procedure, the sample remains conductive even after the annealing process [208]. In order to achieve maximum stability and reproducibility, the

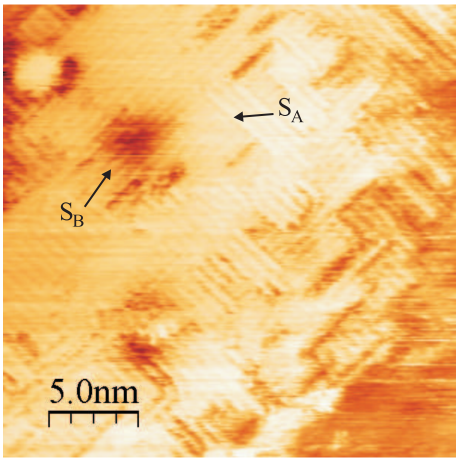

Figure 3.1: STM topography of the hydrogenated diamond C(100) − (2 × 1):H surface (U_{bias} = 1.2 V, I_t = 0.3 nA, T = 300 K).

measurements can be performed at either liquid nitrogen ($T_{\mathrm{sample}} \simeq 78\,\mathrm{K}$) or liquid helium ($T_{\mathrm{sample}} \simeq 4.5\,\mathrm{K}$) temperature. Both mechanically cut and preformed PtIr (10% Ir) tips were used. STM topographic imaging (400 × 400 data points) of CVD hydrogenated diamond surface was performed in constant current mode.

Fig. 3.1 shows $25 \times 25\,\mathrm{nm}^2$ UHV STM image of an homoepitaxial diamond (100) film grown as described above after exposure to atomic hydrogen for 1 min, at a 750 °C. A 2 × 1 surface reconstruction is observed. It is known that the diamond $(100)-(2\times1)$ surface exposed to atomic hydrogen is monohydrate terminated [209], and is denoted as diamond $(100) - (2 \times 1)$:H. The terraces observed in the image consist of atomic planes with dimers rows rotated in the xy plane by 90° relative to the dimer rows in the adjacent planes, indicating a two domain (2 × 1) dimer reconstruction. Two different types of terrace steps are observed, marked S_A and S_B. Single atomic steps that consist of dimer rows parallel to the step edge are S_A steps, and single atomic steps that consist of dimer rows that are perpendicular to the step edge are S_B steps. A bright circular structure having a diameter of approximately 2.5 nm is observed in Fig. 3.2, similar to the one observed in Ref. [135]. It is supposed that the

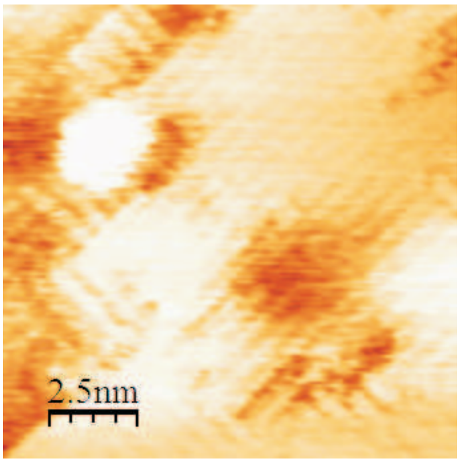

Figure 3.2: $10 \times 10\,\mathrm{nm}^2$ zoom image of the film shown in Fig. 3.1 showing an etch pit with a bright structure inside.

bright structures are etched by products or groups of hydrogen atoms because the structures disappear after the sample is heated to 1000 °C.

A $4 \times 4\,\mathrm{nm}^2$ zoom image (Fig. 3.3(a)) shows that the distance between the bright lines ($\Delta \simeq 5.0\,\text{Å}$) corresponds well to the distance ($5.04\,\text{Å}$) between the C−C dimer rows of the 2×1 reconstructed diamond surface. The bright beam-shape features within the bright lines, separated by $2.5\,\text{Å}$ (see Fig. 3.3(b)), were attributed to single CH−CH dimers [134].

We have also performed I(V) measurements, using a set point of 0.33 nA and a bias voltage of +1 V. The pronounced asymmetric behavior observed in Fig. 3.4 suggests the presence of a Schottky contact between the metallic tip and the semiconducting CVD diamond [210]. The asymmetry is attributed to the surface band bending. At positive voltage a band gap of 0.6 V is visible, which indicates that the Fermi level is pinned near the valence band. However, both asymmetric and symmetric tunneling characteristic have been reported at different locations of the same sample [211–213]. Although this might be explained by inhomogeneities of the hydrogenated diamond surfaces, further investigations are needed to fully clarify this problem.

In conclusion, the STM images, which clearly reveal atomic resolution, demonstrate that our CVD diamond samples have good quality, comparable

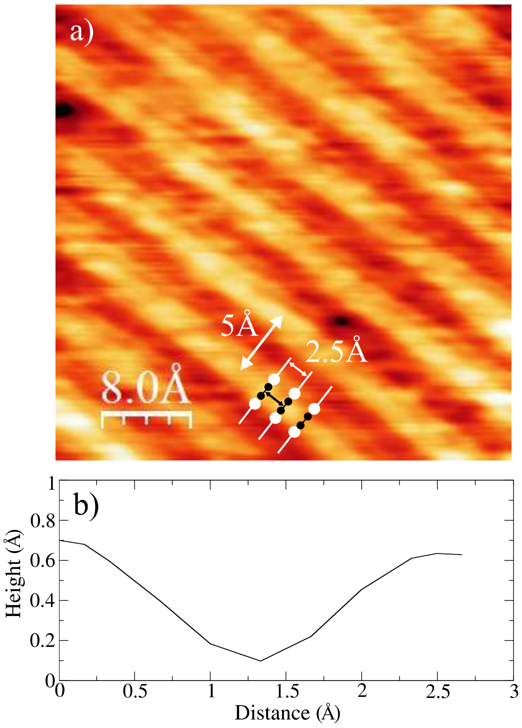

Figure 3.3: (a) UHV STM zoom image of a different area of the film. The bright lines on the topography indicate the C−C dimer rows; (b) Line profile between two CH−CH dimers.

with the one used in Ref. [133]. The absence of defects on most of areas and of the electrically active impurities makes the samples suitable for nanometer-scale device applications.

3.4 AFM characterization

In order to be used for electronic applications the diamond films produced by CVD technique must have flat surfaces. This kind of samples can be obtained only by careful growth process or by polishing techniques.

First we characterize the samples on large scale. This is done because the CVD diamond samples may have defects that are visible even with an optical

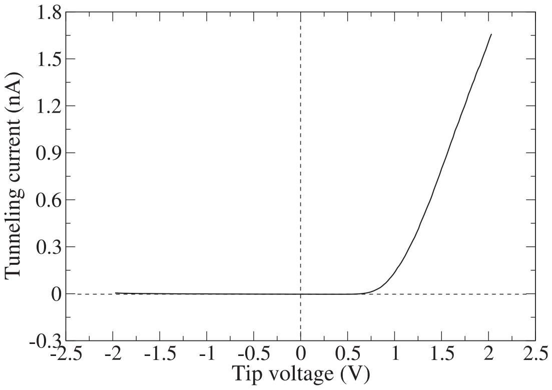

Figure 3.4: I-V characteristic of the hydrogenated diamond sample after UHV anneal at 400 °C for 1 hour ($U_{bias} = 1\,V$, I= 0.33 nA).

microscope. Such defects can be seen in Fig. 3.5. From the optical microscope images we can select the areas which are defect-free and subsequently we can proceed with the small scale surface characterization. For this we use an atomic force microscope device Autoprobe M5 (Veeco Instruments). We performed AFM surface characterization of CVD diamond sample which were grown at different conditions (different microwave power, or different methane concentration). The effects of mechanical polishing and the hydrogen plasma etching processes were also investigated. The surface roughness analysis was done in tapping-mode using a commercial silicon AFM tip (Veeco) with a spring constant of 2.0 N/m, a nominal apex radius of 20 nm and a resonance frequency of 190 − 320 kHz. Typical scan areas were 40×40 μm^2, 10×10 μm^2 and 5×5 μm^2. Surface roughness (Root-Mean-Square (RMS) roughness R_q and Peak-to-Valley (P-V) roughness R_{pv}) values were obtained from a complete image, using the standard roughness definitions (see Table 3.2). In order to analyze the roughness of a thin film, we have identified specific regions that are defects free. For some samples, repeated scans were taken from different regions of the sample. Larger scan areas (up to $80 \times 80\,\mu$m^2) were performed in order to find defect-free regions and to characterize the sample topography.

The effect of microwave power in the growth process of CVD diamond is illustrated in Figs. 3.6−3.7, where the difference in roughness can be observed.

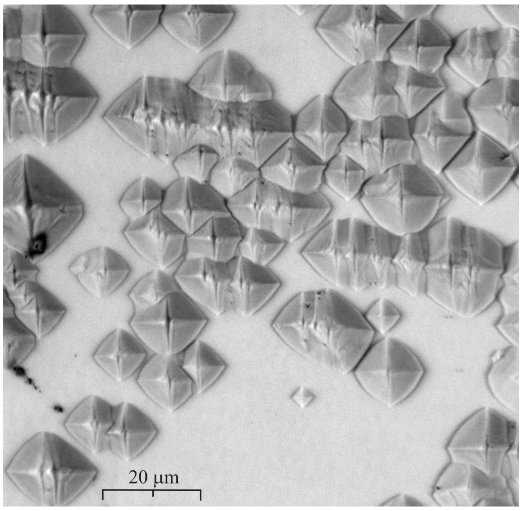

Figure 3.5: An optical microscopy view of the sample surface ($100 \times 100\,\mu\mathrm{m}^2$), revealing pyramidal features.

Table 3.2: Peak-to-valley roughness R_{pv}, root-mean-square roughness (R_q), the average roughness ($\langle R \rangle$) and the scan size of the AFM studied samples.

Sample	R_{pv} (nm)	R_q (nm)	$\langle R \rangle$ (nm)	Scan size ($\mu\mathrm{m}^2$)
Fig. 3.6(a)	293.0	29.3	23.3	40×40
Fig. 3.6(b)	38.1	2.3	1.5	10×10
Fig. 3.7(a)	287.5	6.8	3.9	30×30
Fig. 3.7(b)	30.1	2.5	2.0	10×10
Fig. 3.8(a)	40.6	2.3	1.8	10×10
Fig. 3.8(b)	1339.5	187.0	139.0	10×10
Fig. 3.9(a)	64.0	9.7	7.2	10×10
Fig. 3.9(b)	43.3	1.5	0.8	10×10
Fig. 3.10(a)	3.2	0.4	0.3	10×10
Fig. 3.10(b)	52.7	2.8	2.2	10×10

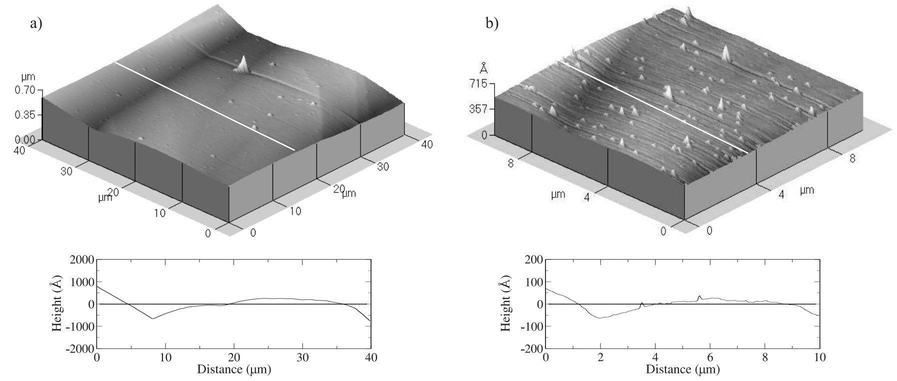

Figure 3.6: $40 \times 40\,\mu\text{m}^2$ (a) and $10 \times 10\,\mu\text{m}^2$ (b) topographic images of the sample grown at 1550 W($IMOa$).

The homoepitaxial films grown at high microwave power are smooth on a small scale ($10\,\mu\text{m} - 5\,\mu\text{m}$), but on the other hand show largest peak-to-valley roughness on $40\,\mu\text{m} - 30\,\mu\text{m}$ scale. The films grown at low microwave power clearly exhibit a granular structure.

We characterized also the effect of the CH_4 concentration used in the growing process. For a very high concentration (10%) the sample are less rough and they show a granular structure. For the samples with low methane concentration (1 – 3%) the AFM images reveal a pronounced topography (crystalline features) visible also with the optical microscope (see Fig. 3.5), which are in fact all “pyramidal deep” with height up to 500 nm on a larger scale ($10\,\mu\text{m}^2$ to $80\,\mu\text{m}^2$), especially near the defects (see Fig. 3.8). The substrate temperature was the same for all the samples (around 750 °C – 800 °C), which is the optimum for the CVD diamond growth. Therefore, we can conclude that the quality of the diamond films deteriorates with increasing methane concentration and decreasing microwave power.

Fig. 3.9 shows an $40 \times 40\,\mu\text{m}^2$ AFM image of a polycrystalline diamond film (sample IMOa from Table 3.1) before and after the mechanical polishing process, which is done using fine diamond powder. The surface morphology of the resulting film is changed dramatically. The roughness is reduced by approximately 80% compared with the original film. The polished samples have not only different roughness, but also a different texture: some crossed

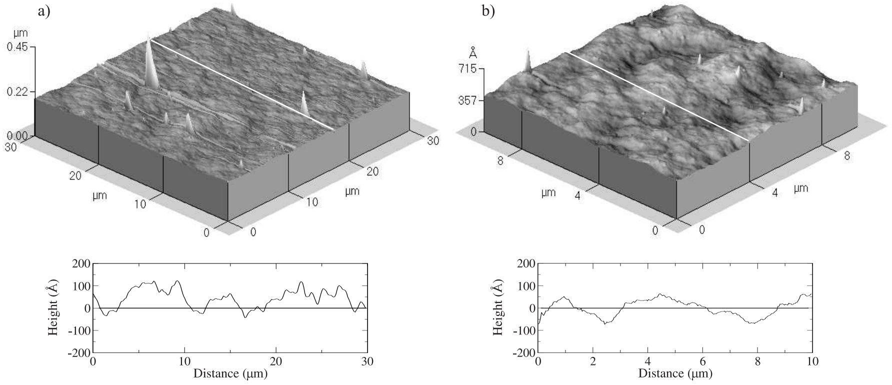

Figure 3.7: $30 \times 30\,\mu\text{m}^2$ (a) and $10 \times 10\,\mu\text{m}^2$ (b) topographic images of the sample grown at 650 W. (IMOb)

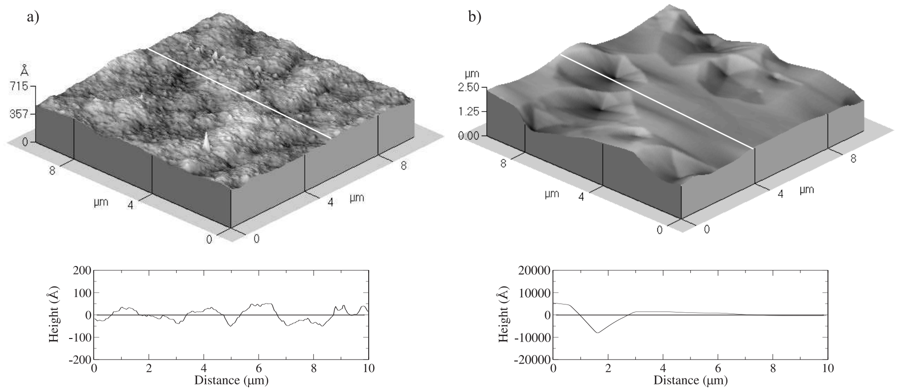

Figure 3.8: $10 \times 10\,\mu\text{m}^2$ topographic images of the sample grown using 10% of CH_4 (IMOc) (a) and 3% of CH_4 (IMOd) (b).

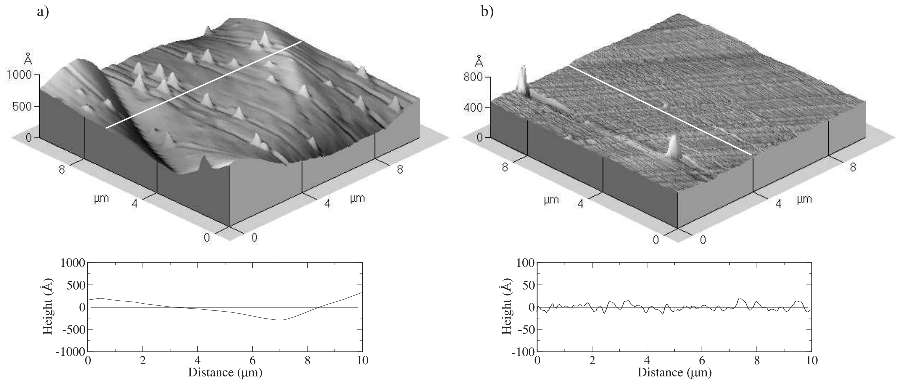

Figure 3.9: $10 \times 10\,\mu\mathrm{m}^2$ topographic images of the sample IMOa before (a) and after (b) mechanical polishing.

scratches features are present.

We have also studied the influence of the duration of hydrogen plasma treatment on the surface roughness. It has been shown that the effect of the plasma etching strongly depends on the initial conditions of the surface [214]. In the case of an (almost) atomically flat diamond sample, a long hydrogenation time leads to an increase of surface roughness. On the other hand, on initially rough samples the etching seems to provide a smoother surface, with smaller roughness [215,216]. For a hydrogenation time of 1 min, the average roughness of the sample is 2.5 Å on $10\,\mu$m scale. After the exposure to the H plasma (Fig. 3.10(b)) for 10 min, the roughness increased up to 22.1 Å on the same scale. Therefore, in our case, the roughness increases with the time of the hydrogenation process.

In order to create lithographic structures suitable for electronic device applications, we combine photolithography and local anodic oxidation techniques. For this we need flat samples (on large scale), which at the same time have to be perfectly hydrogenated. We have seen that samples grown at low plasma power and high methane concentration are suitable for large scale photolithography but not for small scale AFM lithography (Fig. 3.7 and Fig. 3.8(a)), while samples grown at high plasma power and low methane concentrations are suitable for AFM lithography but not for photolithography (Fig. 3.6 and Fig. 3.8(b)). Therefore, the optimal samples are either the ones that are polished or the

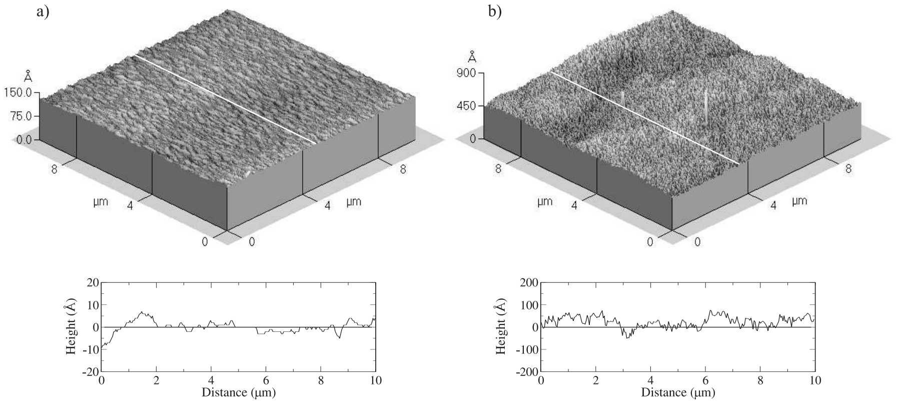

Figure 3.10: $10 \times 10\,\mu\mathrm{m}^2$ topographic images of the sample IMOa hydrogenated for 1 min (a) and 10 min (b).

samples grown using a microwave power of $\sim 750\,\mathrm{W}$ and low methane concentration. Additionally, a short time hydrogenation is needed to avoid the roughness of the surface caused by H plasma etching.

3.5 EFM characterization

With the aim of better understanding the surface conducting properties of the hydrogen-terminated (H-terminated) diamond surface we relied on measurements with electrostatic force microscopy (EFM) [156]. The EFM instrument permits simultaneous measurement of the topography and of the local distribution of the electrostatic potential difference between tip and sample. EFM therefore provides the possibility to detect local variations of the surface potential (SP), which corresponds to the work function for a metallic surface.

EFM maps of the voltage distribution of a current-carrying surface layer clearly reveal conductive and insulating regions, while the SP images (obtained at zero current) are only indirectly related to the distribution of the conductive properties. In contrast to the SP imaging, the EFM mapping of a current-carrying surface layer is rather insensitive to surface contamination or adsorbates. It should be noted, however, that certain adsorbates can influence the conductivity of the surface [217], and consequently affect the distribution of the current. We show that highly conductive H-terminated diamond surface layers behave as diffusive conductors with a well-defined value of the sheet resistance. On the other hand, we find that conductive as well as insulating regions coexist for not perfectly H-terminated diamond surfaces with poor electric conductivity. A similar coexistence of metallic and insulating regions was recently introduced in a model based on long-range potential fluctuations at the H-terminated diamond surface [203].

In order to create a sufficiently large lateral electrical field for the high performance EFM measurements in the presence of a current flow, two narrowly spaced electrodes have to be fabricated on top of the hydrogenated diamond films. This is done by sputtering of Ti/Al bilayers (50 nm) through an optical-lithography mask with a separation between the electrodes of 100 μm. After annealing at 600 °C in Ar atmosphere, the Ti/Al bilayers provide reliable ohmic contact to the hydrogenated diamond surface layer.

After hydrogenation, followed by the contact fabrication, most of the samples (for instance IMO2 from Table 3.1) show relatively high conductivity (sheet resistance R ranges from 20 k$\Omega/\Box$ to 100 k$\Omega/\Box$). Some of the samples were poorly conductive (IMO3 from Table 3.1), their resistance being of the order of 1 M$\Omega/\Box$, although the same hydrogenation procedure was used. The considerable scatter in the conductivity of similarly hydrogenated samples has been reported by several groups, using all kinds of hydrogenation procedures [54, 218]. It is noteworthy that the surface roughness of the poorly conductive samples is typically larger than the roughness of highly conductive samples. A similar effect was observed for polished CVD diamond films, where these films showed higher conductivity values than unpolished, rougher films [219, 220]. Nevertheless, the underlying mechanism remains unknown. We have studied poorly conductive samples as well as samples with a relatively high conductivity by EFM.

The EFM measurements on the contacted H-terminated diamond film samples are performed with a commercial AFM system. The AFM operates in the non-contact mode with the cantilever oscillating near its resonant frequency ($\omega_{res}/2\pi \sim 90$ kHz) at a fixed height (10 nm − 40 nm) above the sample (Fig. 3.11). A dc voltage V_{dc}, modulated at low frequency $\Omega/2\pi$ with amplitude V_m is applied between the electrodes. An ac voltage with amplitude V_{ac} and frequency $\omega/2\pi$ is applied to the conductive AFM tip, a Pt/Ir coated Ultra-

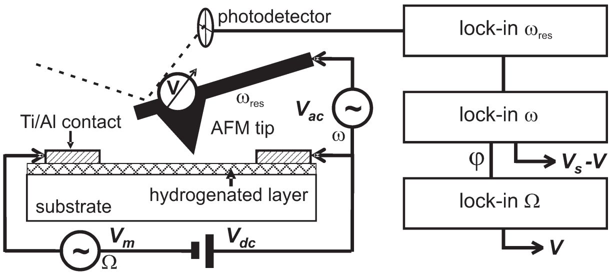

Figure 3.11: Set-up for the EFM measurements on current-carrying H-terminated diamond film surfaces, which includes harmonic detection of the phase shift (ϕ) variations of the AFM cantilever oscillations at the frequency $\Omega/2\pi$ of that is used to modulate the current flowing across the diamond film sample between the two Ti/Al electrodes. The double lock-in setup allows one to separate the current-induced voltage distribution $V(x, y)$ from the surface potential distribution $V_s(x, y)$.

lever (Veeco Instruments) with a spring constant of 3.2 N/m. The AFM tip is then scanned over the H-terminated diamond sample surface, while the local electrostatic interaction between the current-carrying sample and tip, which reflects the surface current distribution, is detected in two different ways.

In a first approach (Fig. 3.11, signal output from the lock-in amplifier at frequency $\omega/2\pi$), which is similar to conventional EFM [221], we rely on harmonic detection of the amplitude of the AFM cantilever oscillations caused by the ac-modulated (at frequency $\omega/2\pi$ ranging between 3 kHz and 9 kHz) local voltage between the AFM tip and the sample surface. The changing harmonic component of the electrostatic force is proportional to V_{ac} as well as to $V - V_s$. Here, V is the local dc voltage between the AFM tip and the sample, while V_s is the SP of the sample. In Fig. 3.11 the AFM tip therefore acts as a local voltmeter. The EFM signal is converted into a potential (in Volts) using the results of a standard EFM calibration procedure with the AFM tip positioned above the electrode (see Fig. 3.11). The applied dc voltage V_{dc} is in the range $0 - 10\,\mathrm{V}$ ($V_m = 0$ in the first approach), while $V_{ac} = 2\,\mathrm{V}$. Using this EFM mode, it becomes possible to map the topography as well as the voltage distribution $(V - V_s)(x, y)$ on the sample surface, which contains the voltage $V(x, y)$ induced by current flow through the H-terminated diamond film and the component $V_s(x, y)$ corresponding to the SP distribution of the film. The SP distribution $V_s(x, y)$ can be mapped separately in the absence of a transport current ($V_{dc} = 0$), allowing us to directly compare morphological structure and local electrical properties on a relatively large scale ranging between 40 μm and 80 μm.

In a second approach, we use a double lock-in detection (Fig. 3.11), signal output from the lock-in at frequency $\Omega/2\pi$) and measure the harmonic component of the variations of the phase shift of the cantilever oscillations caused by the current-induced local voltage between the AFM tip and the sample surface. The current that flows across the diamond film sample between the electrodes is modulated at low frequency $\Omega/2\pi = 177\,\mathrm{Hz}$. This approach allows us to separate the current-induced voltage distribution $V(x, y)$ from the SP distribution $V_s(x, y)$ and decrease the influence of surface topography on the results of our measurements. According to [153, 222] the phase shift is proportional to the electrostatic force gradient that can be written as

$$\begin{aligned} \nabla(F)_\omega \quad \approx \quad & C''(z) \cdot V_{ac} \cdot \big[V_s(x, y) - \\ - \quad & V(x, y) \cdot (1 + m \sin(\Omega t)) \big] \cdot \sin(\omega t) \end{aligned} \tag{3.1}$$

where $C''(z)$ is the second derivative of the capacitance of the tip-sample system, which depends on the tip-sample distance z, and $m = V_m/V_{dc}$ is the modulation coefficient ($0 \leqslant m \leqslant 1$). Relying on Eq. 3.1 we are able to do better measurements of the current-induced voltage distribution $V(x, y)$ because the electrostatic force gradient component varying proportional to $\sin(\Omega t)$ is less susceptible to the SP, parasitic surface charges and height variations on the sample surface. Moreover, an EFM-phase method, which is used in this second approach, provides improved spatial resolution when compared to conventional EFM [153, 222]. We have first used standard EFM (see Fig. 3.11, signal output from the lock-in at frequency $\omega/2\pi$) to visualize the electrical voltage distribution in highly conductive ($R < 100\,\mathrm{k}\Omega/\Box$) current-carrying H-terminated diamond films as well as in current carrying H-terminated diamond films with poor conductivity ($R \approx 2\,\mathrm{M}\Omega/\Box$), as illustrated by the two examples in Fig. 3.12. The gray-scale contrast gradient from the left side to the right side of the EFM image in Fig. 3.12(a) for the highly conductive film clearly demonstrates the electrical potential drop due to the resistive properties of the H-terminated diamond film. The corresponding lateral voltage profile is shown in

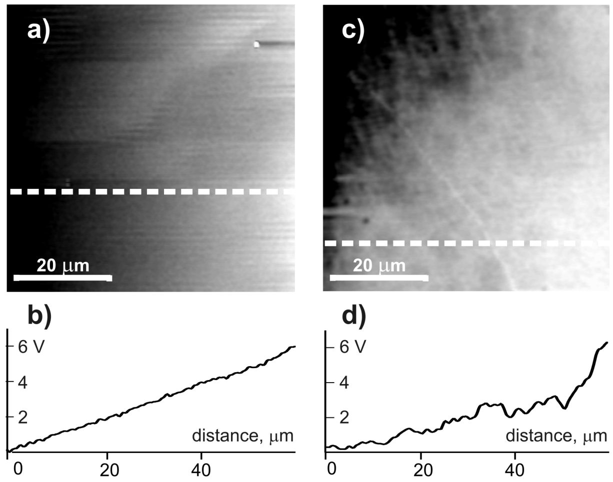

Figure 3.12: $60 \times 60\,\mu\text{m}^2$ EFM images of the current-carrying H-terminated diamond film surface ($V_{dc} = 10\,\text{V}$) for a highly conductive ($R \approx 47\,\text{k}\Omega/\Box$) – IMO2 (a) and a poorly conductive ($R \approx 2\,\text{M}\Omega/\Box$) – IMO3 (c) sample. The linear voltage drop indicates that the highly conductive layer behaves as a spatially homogeneous, diffusive conductor (b). On average, the voltage continues to drop uniformly along the poorly conductive film, but pronounced fluctuations of V are present at micrometer scale (d).

Fig. 3.12(b). The EFM signal $V(x)$ drops uniformly along the film. According to Fig. 3.12(b) the average voltage drop is $0.10 \pm 0.02\,\text{V}$ over $1\,\mu\text{m}$ ($V_{dc} = 10\,\text{V}$). The linear voltage drop in highly conductive H-terminated diamond surface layers indicates that these layers behave as diffusive conductors with a well-defined value of the sheet resistance. Figure 3.12(c) shows an EFM image of a current-carrying H-terminated diamond film sample with poor conductivity ($R \approx 2\,\text{M}\Omega/\Box$). While the average EFM signal continues to drop uniformly along the film (Fig. 3.12(d)), pronounced fluctuations of $V(x)$ are present at micrometer scale, which cannot be attributed to topographical features. In Fig. 3.13 we show AFM topography and EFM images of the current-carrying H-terminated diamond film sample with poor conductivity ($R \approx 2\,\text{M}\Omega/\Box$). In contrast to the highly conductive diamond film samples, the EFM image (Fig. 3.13(b)) of the poorly conductive sample acquired at $V_{dc} = V_m = 0$, and

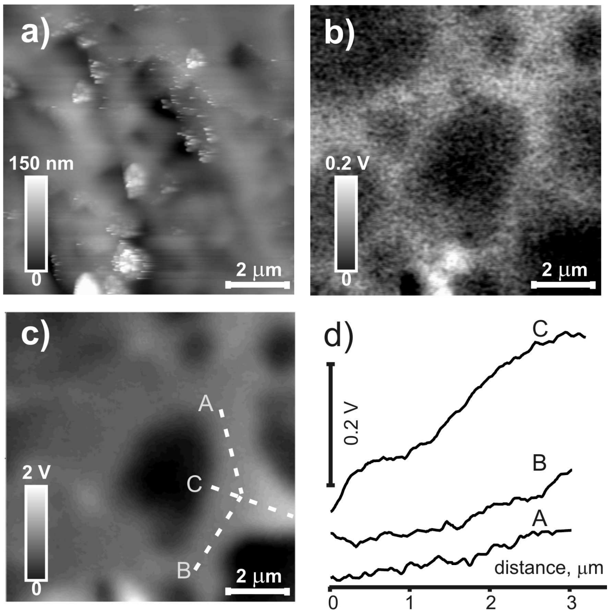

Figure 3.13: 10 × 10 μm^2 topographic AFM image of the poorly conductive sample IMO3 (a). Corresponding EFM images of the film surface without any current flow ($V_{dc} = 0$) (b), and of the current-carrying film surface (c). Electrical potential profiles along the three lines (A, B and C) indicated in (c) are shown in (d).

using harmonic detection of the EFM signal component related to the frequency $\omega/2\pi$, clearly reveals regions with different SP. According to [223] brighter areas are areas with a lower SP. This can be attributed to a higher negative electron affinity. Consequently, the regions with a brighter contrast may be considered as the H-terminated areas. However, we cannot exclude the presence of some surface contamination or trapped electrostatic charges that modify the SP distribution. Such a modification is unlikely in our experiments due to two reasons. First, the observed average SP difference of 150 ± 50 mV between the brighter and the darker regions is in agreement with the SP difference between H-terminated and oxygen terminated (O-terminated) areas reported in Ref. [161]. An additional argument is that the topographic image (Fig. 3.13(a)) does not reveal any features that are correlated with the observed SP distribution (EFM image shown in Fig. 3.13(b)) and may be attributed to surface contamination. Relying on our sample preparation procedure (see above) we expect that contrary to the H-terminated bright regions darker regions correspond to O-terminated areas. Consequently, the observation of the grain-like structure of the SP distribution is consistent with our hypothesis of a partially hydrogenated surface consisting of H- and O-terminated domains.

Figure 3.13(c) shows the EFM image of the current-carrying poorly conductive film ($V_{dc} = V_m = 5\,\mathrm{V}$), which was acquired using the double lock-in setup (see Fig. 3.11). To obtain the EFM image shown in Fig. 3.13(c), we have relied on harmonic detection of the phase shift variations of the cantilever oscillations at frequency $\Omega/2\pi$, i.e. the modulation frequency of the current that flows across the diamond film sample. As discussed above, this allows us to map the current-induced voltage distribution $V(x, y)$ on the sample surface. The cross-sections of the EFM data labeled by the dashed lines A, B and C in Fig. 3.13(c) are shown in Fig. 3.13(d) and clearly reveal a non-uniform distribution $V(x, y)$. The voltage profiles across the regions corresponding to the brighter contrast in the EFM images show a different behavior for lines A, B and C. The profiles for lines A and B have a smaller drop of voltage along the direction of the cross-sections. On the other hand, the voltage profile along the line C reveals on average a pronounced drop from the right to the left. We attribute this difference to the current flow along the cross-sections: The current flow along cross-section C collects the current flow along cross-sections A and B. These observations provide another confirmation of our interpretation that the regions with a brighter contrast in Fig. 3.13(b) are the H-terminated and consequently conductive areas. Our analysis of other cross-sections of the EFM data confirms that the current preferentially flows along the brighter regions. It therefore looks reasonable to assume that the current flow on the H-terminated surface is obstructed by the darker regions that can be related to insulating O-terminated domains.

The spatial resolution for detecting a local drop of the current-induced voltage, which is achieved in our double lock-in EFM method, can be inferred from the results shown in Fig. 3.13(d). If the lateral resolution is taken to be equal to the full width at half-maximum height of the smallest protrusion that can still be observed in the voltage profile plots, a value of $50 - 70\,\mathrm{nm}$ is obtained.

3.6 Summary

We have used the UHV STM technique for studying the atomic structure of steps and defects on the H-terminated CVD diamond (100) 2×1 surface. Subsequently, an AFM has been used for the surface topography, in order to choose the most suitable sample for large and small scale lithography, and for creating submicrometer structures on the surface (see Chapter 4). Using these techniques, we have characterized several samples, grown at different conditions. The surface analysis enabled us to choose the samples suitable for the electronics device applications.

On the other hand, we have shown in this chapter that EFM is a valuable technique to characterize the surface conductivity of current-carrying H-terminated diamond films. Our method of harmonic detection of the EFM signal caused by the ac-modulated current flowing on the sample surface allows us to clearly separate the influence of changes in the surface conductivity from variations of the SP and of the sample topography. For highly conductive H-terminated diamond surface layers, the linear voltage drop indicates that these layers behave as diffusive conductors with a well-defined value of the sheet resistance that is constant for the whole surface. For H-terminated diamond surfaces with poor electric conductivity, we observe the coexistence of conductive as well as insulating regions. Our results support a simple physical picture that is based on current flow obstructed by insulating regions. The conductivity decreases when the fraction of the surface occupied by insulating regions increases.

Chapter 4

Fabrication and characterization of conductive structures on H-terminated diamond surfaces

4.1 Introduction

In this chapter we present the two lithographic processes which we have used in order to create micrometer and sub-micrometer structures on H-terminated diamond surfaces. These structures can be used in electronic device applications. First, the large scale lithography with the creation of the pattern on H-terminated diamond surface. Then the small scale local anodization lithography is presented. Finally, combining these two techniques, we obtain conductive sub-micrometer structures, which are analyzed by EFM and then used for electric transport measurements.

4.2 Fabrication of the micrometer lithographic structure

In order to create patterned structures on the hydrogen-terminated diamond surface, we combine the photolithography technique (described below) and the local anodic oxidation process. These structures, which form Hall crosses, will be characterized by EFM and will be used for transport properties studies. For this we use a $2 \times 2\,\mathrm{mm}^2$ hydrogen terminated diamond sample, as schemati-

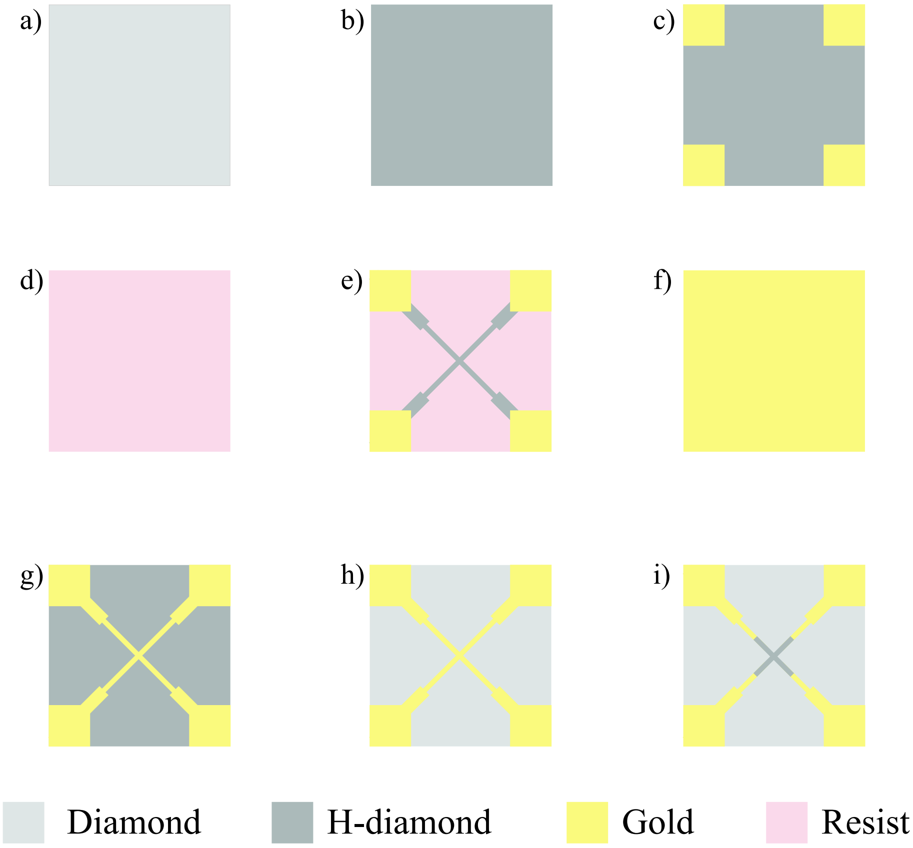

Figure 4.1: Schematic illustration of the process followed for creating the structures on H-terminated diamond surface (see text).

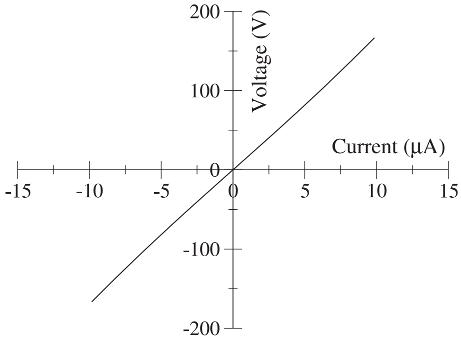

Figure 4.2: I-V characteristic of Ti/Au ohmic contacts after annealing at 450°C for 20 min.

cally depicted in Fig. 4.1(b). First we deposited the Ti/Au contacts, separated by 1 mm from each other, (100 nm/50 nm) using a DC magnetron sputtering (Fig. 4.1(c)). The vacuum chamber used for deposition has a base pressure of $5 \cdot 10^{-8}$ mbar and a large DC voltage (~ 1 kV) is applied between the anode with the substrate and the cathode containing the source material (target). The Ti underlayer improves the adhesion of the Au with the hydrogenated diamond surface. In order to prepare good and stable ohmic contacts, the sample is then annealed at $\sim$ 450°C for 20 min. In this way a titanium carbide (TiC) layer with thickness of several nanometers is formed [97, 224]. This carbide formation correlates well with observation of ohmic I-V behavior (Fig. 4.2). In order to prepare the structures, a double layer positive resist was spin-coated on the hydrogenated diamond surface (Fig. 4.1(d)). The bottom layer was a non-photoresist material (LOL-2000) which dissolves in photoresist developer in a controlled way. The thickness of about 200 nm is obtained at 3000 rpm spin speed. After spinning, the resist layer is baked out on a hot plate for 5 minutes at $140°C$. The next step is to spin the normal photoresist layer (S 1813) at 4000 rpm for 1.3 um thickness and bake it at 110°C for 2 minutes. Afterwards, the resist layers are illuminated through a pattern mask for 25 s using an ultraviolet (UV) Karl Süss illuminator, followed by the immersion of the sample in the developer (MF319) for 30 s and clean with distilled water (Fig. 4.1(e)). The sample is then introduced in the DC magnetron sputtering for the Au deposition (Fig. 4.1(f)). We used the Au as a mask for the hydrogenated layer.

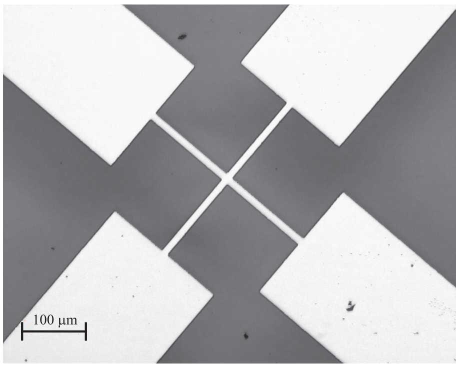

Figure 4.3: Optical microscope image of the Au structure created on the hydrogen terminated diamond surface.

In order to remove the photoresist we used the N-methyl-2-pyrrolidine (NMP) (Remover 1165) (Fig. 4.1(g)). An optical microscope image of the structure at this stage is shown in Fig. 4.3. The removal of the hydrogenated layer from the surface can be achieved by exposing the surface to Ar^+ ions [113]. However, that method has two disadvantages. First, (part of) Au is simultaneously removed. Secondly, the Ar+ bombardment can cause the graphitization of the diamond surface [225], as can be observed in our STM image in Fig. 4.4. However, the elimination of the conductive hydrogenated surface layer can also be achieved by the exposure of the sample to an oxygen plasma. We have employed the latter method and kept the sample in the oxygen plasma for 30 s (Fig. 4.1(h)). In the final step we partially etched the Au structure in the central part of the sample (Fig. 4.1(i)), using a potassium iodide (KI) solution [113]. The resulting feature in the middle part of the sample is a cross formed by hydrogen-terminated lines of 10 μm width and 150 μm long.

4.3 Submicrometer scale lithography on H-terminated surface using AFM

AFM can be used not only to characterize but also to modify electronic as well as structural properties of hydrogenated diamond surfaces on a microscopic level. Electrically insulating patterns are formed on hydrogenated diamond

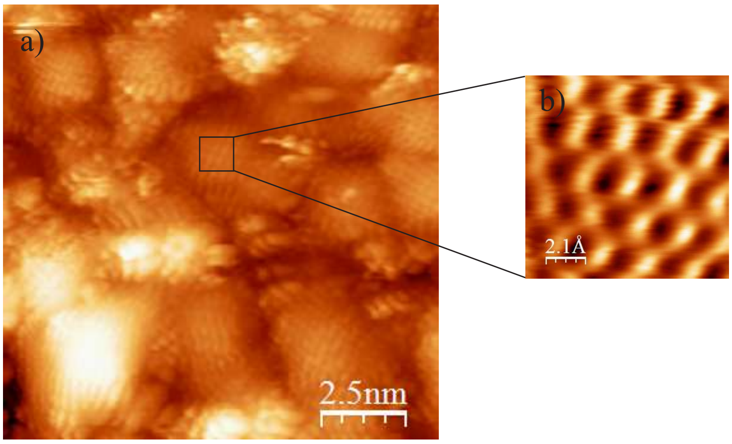

Figure 4.4: $12 \times 12\,\mathrm{nm}^2$ STM image of the diamond sample IMO1 from Table 3.1 (a) and $1 \times 1\,\mathrm{nm}^2$ zoom image (b) showing the graphene flakes present on the diamond surface after Ar^+ treatment.

surfaces by applying negative bias voltages on the AFM cantilever which scans the surface. Formation of the patterns is attributed to anodic oxidation, which is a well-established process on silicon [192], but its mechanism on diamond still needs to be elucidated.

Our AFM instrument is a modified commercial AFM system Autoprobe M5 (Veeco Instruments), which can operate in both contact AFM and dynamic modes and allows us to perform local anodization under controlled humidity conditions as well as imaging of topography and work function or surface potential (SP). The modes of operation of our AFM can be easily switched during the experiment. The setup for AFM local anodization is shown in (Fig. 4.5(a)). An adjustable voltage source, which consists of a battery, a switch of polarity and potentiometer, is connected through a resistor ($1\,\mathrm{M}\Omega$) to the electrodes of a patterned conductive structure microfabricated on a sample surface. This battery-powered circuit is perfectly decoupled from other parts of the AFM measurement circuit in order to avoid any parasitic currents which can disturb the local anodization process. A preamplifier OA is used to measure “in situ” the current flow through the tip-sample surface contact in a wide current range ($1\,\mathrm{pA} - 100\,\mathrm{nA}$) during the anodization process. The output signal of

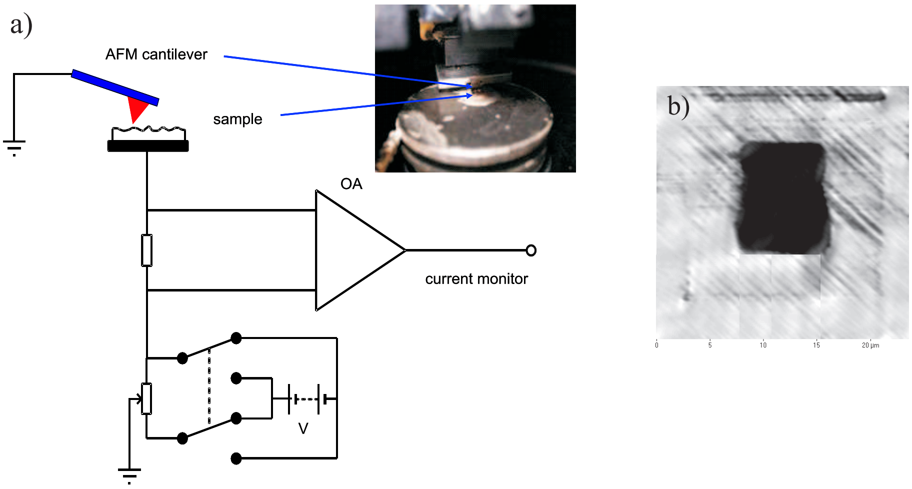

Figure 4.5: (a) Schematic drawing of our modified atomic force microscope. (b) Current image obtained after the local anodization process. The darker region corresponds to the treated area, which has lower conductivity.

the preamplifier is used to acquire the “current” images during the anodization process as well as the conductivity maps of the locally modified sample surface or structure. An example of such a conductivity map is shown in Fig. 4.5(b). This image was acquired at a small bias voltage which is considerably lower than it is required, and demonstrates the result of local anodization over the square area of $9 \times 9\,\mu\mathrm{m}^2$. The treated area has considerably lower conductivity which corresponds to the darker square region in Fig. 4.5(b).

We built a setup to control the relative humidity of air near the sample. The AFM unit was placed in a hermetically sealed box which was ventilated with controllably water-saturated air in order to adjust humidity. The relative humidity was measured by the probe placed near the sample.

The diamond surface is locally oxidized using an AFM operating in contact mode. We apply a negative voltage to the conductive AFM tip in air at controlled humidity ($65\% - 70\%$). The voltage applied to the silicon tip is varied between $-6\,\mathrm{V}$ and $-15\,\mathrm{V}$. Topographic images of the AFM-modified regions were obtained in contact-AFM as well as in tapping AFM modes. Tapping parameters were optimized to avoid the switching effects observed in [137], by

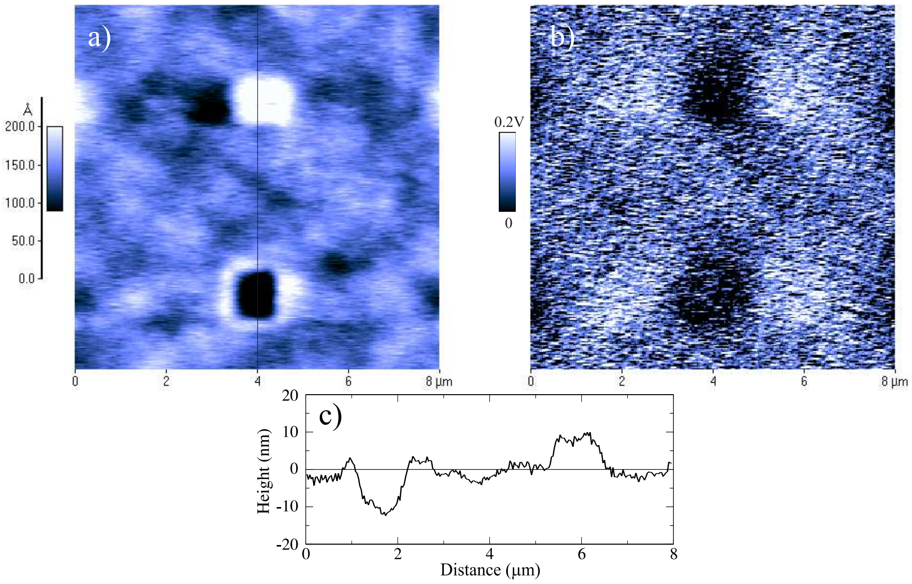

Figure 4.6: (a) Topographic image of a CVD diamond surface after AFM modification, obtained in tapping mode (see text). (b) EFM surface potential image of the hydrogen-terminated and locally modified diamond surface. The vertical scale (black to white) is 200 mV. (c) Line profile for the patterns displayed in (a).

checking the correspondence with the contact AFM images.

Figure 4.6(a) shows the topographic image of a locally modified $1 \times 1\,\mu\text{m}^2$ square area on a hydrogenated homoepitaxial CVD diamond surface (sample IMO4 from Table 3.1). For the upper square we applied a negative voltage of -10 V, while for the bottom square a voltage of -15 V was used. From the line profile in (Fig. 4.6(c)) we infer that the upper square sticks out of the surface, while the bottom square is scribed into the diamond surface.

We investigated in more detail the influence of the applied voltage on the height (depth) of the patterns. The elevated patterns are obtained for negative voltages lower than -10 V, and the inscribed ones are obtained at voltages larger than -12 V. The results are plotted in Fig. 4.7. Each point of the graph is obtained by averaging over about 100 line profiles. The height of the features that stick out of the surface ($3-8$ nm) does not depend on the applied voltage,

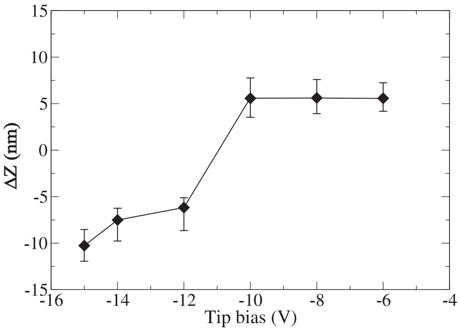

Figure 4.7: Voltage dependence of the height (depth) of the patterns created by the conductive AFM tip on a hydrogen-terminated diamond surface.

in agreement with previous observations [226]. On the other hand, the patterns that appear as pits have a tendency to become deeper for larger absolute values of the AFM tip voltage. Further investigation is needed in order to fully understand this behavior. For the elevated patterns we observe a higher elevation than can be expected as the result of replacement of hydrogen atoms by oxygen atoms, similar to the situation described in Ref. [197]. This can be explained by the difference in adsorbate thickness since a hydrogenated diamond surface is hydrophobic and an oxidized diamond surface is hydrophilic [197]. The mechanism causing the inscribed patterns is not completely clear. These patterns may be obtained either through mechanical scratching or by some kind of electrochemical process. Recently, Rezek et al. reported on the removal of a non-diamond surface layer by contact AFM [223]. Of course, we can not exclude this possibility as a simple explanation for the AFM tip induced scribing. However, unlike in Ref. [223] we do not observe any surface modification by contact AFM imaging even when the AFM tip is pressed against the surface with a force of about 300 nN during scanning. A non-diamond layer may be present due to the specific growth conditions of the CVD film. Our results reveal that both types of patterns can be observed for samples that are prepared at different growth conditions, including at elevated microwave frequency plasma power. We note that our monitoring of the dc current during the AFM modification process in both cases reveals a relatively stable (same order of magnitude) current flow (∼ 10 nA). This observation supports an elec-

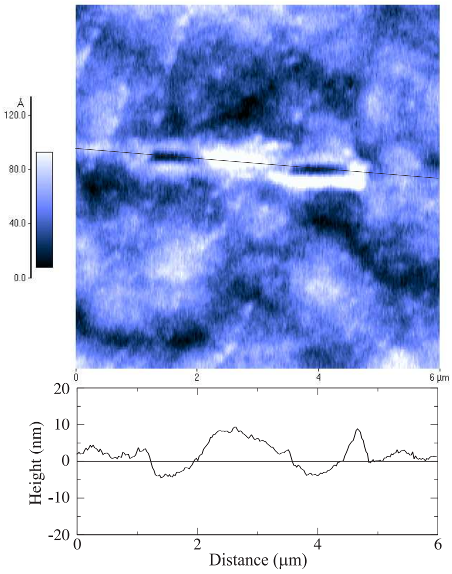

Figure 4.8: Three-dimensional submicrometer structure on a diamond surface (IMO4 from Table 3.1) created by local AFM modification.

trochemical origin for both AFM modification processes. Thermally activated reactions similar to the ones reported in Ref. [227] and Ref. [228] can promote the electrochemical processes. Simulations of the temperature distribution in the AFM tip-sample contact region [228] show that the local current induces a heating effect of several hundreds of degrees. Provided that the current produces such a significant heating, local thermal oxidation followed by removal of the soft products resulting from the oxidation upon scanning becomes possible. The depth increase at higher bias voltage supports this simple physical picture. Clearly, further investigation is needed to understand the observed surface modification, in particular the unusual case of scribing with a sensitive soft silicon AFM tip into an extremely rigid diamond surface.

The ability of creating both elevated and inscribed patterns on the same surface provides the possibility to fabricate various three-dimensional features at submicrometer scale. Figure 4.8 shows the patterns we have obtained on a diamond surface by applying a voltage of $-8\,\mathrm{V}$ for the elevated lines and

−12 V for the inscribed ones. The humidity was stabilized within the range 65% − 68%. Relying on this approach, nanofabrication of electronic devices on a hydrogen-terminated diamond surface can be achieved. Furthermore, the EFM system is used for analysis of the results of the local anodization process.

In Fig. 4.6(b) the EFM image of the area corresponding to the area in Fig. 4.6(a) is shown. One can clearly see the difference in surface potential between the hydrogen-terminated surface and the AFM modified area. Both square features (Fig. 4.6(a)) reveal an SP that is lower than for the non-treated hydrogen-terminated surface. The average SP difference is 150 ± 50 mV for the elevated square feature and 100 ± 50 mV for the inscribed square feature. These values are in agreement with the surface potential difference between hydrogenated and AFM oxidized areas reported in Ref. [161].

4.4 EFM characterization of the submicrometer structure

We have performed EFM measurements in order to characterize the conductivity of the hydrogenated patterned structure, which was obtained using the photolithography technique described in the previous section. For these measurements we have used the sample labeled IMO5 in Table 3.1. In Fig. 4.9 an EFM image of a fragment of the patterned line structure is shown. One can see that the line structure has a different surface potential compared to the oxidized diamond surface. The SP difference is around 150 mV, which is in agreement with the surface potential difference between hydrogenated and AFM-oxidized areas reported in Ref. [161].

Then, we have used EFM to visualize the electrical voltage distribution in the current-carrying H-terminated structure (see Fig. 4.10-a). One can see a gray-scale contrast gradient from the top side to the bottom side of the line. This is the result of the voltage drop due to the resistive properties of the H-terminated diamond film. The linear voltage drop in H-terminated diamond structure (Fig. 4.10-b) indicates that this layer behaves as a diffusive conductor with a defined value of the sheet resistance. This measurement is also a proof that the created structure is highly conductive, while the rest of the sample is insulating. Therefore, the structures obtained by our photolithography technique can be used further for transport properties measurements.

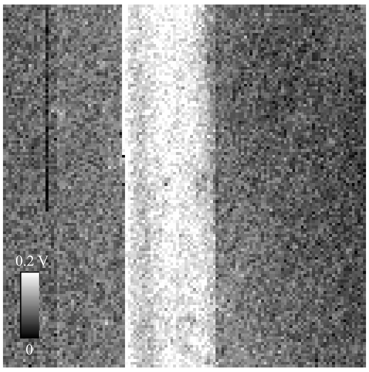

Figure 4.9: $50 \times 50\,\mu\mathrm{m}^2$ EFM image of the conductive line structure on the H-terminated diamond surface obtained by photolithography ($V_{dc} = 0$).

In order to interrupt the conductive line structure we have locally oxidized it using an AFM operating in contact mode, by applying a negative voltage of $-10\,\mathrm{V}$ to the tip at 50% air humidity. The AFM tip was scanned along the line perpendicular to the structure. The scan range was about $20\,\mu\mathrm{m}^2$, which is two times larger than the width of the line. In this way we were able to interrupt the conductive line (Fig. 4.11-(a)). From the voltage profile in Fig. 4.11-(b) one can clearly see that the current does not flow anymore through the patterned line after the interruption by AFM oxidation. The width of the insulating region obtained by AFM oxidation can be evaluated as $0.3\,\mu\mathrm{m}$. This demonstrates that using our AFM based local oxidation technique, we are able to create submicrometer insulating line structures on the conductive H-terminated diamond surface. On the other hand EFM could be a very useful tool for identifying the interruptions present in the electronic devices.

In Fig. 4.12 the EFM image of the locally modified line from Fig. 4.11-(a) without any current flow is shown. The difference in surface potential between the hydrogen-terminated structure and the AFM modified area is clearly visible. This image reveals a higher SP for the hydrogen terminated structure than for the locally modified area.

We have seen in this section that EFM is a useful technique to characterize the surface conductivity of current carrying H-terminated diamond line. The linear drop of the potential in highly conductive H-terminated diamond struc-

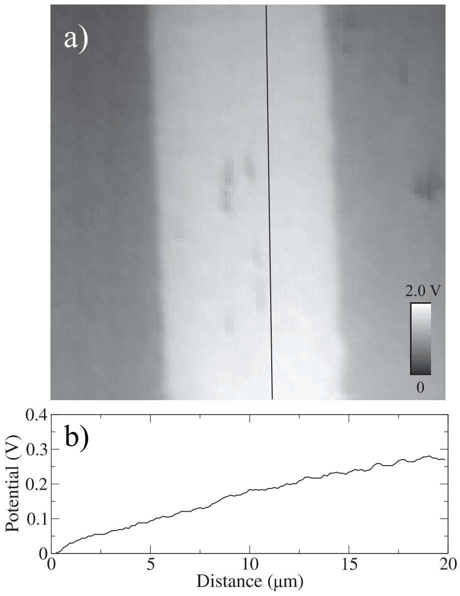

Figure 4.10: $20 \times 20\,\mu\mathrm{m}^2$ EFM image of the current-carrying line structure microfabricated on the H-terminated diamond surface ($V_{dc} = 1\,\mathrm{V}$) (a) and the corresponding voltage profile along the line structure (b).

ture indicates that the line behaves as diffusive conductors with a well defined value of the sheet resistance. Additionally, the highly conductive H-terminated diamond line reveals a uniform SP distribution.

Our EFM method is also very useful to probe the contact resistance and to locate interruptions in the conductivity of devices that are fabricated on an H-terminated diamond film surface by lithographic patterning (see Sec. 4.4).

4.5 Electrical transport properties of hydrogenated diamond surface

The combination of surface hydrogen termination and the presence of surface adsorbates produces the accumulation of holes in a surface channel [45, 229], where carrier concentrations up to $5 \cdot 10^{13}\,\mathrm{cm}^{-2}$ have been reported [54]. Thin

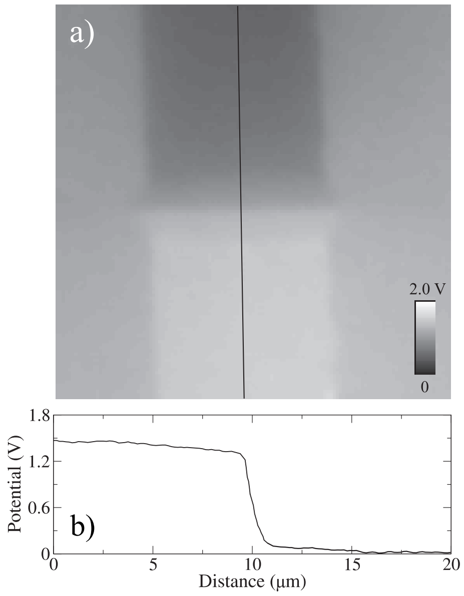

Figure 4.11: $20 \times 20\,\mu\mathrm{m}^2$ EFM image of the current carrying ($V_{dc} = 1\,\mathrm{V}$) locally oxidized line structure using an AFM tip (a) and the corresponding voltage profile along the line structure (b).

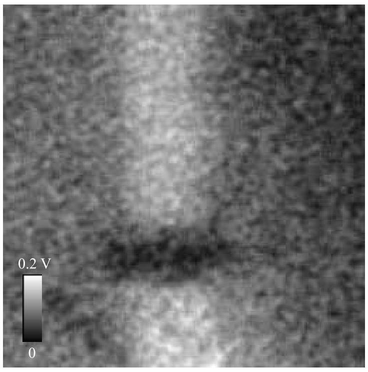

Figure 4.12: $40 \times 40\,\mu\mathrm{m}^2$ EFM image of the conductive line after the interruption, without any current flow ($V_{dc} = 0$), which maps surface potential. The bright region corresponds to H-terminated, while the darker region corresponds to O-terminated area.

conducting layers, in which the motion of the charge carriers (the holes in the case of the H-terminated diamond surface) is restricted to two spatial dimensions, are referred to as two-dimensional (2D) electron (or hole) gases. Because of the strong electric fields perpendicular to the surface, the holes are expected to form a 2D channel in the close vicinity of the H-terminated diamond surface. Therefore, the presence of charged surface adsorbates and structural defects is expected to play an important role for the transport and scattering of holes in the surface channel. Moreover, a laterally inhomogeneous hydrogen termination of the diamond surface should have a similar effect as the surface adsorbates. As a result, important surface potential fluctuations are expected and might even lead to charge carrier localization which is a property of disordered systems. By performing Hall effect experiments it has been shown that at temperatures above 70 K the hole density is almost constant, while the hole mobility increases by two orders of magnitude [48]. In the temperature interval $70\,\mathrm{K} < T < 200\,\mathrm{K}$ the mobility is exponentially activated with an activation energy of 22 meV, while at higher temperatures it follows a $T^{3/2}$ power law [48].

Nebel et al. [54] have shown that the mobility of holes exhibits a minimum around a critical temperature between 20 K and 70 K, increasing towards higher temperatures and even more strongly towards lower temperatures. The sheet hole density depends weakly on temperature above the critical temperature, while below this temperature carriers freeze out [54]. On the other hand, Garrido et al. [203] found no critical temperature for mobility or sheet hole density: the mobility increases with temperature in the interval $30\,\mathrm{K} - 300\,\mathrm{K}$, while the sheet hole density remains almost constant. The mobility and conductivity are exponentially activated with almost identical activation energies.

At low temperatures the experimental results [203] are in agreement with the theoretical prediction for thermally activated electrical conduction via variable range hopping. This particular regime of conduction was first considered by Mott [230]. At sufficiently low temperatures, where the thermal energy is not sufficient to excite electrons from the spatially localized to the spatially extended states, the dominant conductance mechanism will be thermally activated tunneling between localized states (variable-range hopping), which results in a temperature dependence of the conductivity that for a 2D system is [231]:

$$\sigma = \sigma_0 \cdot e^{-(T_0/T)^{1/3}} \tag{4.1}$$

where σ_0 is only weakly dependent on temperature. This is Mott's famous

$T^{-1/3}$ law for variable range hopping in a 2D system.

It is very important to note that concepts such as the Mott variable range hopping can be verified experimentally only for samples with strong, exponentially localized electron states, i.e., for samples that are well into the insulating regime. Less disordered samples with higher carrier concentration need to be treated as metallic samples with "weakly localized" electron states, i.e., the localization effects can be described in terms of a weak perturbation starting from a pure metallic state [232, 233]. The weak localization is to be distinguished from strong localization, often also referred to as Anderson localization [234], which is the absence of diffusion of electron waves in a sufficiently disordered medium.

The origin of the weak localization can be linked to the diffusive character of the electronic motion, which results from the frequent, random elastic scattering at impurities and defects. Quantum-mechanically there occurs a constructive interference between electron waves that are backscattered around a closed path in the clock-wise and counter-clockwise direction. Due to the fact that the two interfering waves follow the same path, but in reversed time order, the phase difference is always equal to zero. Consequently, the interference is always constructive and survives in samples with macroscopic dimensions. At higher temperatures, the interference processes are limited by inelastic scattering: the size of the backscattered electron paths is limited by the inelastic diffusion length that is determined by inelastic scattering at phonons and at other electrons. The weak localization therefore results in an increase of the resistance with decreasing temperature. Since the backscattering effects become more pronounced for samples with reduced dimensionality, the weak localization effects are more easily observable for lower dimensionality. For $D = 2$ the sheet resistance increases logarithmically with decreasing temperature. The logarithmic divergence will become more pronounced by the increased Coulomb repulsion between the charge carriers, which is enhanced by the diffusive electron motion.

A clear, unique signature of the weak localization is the appearance of an anomalous negative magnetoresistance that appears at relatively low magnetic fields and results from the breaking of the time-reversal symmetry by a magnetic field perpendicular to the 2D system [232, 235]. The perpendicular magnetic field gives rise to additional phase shifts of the interfering electron waves (Aharonov-Bohm effect), resulting in a destruction of the weak localization. A parallel field has a much smaller influence on the interference processes, resulting in a pronounced anisotropy of the negative magnetoresistance.

Obviously, in our case it has no sense to study localization effects in the 2D hole gas for the samples with very high sheet resistance. Our EFM measurements, which have been discussed in the previous chapter, clearly reveal that the conduction process becomes strongly inhomogeneous on larger length scales. We therefore limit our analysis of the electrical transport properties to the samples with sheet resistance around $10\,\mathrm{k}\Omega/\square$. However, for $D = 2$ the transition between weak and strong localization occurs for a sheet resistance around $30\,\mathrm{k}\Omega/\square$. Because our homogeneous samples with diffusive charge transport are very close to this transition, we can only perform a qualitative analysis of our experimental results. At higher temperatures an analysis in terms of weak localization appears to be more appropriate, while at low temperatures, where the sheet resistance can become considerably higher than $30\,\mathrm{k}\Omega/\square$, an analysis in terms of strong localization appears to be more appropriate.

Below we present and discuss the experimental results for the temperature dependence of the resistance, the magnetoresistance and the Hall effect for a selection of samples with a sheet resistance that is around $10\,\mathrm{k}\Omega/\square$ at room temperature. This will provide direct information on the use of the 2D hole gas for device applications.

Plain hydrogenated CVD diamond layers

The following measurements were performed on two different samples: a homoepitaxial single crystal CVD diamond grown at IMO (IMO2) and a single crystal CVD diamond (MCC) supplied by the Element Six company. The samples are glued to the sample holder (see Fig. 2.21) and the electrical contacts are made by ultrasonic wire bonding with $30\,\mu$m diameter aluminium wires. Four-point resistance measurements are performed with a nanovoltmeter (Hewlett Packard 34420A) and a programmable current source (Keithley 220). The measured voltage is averaged over both positive and negative polarities of the injected current in order to eliminate thermal or offset voltages when using the nanovoltmeter. Typically a current between $10\,\mu$A and $100\,\mu$A is used. We have performed resistance and magnetoresistance measurements on both samples, and Hall effect measurements on the MCC sample in a vacuum of 10^{-6} mbar.

For the Hall measurements we applied magnetic fields between 1 T and 10 T. The measurements were performed in a cryostat where the temperature could be varied between 1.5 K and 300 K without breaking the vacuum. Using the van der Pauw method and the two configurations depicted in Fig. 2.20, we have determined the sheet resistance R_s from the equation:

$$R_s = \frac{\pi(R_A + R_B)}{2\ln 2} \tag{4.2}$$

The sheet resistance has a room temperature value of about $6\,\mathrm{k}\Omega/\square$ for IMO2 and $10\,\mathrm{k}\Omega/\square$ for the MCC sample and increases with decreasing temperature. The increase is weaker at high temperatures and becomes much more pronounced at low temperatures (Fig. 4.13). The insets of Fig. 4.13 show the sheet resistance dependence as a function of the logarithm of temperature. The variation of the sheet resistance is consistent with a logarithmic divergence. As discussed above, such a divergence of the resistance is typical of a 2D disordered conductor and indicates weak localization of the charge carriers [236, 237].

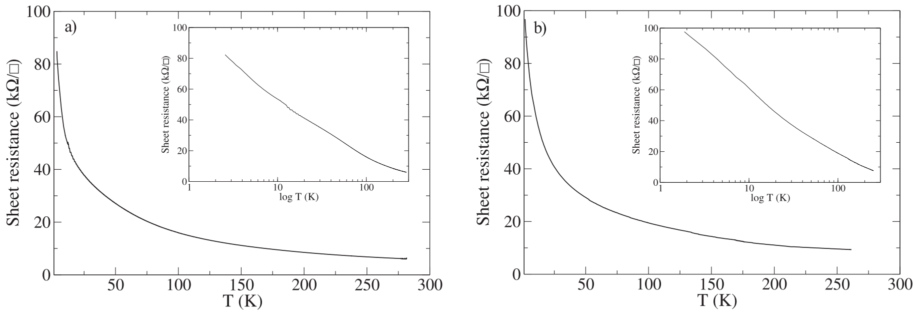

Figure 4.13: Sheet resistance of the H-terminated diamond sample plotted as a function of temperature: (a) Sample IMO2 from IMO; (b) Sample MCC from Element Six. Insets: The same data plotted as a function of the logarithm of temperature.

Since our samples are close to the transition towards strong localization, we also try to interpret our results in terms of strong localization and therefore also analyze the temperature dependence of the 2D sheet conductivity σ_s of the hydrogenated diamond samples. As can be seen in Fig. 4.14, σ_s varies between $2 \cdot 10^{-5}$ and $2 \cdot 10^{-4}\,\Omega^{-1}$ for IMO2 and between $10^{-5}$and $10^{-4}\,\Omega^{-1}$ for MCC.

When plotting the logarithm of the conductivity as a function of $1/T$, we observe a saturation of the conductivity at lower temperatures, indicating that a simple analysis in terms of exponential activation of the conduction process fails. On the other hand, for higher temperatures ($> 90\,\mathrm{K}$) the temperature dependence of the conductivity seems to agree with a thermally activated behavior that is consistent with strong localization. The activation energies are 13.1 meV (IMO2) and 11.3 meV (MCC) at higher temperatures, while at lower temperatures the conductivity is exponentially activated with an activation energy of 3.3 meV (IMO2) and 2.7 meV (MCC). From Fig. 4.14 we conclude that an analysis in terms of strong localization does not make too much sense. First, the barriers for the thermally activated transport become smaller at lower temperatures, while the opposite behavior is expected. Second, the fitted barrier heights are comparable to the available thermal energy $k_B T$, while the thermal energy needs to be much smaller than the barrier height for a reliable analysis.

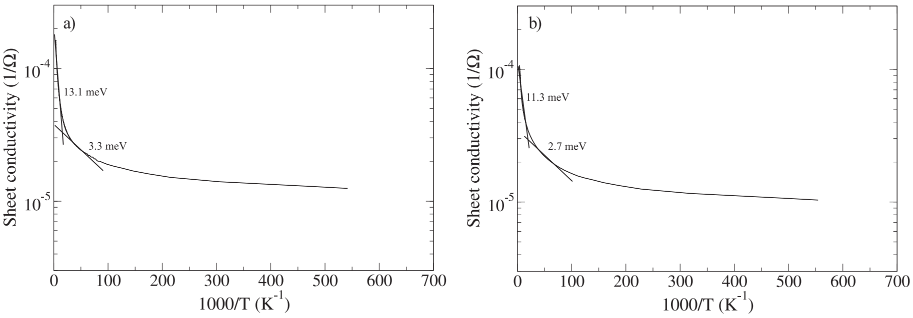

Figure 4.14: Temperature dependence of the conductivity: (a) The sample IMO2 from IMO; (b) The sample MCC from Element Six.

Using the configuration shown in Fig. 2.19 we have measured the Hall voltage for the MCC sample at seven different temperatures: 1.6 K, 4.5 K, 14.5 K, 25 K, 60 K, 120 K and 240 K. The measurements are performed with constant current $I = 10\,\mu\mathrm{A}$ and in a magnetic field applied perpendicular to the plane of the sample. From these measurements we can then calculate the sheet carrier density and the Hall mobility for our sample using Eqs. 2.23 and 2.29, respectively. From Fig. 4.15 we find that the sheet carrier density increases by one order of magnitude at high temperatures (up to $3 \cdot 10^{12}\,\mathrm{cm}^{-2}$), and appears to

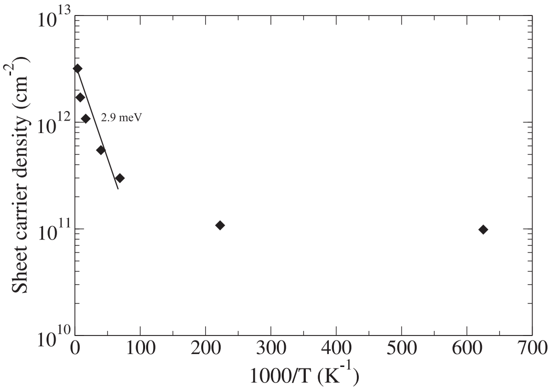

Figure 4.15: Sheet carrier density inferred from Hall effect measurements at different temperatures. The applied current was $I = 10\,\mu$A and the magnetic field $B = 10\,$T was applied perpendicular to the plane of the sample.

be exponentially activated with an activation energy of 2.9 meV. At lower temperatures the carrier density tends to saturate. Knowing the carrier density, we can calculate the Hall coefficient using Eq. 2.24. A positive Hall coefficient is obtained, confirming that holes are indeed dominating the electrical transport properties. Again, we note that an analysis in terms of exponentially activated transport is not relevant in view of the too small barrier heights.

The Hall mobility is between 200 and 600 $\mathrm{cm}^2/\mathrm{Vs}^{-1}$ (Fig. 4.16) and above 10 K the logarithm of the hall mobility scales with $T^{-1/3}$ (inset of Fig. 4.16), a dependence that in principle is consistent with Mott variable range hopping for $D = 2$ [231]. We should, however, consider the agreement with Mott's prediction rather as accidental. Indeed, variable range hopping is expected only for samples with strong localization and should become more dominant at lower temperatures.

The disorder in our 2D hole gas can be related to lateral inhomogeneities at the nanometer scale of the hydrogen termination of the diamond surface as well as the presence of charged surface adsorbates and structural defects [203]. Electrical transport at the hydrogen terminated diamond surface may then be described in terms of the models for localization of holes moving in a system with potential fluctuations associated with the microscopic inhomogeneities. Indeed, in our EFM images (Fig. 4.10) we do not observe any fluctuations of the

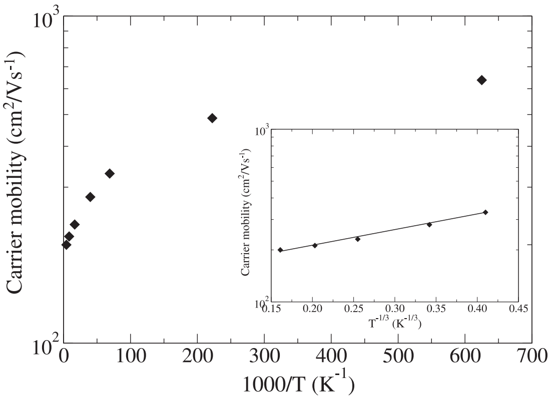

Figure 4.16: Temperature dependence of the hole mobility calculated from Hall experiments in a magnetic field $B = 10\,\mathrm{T}$ and using a current of $I = 10\,\mu\mathrm{A}$. Inset picture: temperature dependence of the hole mobility plotted versus $T^{-1/3}$ ($T > 10\,\mathrm{K}$).

SP down to about 70 nm, i.e., the spatial resolution of our EFM measurements. SP fluctuations should therefore occur on a smaller (nanometer) scale.

As indicated above, magnetoresistance (MR) measurements present a unique method to detect the presence of 2D localization effects in disordered metallic systems. A magnetic field B should destroy the interference of the backscattered charge carrier waves and result in a decrease of the resistance (negative MR) at relatively low fields.

We have performed MR measurements for the IMO2 sample as well as for the MCC sample. The magnetic field has been applied in two directions: parallel and perpendicular to the plane of the sample. The measurements were performed at a constant temperature of 10 K while applying a current of $10\,\mu$A. A pronounced anisotropy is clearly observed when comparing the results of the two measurements in Figs. 4.17-4.18. The anisotropy of the MR clearly confirms the 2D character of the electrical transport properties: the orbital motion of the holes is strongly affected by a magnetic field perpendicular to the 2D layer, while the orbital motion remains unaffected for a magnetic field parallel to the 2D hole gas layer. The positive MR that appears at very high fields and dominates the MR for a parallel field can be related to the disorder enhanced Coulomb repulsion between charge carriers and results from the Zeeman splitting of the spin-up and spin-down charge carriers. The positive MR is also present for a perpendicular field, but in that case only results in a saturation of the MR at very high fields due to the competition with the negative MR resulting from the localization effect.

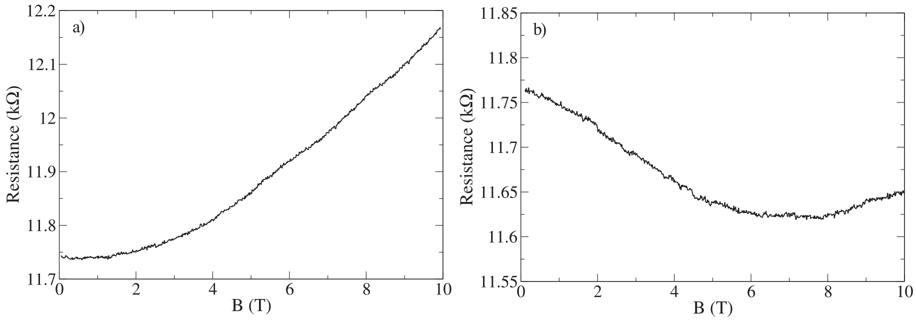

Figure 4.17: The magnetoresistance data obtained at 10 K for a magnetic field oriented parallel to the IMO2 sample (a) and perpendicular to the plane of the IMO2 sample (b).

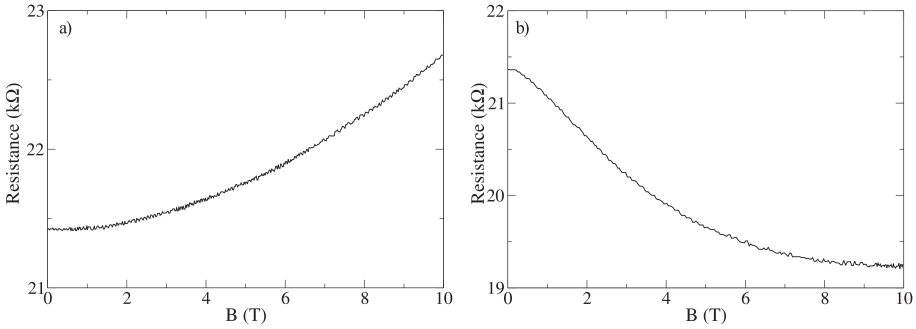

Figure 4.18: The magnetoresistance data obtained at 10 K for a magnetic field oriented parallel to the MCC sample (a) and perpendicular to the plane of the MCC sample (b).

Patterned structures

Furthermore, we have patterned the MCC sample as described in Sec. 4.2 and we have performed EFM and resistance measurements before and after local

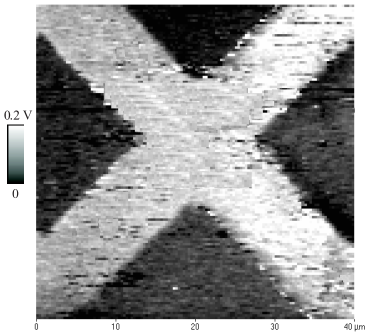

Figure 4.19: $40 \times 40\,\mu\mathrm{m}^2$ EFM image of the conductive cross structure patterned on the H-terminated surface by photolithography technique ($V_{dc} = 0$).

AFM modification. Fig. 4.19 shows the work function image of the conductive cross created on the sample. It can be seen that the cross structure has a different surface potential compared to the diamond surface. According to Ref [161], the brighter cross correspond to the H- terminated surface, while the darker areas correspond to the O-terminated surface. The SP difference is around 150 mV, similar to what we observed before on the patterned line (Section 4.4). In the next step we have applied a DC current ($V_{dc} = 2\,\mathrm{V}$) in order to visualize the electrical voltage distribution in the current-carrying H-terminated structure (Fig. 4.20). It can be seen that the current flows only along the bright lines, which represent the conductive H-terminated areas. The resistive properties of the H-terminated diamond film structure can be observed from the voltage drop seen in the voltage profile (Fig. 4.20-b). The linear voltage drop is an indication that the H-terminated structure behaves as diffusive conductors with a well defined value of the sheet resistance.

Using an AFM operating in contact mode, we have locally oxidized the conductive cross. We have applied a negative voltage of $-14\,\mathrm{V}$ to the tip at 65% air humidity. In this way we have created a $8 \times 8\,\mu\mathrm{m}^2$ square in the middle of the cross. From the work function image (Fig. 4.21) we can see that this locally modified square region has an identical work function to the oxidized areas of the sample.

In order to characterize the local electric properties of the AFM-modified structure we switch our advanced AFM setup to EFM mode of operation. By

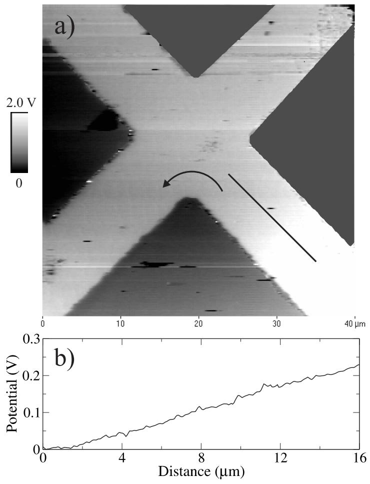

Figure 4.20: (a) 40 × 40 μm^2 EFM image of the current-carrying structure patterned on H-terminated diamond surface (V_{dc} = 2 V). The arrow indicates the direction of the applied current; (b) The voltage profile corresponding to the line drawn in (a).

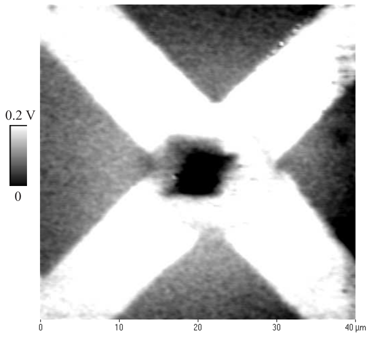

Figure 4.21: 40 × 40 μm^2 EFM image of the cross structure after the AFM modification ($V_{dc} = 0$).

applying again a DC voltage of 2 V between two adjacent lines forming the cross structure (other two lines are not connected), we can visualize the electrical voltage distribution in the AFM-modified structure (Fig. 4.22). Similar to the situation before the AFM modification, the voltage drops linearly along the direction of the current flow (line B in Fig. 4.22-c), while along a direction where the cross sectional area of the conductive layer is smaller (line A) the drop of potential is higher (Fig. 4.22-b). Other parts of the cross structure remain correspondingly equipotential because no current is flowing through the corresponding conductive lines. Based on our EFM characterization of the modified structure we can conclude that after modification an essential part of the total structure resistance is concentrated in the constriction created by the AFM-anodization process. This provides a nice possibility to investigate the electrical transport properties of nanometer size conductive regions fabricated on the H-terminated surface and compare these transport properties to the properties of micrometer size regions.

Figure 4.23 shows plots of the temperature dependence of the resistance of the H-terminated cross structure before the AFM modification and after the AFM modification. As it can be seen from Fig. 4.23, the resistance increases by more than 1 MΩ after the AFM modification (which is more than 100%) and it also reveals a more pronounced temperature dependence especially at lower temperatures. Note that in general the variations of the resistance with temperature for both cases are similar and behave typically for a 2D disordered conductor. The difference in temperature dependencies can be explained by the fact that for a smaller region the localization effects manifest themselves much more strongly because of the reduced system size while keeping the disorder fixed.

The sub-micrometer conductive structure we have obtained, by combining photolithography and AFM local modification, can be used in electronic device applications.

4.6 Summary

We have succeeded to locally modify the hydrogenated surface of the CVD-grown diamond films using a conductive AFM tip. By varying the voltage, both elevated and carved patterns could be obtained and “in situ” characterized by

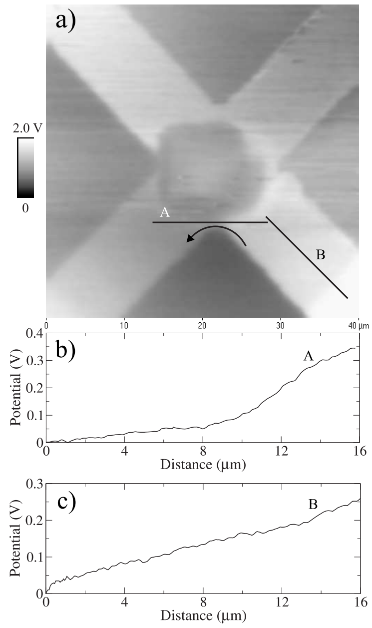

Figure 4.22: (a) $40 \times 40\,\mu\text{m}^2$ EFM image of the current-carrying H-terminated diamond structure after the AFM modification ($V_{dc} = 2\,\text{V}$). The arrow indicates the direction of the applied current; (b) The voltage profile corresponding to the lines A and B drawn in (a).

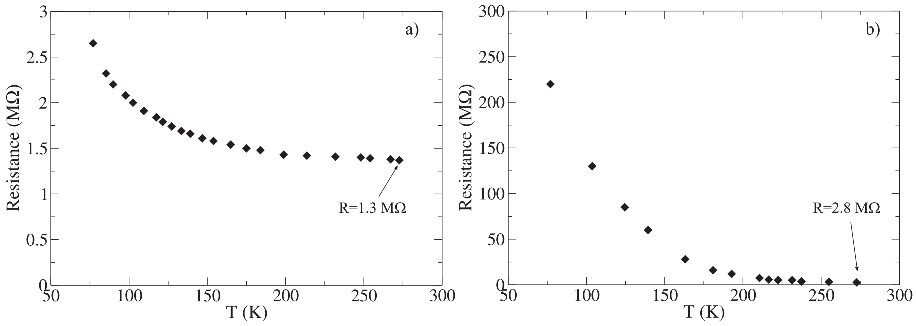

Figure 4.23: Temperature dependence of the resistance of the structure prepared by patterning the hydrogen surface in form of the cross: (a) before the AFM modification and (b) after the AFM modification.

EFM. From the EFM images a different work function could be inferred for the modified structures when compared to the hydrogenated surface. Combining the photolithography and the plasma oxidation techniques, we were able to create conductive structures on the CVD diamond surface. With the conductive AFM tip we are able to create sub-micrometer scale structures on the hydrogen-terminated layer. The conductive properties of the obtained structure were investigated by using EFM. In this way we could see that the structure has a different work function than the oxygen plasma treated areas and we could confirm that the obtained H-terminated structure is conductive. We have used EFM to visualize the electrical voltage distribution in the current-carrying H-terminated structure. The linear voltage drop in the H-terminated diamond narrow-line structure indicates that this layer behaves as a diffusive conductor with a well defined value of the sheet resistance. We demonstrate that our EFM method is very useful to locate interruptions in the conductivity of devices that are fabricated on an H-terminated diamond film surface by lithographic patterning.

Electrical transport measurements were performed in order to study the electronic properties of the created structure. Electrical transport of the H-terminated diamond surface structures is analyzed qualitatively. Our analysis is based on the models for localization of holes moving in a disordered system with potential fluctuations associated with nanometer scale inhomogeneities of the hydrogen termination of the diamond surface as well as with the presence of charged surface adsorbates and structural defects.

The temperature variation of the sheet resistance is consistent with a logarithmic divergence, which is typical of a 2D disordered conductor and indicates weak localization of the charge carriers. The magnetoresistance curves obtained at different orientations of the magnetic field reveal a strong anisotropy. The anisotropy of the magnetoresistance clearly confirms the 2D character of the electrical transport properties: the orbital motion of the holes is strongly affected by a magnetic field perpendicular to the 2D hole gas layer, while the orbital motion remains unaffected for a magnetic field parallel to the 2D hole gas layer. The positive MR, which appears at very high fields and dominates the magnetoresistance for a parallel field, can be related to the disorder enhanced Coulomb repulsion between the charge carriers and results from the Zeeman splitting of the spin-up and spin-down charge carriers.

Conclusions

In CVD diamond, an electrically insulator, a highly conductive surface layer with quasi-two dimensional (2D) hole gas characteristics can be obtained by hydrogen termination. Electrical properties of this conductive layer can be controlled by changing surface hydrogen termination to oxygen termination. Although the properties of diamond conductive surface layers have been used in different prototype devices such as Schottky diodes and field-effect transistors, the mechanism behind the surface conductivity is far from being fully understood. To investigate the potential device applications of the diamond surface local electrical characterization and modification are crucial. The aim of the present thesis is the nanoscale characterization and modification of the electronic properties of hydrogen terminated diamond surfaces. In order to pattern hydrogen-terminated (H-terminated) diamond surfaces down to the nanometer scale we combine photolithography and local anodic oxidation, using an atomic force microscope (AFM). Another goal of the thesis was to investigate the transport properties of the holes in conductive channels at the surface of the hydrogenated diamond surface.

The films were prepared by chemical vapor deposition (CVD). We have characterized the hydrogenated diamond surface in order to optimize the preparation procedure of the samples suitable for large and small scale lithography, and for creating submicrometer structures used for further electrical characterization. We performed AFM surface characterization of CVD diamond samples, that were grown at different conditions. The growth parameters and hydrogenation process time were optimized in order to satisfy the requirements of the lithographic processing on both micrometer and nanometer scale. The effects of mechanical polishing and the hydrogen plasma etching on the surface roughness were also investigated. We used scanning tunneling microscopy in ultra-high vacuum as a suitable tool for studying the properties of the CVD diamond surface at the atomic level. The direct observation of a (2×1) surface reconstruction due to dimerization evidenced the high quality of the crystalline surface layer.

We discussed the fabrication of the conductive structures on the H-terminated diamond surface. We succeeded to locally modify the hydrogenated surface of diamond films with a conductive AFM tip. By varying the voltage, which is applied to the tip, both elevated and inscribed patterns can be obtained and "in situ" characterized by electrical force microscopy (EFM). From the EFM images a different work function can be inferred for the parts of the surface that have been modified when compared to the hydrogenated surface. For the elevated features there is no voltage dependence of the "AFM writing" process, while for the inscribed features a weak voltage dependence is observed. This dependence can be explained by the fact that a higher voltage induces a higher local temperature, making easier the removal of the non-diamond layer formed during the electrochemical oxidation process. With the conductive AFM tip we are able to create three-dimensional structures with lateral size in the submicrometer regime. This opens the possibility for nanofabrication of electronic devices by local anodic oxidation, of the H-terminated diamond surface, and also tune the vertical dimension by varying the depth or height of the created features.

The EFM was adapted to characterize the surface conductivity of current carrying H-terminated diamond films. The almost linear drop of the voltage for a highly conductive layer indicates that such layers behave as diffusive conductors with a well defined value of the sheet resistance. On hydrogen-terminated diamond surfaces with poor electrical conductivity we observe obstruction of the current flow in particular regions. The coexisting conductive and insulating regions are characterized by a different surface potential. Our EFM based local electrical measurements, which have been developed for current-carrying hydrogen-terminated diamond films, can also be used to identify local interruptions in the conductivity of diamond film devices fabricated by lithographic patterning. By combining two techniques, i.e. large scale standard photolithography and AFM local anodic oxidation we obtain conductive sub-micrometer structures, which are analyzed by AFM and EFM and then used for the electric transport measurements. Photolithographic patterning of the hydrogenated

CVD diamond has been achieved using a double layer resist method. Using this method, patterns with lateral dimensions as small as 1 μm were obtained.

Detailed electrical transport measurements as a function of temperature and magnetic field, before and after local modification (anodization) with AFM of photolithographically patterned diamond films were performed. The observed variation of the resistance with temperature is consistent with the logarithmic divergence of the sheet resistance, which is typical of a 2D disordered conductor and corresponds to weak localizations of charge carriers. We were able to verify the quasi 2D behavior by measuring the pronounced anisotropy of the magnetoresistance at liquid helium temperatures, and to attribute this anisotropy to 2D weak electron localization.

Bibliography

[1] A. El Goresy and G. Donnay, *A new allotropic form of carbon from the ries crater*, Science **161** (1968), 363.

[2] P. Fallon, V. S. Veerasamy, C. A. Davis, J. Robertson, W. I. Milne G. A. J. Amaratunga, and J. Koskinen, *Properties of filtered-ion-beam-deposited diamondlike carbon as a function of ion energy*, Phys. Rev. B **48** (1993), 4777.

[3] A. A. Voevodin and M. S. Donley, *Preparation of amorphous diamond-like carbon by pulsed laser deposition: A critical review*, Surf. Coat. Technol. **82** (1996), 199.

[4] P. C. Kelires, *Structural properties and energetics of amorphous forms of carbon*, Phys. Rev. B **47** (1993), 1829.

[5] N. B. Brandt, S. M. Chudinov, and Y. G. Ponomarev, *Semimetals 1: Graphite and its compunds*, North-Holland, Amsterdam, 1988.

[6] K. S. Novoselov, A. K. Geim, S. V. Morozov, D. Jiang, Y. Zhang, S. V. Dubonos, I. V. Grigorieva, and A. A. Firsov, *Electric field effect in atomically thin carbon films*, Science **306** (2004), 666.

[7] N. W. Ashcroft and N. D. Mermin, *Solid state physics*, Harcourt College, Orlando, 1976.

[8] X. Zhou, G. D. Watkis, K. M. McNamara Rutledge, R. P. Messmer, and S. Chawla, *Hydrogen-related defects in polycrystalline CVD diamond*, Phys. Rev. B **54** (1996), 7881.

[9] C. Frondel and U. B. Marvin, *Lonsdaleite, a hexagonal polymorph of diamond*, Nature **214** (1967), 587.

[10] K. E. Spear and John P. Dismukes, *Synthetic diamond: Emerging CVD science and technology*, Wiley-Interscience, New York, 1994.

[11] J. Singh, *Physics of semiconductors and their heterostructures*, McGraw-Hill, New York, 1993.

[12] I. Reineck, M. E. Sjostrand, J. Karner, and M. Pedrazzini, *Diamond coated cutting tools*, Int. J. Refract. Met. Hard Mater. **14** (1996), 187.

[13] J. Karner, M. Pedrazzini, I. Reineck, M. E. Sjostrand, and E. Bergmann, *CVD diamond coated cemented carbide cutting tools*, Mater. Sci. Eng. A **209** (1996), 405.

[14] P. J. Boudreaux, *Thermal aspects of high performance packaging with synthetic diamond*, Applications of Diamond Films and Related Materials: 3^{rd} International Conference (A. Feldmann, Y. Tzeng, W. A. Yarbrough, M. Yoshikawa, and M. Murakawa, eds.), NIST, Washington DC, 1995, p. 603.

[15] C. T. Troy, *AT-and-T claims 1st-commercial application of bonding diamond film to metal*, Photon. Spect. **26** (1992), 28.

[16] G. Lu, *Applications of CVD diamond in the thermal management*, Applications of Diamond Films and Related Materials: 2^{nd} International Conference (M. Yoshikawa, M. Murakawa, Y. Tzeng, and W.A. Yarbough, eds.), MYU, Tokyo, 1993, p. 269.

[17] D. P. Morgan, *Surface-wave devices for signal processing*, Elsevier, Amsterdam, 1985.

[18] A. Mainwood, L.Allers, A. T. Collins, J. F. Hassard, A. S. Howard, A. R. Mahon, H. L. Parsons, T. Sumner, J. L. Collinand G. A. Scarsbrook, and R. S. Sussmann A. J. Whitehead, *Neutron damage of chemical-vapor-deposition diamond*, J. Phys. D: Appl. Phys. **28** (1995), 1279.

[19] B. Dischler and C. Wild, *Low-pressure synthetic diamond*, Springer-Verlag, New York, 1998.

[20] X. Jiang, C. P. Klages, R. Zachai, M. Hartweg, and H. J. Füser, *Epitaxial diamond thin films on (001) silicon substrates*, Appl. Phys. Lett. **62** (1993), 3438.

[21] B. R. Stoner and J. T. Glass, *Textured diamond growth on (100) β-SiC via microwave plasma chemical vapor deposition*, Appl. Phys. Lett. **60** (1992), 698.

[22] M. Schreck, H. Roll, and B. Stritzker, *Diamond/Ir/$SrTiO_3$: A material combination for improved heteroepitaxial diamond films*, Appl. Phys. Lett. **74** (1999), 650.

[23] J. Furthmüller, J. Hafner, and G. Kresse, *Dimer reconstruction and electronic surface states on clean and hydrogenated diamond* (100) *surfaces*, Phys. Rev. B **53** (1996), 7334.

[24] G. Kern, J.Hafner, J. Furthmüller, and G. Kresse, *(*2×1*) reconstruction and hydrogen-induced de-reconstruction of the diamond (100) and (111) surfaces*, Surf. Sci. **352-354** (1996), 745.

[25] R. Graupner, M. Hollering, A. Ziegler, J. Ristein, L. Ley, and A. Stampfl, *Dispersions of surfaces states on diamond (100) and (111)*, Phys. Rev. B **55** (1997), 10841.

[26] Y. L. Yang and M. P. Develyn, *Theoretical studies of clean and hydrogenated diamond (100) by molecular mechanics*, J. Vac. Sci. Technol. A **10** (1992), 978.

[27] Th. Frauenheim, U. Stephan, P. Blaudeck, P. Porzeag, J. G. Bussmann, W. Zimmermann-Edling, and S. Lauer, *Stability, reconstruction and electronic properties of diamond (100) and (111) surfaces*, Phys. Rev. B **48** (1993), 18189.

[28] J. C. Zheng, X. N. Xie, A. T. S. Wee, and K. P. Loh, *Oxygen-induced surface state on diamond (100)*, Diamond Relat. Mater. **10** (2001), 500.

[29] Y. M. Wang, K. W. Wong, S. T. Lee, M. Nishitani-Gamo, I. Sakaguchi, K. P. Loh, and T. Ando, *Recent studies of diamond surfaces*, Diamond Relat. Mater. **9** (2000), 1582.

[30] X. M. Zheng and P. V. Smith, *The stable configurations for oxygen chemisorption on the diamond (100) and (111) surfaces*, Surf. Sci. **262** (1992), 219.

[31] F. Maier, J. Ristein, and L. Ley, *Electron affinity of plasma-hydrogenated and chemically oxidized diamond* (100) *surfaces*, Phys. Rev. B **64** (2001), 165411.

[32] G. Schober and O. Weis, *Highly resolved atomic (111) surfaces of synthetic type IIb diamond in air investigated by scanning tunnelinf microscopy using a lithium niobite scanner*, Surf. Sci. **383** (1997), 203.

[33] G. Kern, J.Hafner, J. Furthmüller, and G. Kresse, *Surface reconstruction and electronic properties of clean and hydrogenated diamond* (111) *surfaces*, Surf. Sci. **358** (1996), 422.

[34] K. C. Pandey, *New π-bonded chain model for Si (111)-(*2×1*) surface*, Phys. Rev. Letters **47** (1981), 1913.

[35] G. Kern, J. Hafner, and G. Kresse, *Atomic and electronic structure of diamond*(111) *surfaces .1. reconstruction and hydrogen-induced dereconstruction of the one dangling-bond surface*, Surf. Sci. **366** (1996), 445.

[36] K. P. Loh, X. N. Xie, S. W. Yang, J. S. Pan, and P. Wu, *A spectroscopic studies of the negative electron affinity of cesium oxide-coated diamond (111) and theoretical calculations of the surface density of states on oxyenated diamond (111)*, Diamond Relat. Mater. **11** (2002), 1379.

[37] G. Kern and J. Hafner, *Ab initio calculations of the atomic and electronic structure of clean and hydrogenated diamond* (110) *surfaces*, Phys. Rev. B **56** (1997), 4203.

[38] F. Maier, R. Graupner, M. Hollering, L. Hammer, J. Ristein, and L. Ley, *The hydrogenated and bare diamond* (110) *surface: a combined LEED-, XPS-, and ARPES study*, Surf. Sci. **443** (1999), 177.

[39] J. B. Cui, J. Ristein, and L. Ley, *Electron affinity of the bare and hydrogen covered single crystal diamond* (111) *surface*, Phys. Rev. Letters **81** (1998), 429.

[40] M. Yokoyama and T. Ito, *Dependence of the electron affinity of homoepitaxially grown CVD diamond on the amount of surface oxygen*, Appl. Surf. Sci. **162/163** (2000), 457.

[41] J. Robertson and M. J. Rutter, *Band diagram of diamond an diamind-like carbon surfaces*, Diamond Relat. Mater. **7** (1998), 620.

[42] M. I. Landstrass and K. V. Ravi, *Resistivity of chemical vapor deposited diamond films*, Appl. Phys. Lett. **55** (1989), 975.

[43] T. Maki, S. Shikama, M. Komori, Y. Sakaguchi, K. Sakuta, and T. Kobayashi, *Hydrogenating effect of single-crystal diamond surface*, Jap. J. Appl. Phys. **31** (1992), L1446.

[44] S. G. Ri, T. Mizumasa, Y. Akiba, Y. Hirose, T. Kurosu, and M. Iida, *Formation mechanism of p-type surface conductive layer on deposited diamond films*, Jap. J. Appl. Phys. **34** (1995), 5550.

[45] F. Maier, M. Riedel, B. Mantel, J. Ristein, and L. Ley, *Origin of surface conductivity in diamond*, Phys. Rev. Letters **85** (2000), 3472.

[46] K. Hayashi, S. Yamanaka, H. Okushi, and K. Kajimura, *Study of the effect of hydrogen on transport properties in chemical vapor deposited diamond films by Hall measurements*, Appl. Phys. Lett. **68** (1996), 376.

[47] J. A. Garrido, C. E. Nebel, M. Stutzmann, E. Snidero, and P. Bergonzo, *Capacitance-voltage studies of Al-Schottky contacts on hydrogen-terminated diamond*, Appl. Phys. Lett. **81** (2002), 637.

[48] C. Sauerer, F. Ertl, C.E. Nebel, M. Stutzmann, P. Bergonzo, O.A. Williams, and R.A. Jackman, *Low temperature surface conductivity of hydrogenated diamond*, Progr. Surf. Sci. **186** (2001), 241.

[49] S. G. Ri, K. Tashiro, S. Tanaka, T. Fujisawa, H. Kimura, T. Kurosu, and M. Iida, *Hall effect measurements of surface conductive layer on undoped diamond films in NO_2 and NH_3 atmospheres*, Jap. J. Appl. Phys. **38** (1999), 3492.

[50] H. J. Looi, R. B. Jackman, and J. S. Foord, *High carrier mobility in polycrystalline thin film diamond*, Appl. Phys. Lett. **72** (1998), 353.

[51] K. Tsugawa, K. Kitatani, H. Noda, A. Hokazono, K. Hirose, M. Tajima, and H. Kawarada, *High-performance diamond surface-channel field-effect transistors and their operation mechanism*, Diamond Relat. Mater. **8** (1999), 927.

[52] K. Hayashi, H. Watanabe, S. Yamanaka, H. Okushi, K. Kajimura, and T. Sekiguchi, *Hydrogen-related gap states in the near surface of chemical vapor deposited homoepitaxial diamond films*, Diamond Relat. Mater. **6** (1997), 303.

[53] O. A. Williams, M. D. Whitfield, R. B. Jackman, J. S. Foord, J. E. Butler, and C. E. Nebel, *Formation of shallow acceptor states in the surface region of thin film diamond*, Appl. Phys. Lett. **78** (2001), 3460.

[54] C. E. Nebel, C. Saurer, F. Ertl, and M. Stutzmann, *Hydrogen-induced transport properties of holes in diamond surface layers*, Appl. Phys. Lett. **79** (2001), 4541.

[55] H. Kawarada, *Hydrogen-terminated diamond surfaces and interfaces*, Surf. Sci. Rep. **26** (1996), 205.

[56] J. Ristein, M. Riedel, and L. Ley, *Electrochemical surface transfer doping - the mechanism behind the surface conductivity of hydrogen-terminated diamond*, J. Electrochem. Soc. **151** (2004), E315.

[57] K. Hayashi, S. Yamanaka, H.Watanabe, T. Sekiguchi, H. Okushi, and K. Kajiura, *Investigation of the effect of hydrogen on electrical and optical properties in chemical vapor deposited on homoepitaxial diamond films*, J. Appl. Phys. **61** (1997), 744.

[58] A. Denisenko, A. Aleksov, A. Pribil, P. Gluche, W. Ebert, and E. Kohn, *Hypothesis on the conductivity mechanism in hydrogen terminated diamond films*, Diamond Relat. Mater. **9** (2000), 1138.

[59] H. Gerischer, *Semiconductor electrochemistry*, Physical chemistry (H. Eyring, D. Henderson, and W. Jost, eds.), vol. 9A, Academic Press, New York, 1970, p. 463.

[60] J. B. Cui, J. Ristein, and L. Ley, *Dehydrogenation and the surface phase transition on diamond (111): Kinetics and electronic structure*, Phys. Rev. B **59** (1999), 5847.

[61] V. Chakrapani, J. C. Angus, A. B. Anderson, S. D. Wolter, B. R. Stoner, and G. U. Sumanasekera, *Charge transfer equilibria between diamond and an aqueous oxygen electrochemical redox couple*, Science **318** (2007), 1424.

[62] A. T. Collins and A. W. S. Williams, *The nature of the acceptor centre in semiconducting diamond*, J. Phys. C: Solid State Phys. **4** (1971), 1789.

[63] X. H. Wang, G. H. M. Ma, W. Zhu, J. T. Glass, L. Bergman, K. F. Turner, and R. J. Nemanich, *Effects of boron doping on the surface morphology and structural imperfections of diamond films*, Diamond Relat. Mater. **1** (1992), 828.

[64] P. Hartmann, S. Bohr, R. Haubner, B. Lux, P. Wurzinger, M. Griesser, A. Bergmaier, G. Dollinger, H. Sternschulte, and R. Sauer, *Diamond growth with boron addition*, Int. J. Refract. Met. Hard Mater. **16** (1998), 223.

[65] M. Hata, M. Tsuda, N. Fujii, and S. Oikawa, *Surface migration enhancement of adatoms in the photoexcited process on reconstructed diamond* (001) *surfaces*, Appl. Surf. Sci. **79-80** (1994), 255.

[66] P. Wurzinger, P. Pongratz, P. Hartmann, R. Haubner, and B. Lux, *Investigation of the boron incorporation in polycrystalline CVD diamond films by TEM, EELS and Raman spectroscopy*, Diamond Relat. Mater. **6** (1997), 763.

[67] J. C. Angus, Y. V. Pleskov, and S. C. Eaton, *Electrochemistry of diamond*, Semiconductors and semimetals **77** (2004), 97.

[68] R. Locher, J. Wagner, F. Fuchs, M. Maier, P. Gonon, and P. Koidl, *Optical and electrical characterization of boron-doped diamond films*, Diamond Relat. Mater. **4** (1995), 678.

[69] J. H. Edgar, Z. Y. Xie, and D. N. Braski, *The effects of the simultaneous addition of diborane and ammonia on the hot-filament assisted chemical vapor deposition of diamond*, Diamond Relat. Mater. **7** (1998), 35.

[70] I. Taher, . Aslam, M. A. Tamor, T. J. Potter, and R. C. Elder, *Piezoresistivme microsensors using p-type cvd diamond films*, Sens. Actuators, A **45** (1994), 35.

[71] S. Koizumi, K. Watanabe, M. Hasegawa, and H. Kanda, *Ultraviolet emission from a diamond pn junction*, Science **292** (2001), 1899.

[72] E. A. Ekimov, V. A. Sidorov, E. D. Bauer, N. N. Mel'nik, N. J. Curro, J. D. Thompson, and S. M. Stishov, *Superconductivity in diamond*, Nature **428** (2004), 542.

[73] R. Locher, C. Wild, N. Herres D. Behr, and P. Koidl, *Nitrogen stabilized* (100) *texture in chemical-vapor-deposited diamond films*, Appl. Phys. Lett. **65** (1994), 34.

[74] S. Bohr, R. Haubner, and B. Lux, *Influence of nitrogen additions on hot-filament chemical vapor deposition of diamond*, Appl. Phys. Lett. **68** (1996), 1075.

[75] R. G. Farrer, *On the substitutional nitrogen donor in diamond*, Solid State Commun. **7** (1969), 685.

[76] D. Saada, J. Adler, and R. Kalish, *Sulfur: a potential donor in diamond*, Appl. Phys. Lett. **77** (2000), 878.

[77] H. Zhou, Y. Yokoi, H. Tamura, S. Takami, M. Kubo, A. Miyamoto, N. M. Gamo, and T. Ando, *Quantum chemical calculations of sulfur doping reactions in diamond CVD*, Jap. J. Appl. Phys. **40** (2001), 2830.

[78] J. R. Petherbridge, P. W. May, G. M. Fuge, G. F. Robertson, K. N. Rosser, and M. N. R. Ashfold, *Sulfur doping of diamond films: Spectroscopic, electronic, and gas-phase studies*, J. Appl. Phys. **91** (2002), 3605.

[79] M. Hasegawa, T. Teraji, and S. Koizumi, *Lattice location of phosphorus in n-type homoepitaxial diamond films grown by chemical-vapor deposition*, Appl. Phys. Lett. **79** (2001), 3068.

[80] E. Gheeraert, S. Koizumi, T. Teraji, H. Kanda, and M. Nesládek, *Electronic states of boron and phosphorus in diamond*, Phys. Stat. Sol. (A) **174** (1999), 39.

[81] O. Gaudin, D. K. Troupis, R. B. Jackman, C. E. Nebel, S. Koizumi, and E. Gheeraert, *Charge-based deep level transient spectroscopy of*

phosphorous-doped homoepitaxial diamond, J. Appl. Phys. **94** (2003), 5832.

[82] Y. Koide, S. Koizumi, H. Kanda, M. Suzuki, H. Yoshida, N. Sakuma, T. Ono, and T. Sakai, *Admittance spectroscopy for phosphorus-doped n-type diamond epilayer*, Appl. Phys. Lett. **86** (2005), 232105.

[83] L. G. Wang and A. Zunger, *Phosphorus and sulphur doping of diamond*, Phys. Rev. B **66** (2002), 161202.

[84] Y. Yan, S. B. Zhang, and M. M. Al-Jassim, *Graphite-like surface reconstructions on c{111} and their implication for n-type diamond*, Phys. Rev. B **66** (2002), 201401.

[85] T. Teraji, S. Koizumi, S. Mita, A. Sawabe, and H. Kanda, *Electrical contacts for n-type diamond*, Jap. J. Appl. Phys. **38** (1999), L1096.

[86] T. Teraji, S. Koizumi, and H. Kanda, *Ga ohmic contact for n-type diamond by ion implantation*, Appl. Phys. Lett. **76** (2000), 1303.

[87] S. Koizumi, K. Watanabe, M. Hasegawa, and H. Kanda, *Formation of diamond p-n junction and its optical emission characteristics*, Diamond Relat. Mater. **11** (2002), 307.

[88] H. Kato, S. Yamasaki, and H. Okushi, *n-type doping of (001)-oriented single-crystalline diamond by phosphorus*, Appl. Phys. Lett. **86** (2005), 222111.

[89] T. Makino, N. Tokuda, H. Kato H, M. Ogura, H. Watanabe, S. G. Ri, S. Yamasaki, and H. Okushi, *High-efficiency excitonic emission with deep-ultraviolet light from (001)-oriented diamond p-i-n junction*, Jap. J. Appl. Phys. **45** (2006), L1042.

[90] S. A. Kajihara, A. Antonelli, J. Bernholc, and R. Car, *Nitrogen and potential n-type dopants in diamond*, Phys. Rev. Letters **66** (1991), 2010.

[91] C. Uzan-Saguy, C. Cytermann, B. Fizgeer, V. Richter, R. Brener, and R. Kalish, *Diffusion of lithium in diamond*, Phys. Stat. Sol. (A) **193** (2002), 508.

[92] R. Kalish, *The search for donors in diamond*, Diamond Relat. Mater. **10** (2001), 1749.

[93] Z. Teukam, J. Chevallier, C. Saguy, R. Kalish, D. Ballutaud, M. Barbe, F. Jomard F, A. Tromson-Carli, C. Cytermann, J. E. Butler, M. Bernard, C. Baron, and A. Deneuville, *Shallow donors with high n-type electrical conductivity in homoepitaxial deuterated boron-doped diamond layers*, Nature Materials **2** (2003), 482.

[94] J. Bardeen, *Surface states and rectification at a metal semi-conductor contact*, Phys. Rev. **71** (1947), 717.

[95] W. Schottky, *Vereinfachte und erweiterte Theorie der Randschicht-gleichrichter*, Z. Physik **118** (1942), 539.

[96] Y. Mori, H.Kawarada, and A. Hiraki, *Properties of metal/diamond interfaces and effects of oxygen adsorbed onto diamond surface*, Appl. Phys. Lett. **58** (1991), 940.

[97] T. Tachibana, B. E. Williams, and J. T. Glass, *Correlation of the electrical properties of metal contacts on diamond films with the chemical nature of the metal-diamond interface. II. Titanium contacts: A carbide-forming metal*, Phys. Rev. B **45** (1992), 11975.

[98] M. Itoh and H. Kawarada, *Fabrication and characterization of metal-semiconductor field-effect transistor utilizing diamond surface-conductive layer*, Jap. J. Appl. Phys. **34** (1995), 4677.

[99] H. Kawarada, M. Itoh, and Hokazono A, *Electrically isolated metal-semiconductor field effect transistors and logic circuits on homoepitaxial diamonds*, Jap. J. Appl. Phys. **35** (1996), L1165.

[100] A. Hokazono, T. Ishikura, K. Nakamura, S. Yamashita, and H. Kawarada, *Enhancement/depletion MESFETs of diamond and their logic circuits*, Diamond Relat. Mater. **6** (1997), 339.

[101] H. J. Looi, L. Y. S. Pang, M. D. Whitfield, J. S. Foord, and R. B. Jackman, *Progress towards high power thin film diamond transistors*, Diamond Relat. Mater. **8** (1999), 966.

[102] H. Umezawa, H. Taniuchi, T. Arima, M. Tachiki, and H. Kawarada, *Potential applications of surface channel diamond field-effect transistors*, Diamond Relat. Mater. **10** (2001), 1743.

[103] A. J. Tessmer, L. S Plano, and D. L. Dreifus, *High-temperature operation of polycrystalline diamond field-effect transistors*, IEEE Electron Dev. Lett. **14** (1993), 66.

[104] A. V. Denisenko, A. A. Melnikovand A. M. Zaitsev, V. I. Kurganskii, A. J. Shilovand, J. P. Gorban, and V. S. Varichenko, *p-type semiconducting structures in diamond implanted with boron ions*, Materials Science and Engineering **11** (1992), 273.

[105] A. Denisenko, W. R. Fahrner, U. Strahle, H. H. Henschel, and R. Job, *Radiation response of P-I-P diodes on diamond substrates of various type: Electrical properties of semiconductor-insulator homojunctions.*, IEEE Trans. Nucl. Sci. **43** (1996), 3081.

[106] N. Kawakami, Y. Yokota, T. Tachibana, K. Hayashi, K. Inoue, and K. Kobashi, *Fabrication of a submicron source-drain gap for p-i-p field effect transistors using epitaxial diamond layers*, Diamond Relat. Mater. **13** (2004), 1939.

[107] H. Shiomi, Y. Nishibayashi, N. Toda, and S. Shikata, *Pulse-doped diamond p-channel metal-semiconductor field-effect transistor*, IEEE Electron Dev. Lett. **16** (1995), 36.

[108] A. Vescan, P. Gluche, W. Ebert, and E. Kohn, *High-temperature, high-voltage operation of pulse-doped diamond MESFET*, IEEE Electron Dev. Lett. **18** (1997), 222.

[109] A. Aleksov, A. Denisenko, U. Spitzberg, T. Jenkins, W. Ebert, and E. Kohn, *Rf performance of surface channel diamond fets with sub-micron gate length*, Diamond Relat. Mater. **11** (2002), 382.

[110] H. Kawarada, Y. Araki, T. Saki, T. Ogawa, and H. Umezawa, *Electrolyte-solution-gate FETs using diamond surface for biocompatible ion sensors*, Phys. Stat. Sol. (A) **185** (2001), 79.

[111] J. A. Garrido, C. E. Nebel, M. Stutzmann, G. Rösel, R. Todt, M. C. Amann, E. Snidero, and P. Bergonzo, *Characterization of sub-micron in-plane devices in H-terminated diamond*, Phys. Stat. Sol. (A) **193** (2002), 517.

[112] M. Tachiki, H. Seo, T. Banno, Y. Sumikawa, H. Umezawa, and H. Kawarada, *Fabrication of single-hole transistors on hydrogenated diamond surface using atomic force microscope*, Appl. Phys. Lett. **81** (2002), 2854.

[113] T. Banno, M. Tachiki, Hokuto Seoa, H. Umezawa, and H. Kawaradaa, *Fabrication of diamond single-hole transistors using AFM anodization process*, Diamond Relat. Mater. **11** (2002), 387.

[114] F. J. Himpsel, J. A. Knapp, J. A. VanVechten, and D. E. Eastman, *Quantum photoyield of diamond (111) a stable negative-affinity emitter*, Phys. Rev. B **20** (1979), 624.

[115] H. B. Martin, A. Argoitia, J. C. Angus, A. B. Anderson, and U. Landau, *Boron-doped diamond electrodes for electrochemical applications*, Applications of Diamond Films and Related Materials: 3^{rd} International Conference (A. Feldmann, Y. Tzeng, W. A. Yarbrough, M. Yoshikawa, and M. Murakawa, eds.), NIST, Washington DC, 1995, p. 91.

[116] F. Bouamrane, A. Tadjeddine, J. E. Butler, R. Tenne, and C. Lévy-Clément, *Electrochemical study of diamond thin films in neutral and basic solutions of nitrate*, J. Electroanal. Chem. **405** (1996), 95.

[117] S. Wenmackers, P. Christiaens, W. Deferme, M. Daenen, K. Haenen, M. Nesládek, P. Wagner, V. Vermeeren, L. Michiels, M. vandeVen, M. Ameloot, J. Wouters, L. Naelaerts, and Z. Mekhalif, *Head-on immobilization of DNA fragments on CVD-diamond layers*, Materials Science Forum **492-493** (2005), 267.

[118] S. Wenmackers, S. D. Pop, K. Roodenko, V. Vermeeren, O. A. Williams, M. Daenen, O. Douhéret, J. DHaen, A. Hardy, M. K. Van Bael, K. Hinrichs, C. Cobet, M. vandeVen, M. Ameloot, K. Haenen, L. Michiels, N. Esser, and Patrick Wagner, *Structural and optical properties of DNA layers covalently attached to diamond surfaces*, Langmuir **24** (2008), 7269.

[119] W. G. Eversole, *Synthesis of diamond by deposition on seed crystals*, U.S. Patent No. 3,030,187 and 3,030,188, 1962.

[120] B. V. Derjaguin, D. V. Fedoseev, V. M. Lukyanovich, B. V. Spitzin, V. A. Ryabov, and A. V. Lavrentyev, *Filamentary diamond crystals*, J. Cryst. Growth **2** (1968), 380.

[121] S. Matsumoto, Y. Sato, M. Kamo, and N. Setaka, *Vapor deposition of diamond particles from methane*, Jap. J. Appl. Phys. **21** (1982), L183.

[122] S. Matsumoto, Y. Sato, M. Tsutsumi, and N. Setaka, *Growth of diamond particles from methane-hydrogen gas*, J. Mat. Sci. **17** (1982), 3106.

[123] M. Kamo, Y. Sato, S. Matsumoto, and N. Setaka, *Diamond synthesis from gas-phase in microwave plasma*, J. Cryst. Growth **62** (1983), 642.

[124] P. K. Bachmann, D. Leers, and H. Lydtin, *Towards a general concept of diamond chemical vapour deposition*, Diamond Relat. Mater. **1** (1991), 1.

[125] G. Binnig, H. Rohrer, C. Gerber, and E. Weibel, *Tunneling through a controllable vacuum gap*, Appl. Phys. Lett. **40** (1982), 178.

[126] G. Binnig, H. Rohrer, C. Gerber, and E. Weibel, *Surface studies by scanning tunneling microscopy*, Phys. Rev. Letters **49** (1982), 57.

[127] G. Binnig, H. Rohrer, C. Gerber, and E. Weibel, *7×7 reconstruction on Si(111)resolved in real space*, Phys. Rev. Letters **50** (1983), 120.

[128] P.K. Hansma and J. Tersoff, *Scanning tunneling microscopy*, J. Appl. Phys. **61** (1987), R1.

[129] J. A. stroscio, R. M. Feenstra, and A. P. Fein, *Electronic structure of the Si(111)* 2×1 *surface by scanning tunneling microscopy*, Phys. Rev. Letters **57** (1986), 2579.

[130] R. J. Hamers, R. M. Tromp, and J. E. Demuth, *Surface electronic structure of Si(111)-(7×7) resolved in real space*, Phys. Rev. B **34** (1986), 5343.

[131] H. Kawarada, H. Sasaki, and A. Sato, *Scanning-tunneling microscope observation of the homoepitaxial diamond (001)* 2×1 *reconstructions observed under atmospheric pressure*, Phys. Rev. B **52** (1995), 11351.

[132] P. B. Lukins, M. H. Zareie, and J. Khachan, *Atomic resolution structure of growth and etching patterns at the surface of microwave plasma chemical vapor deposited diamond films*, Appl. Phys. Lett. **78** (2001), 1520.

[133] R. E. Stallcup II and J. M. Perez, *Atomic structure of steps and defects on the clean diamond (100)*-2×1 *surface studied using ultrahigh vacuum scanning tunneling microscopy*, Appl. Phys. Lett. **81** (2002), 4538.

[134] K. Bobrov, A. J. Mayne, G. Comtet, G. Dujardin, L. Hellner, and A. Hoffman, *Atomic-scale visualization and surface electronic structure of the hydrogenated diamond C(100)-(*2×1*):H surface*, Phys. Rev. B **68** (2003), 195416.

[135] R. E Stallcup II and J. M Perez, *Scanning tunneling microscopy studies of temperature-dependent etching of diamond (100) by atomic hydrogen*, Phys. Rev. Letters **86** (2001), 3368.

[136] G. Binning, C. F. Quate, and C. Gerber, *Atomic force microscope*, Phys. Rev. Letters **56** (1986), 930.

[137] B. Rezek, C. Sauerer, J. A. Garrido, C. E. Nebel, and M. Stutzmann, *Scribing into hydrogenated diamond surfaces using atomic force microscopy*, Appl. Phys. Lett. **82** (2003), 3336.

[138] K. F. Brennan, *The physics of semiconductors with applications to optoelectronic devices*, Cambridge University Press, New York, 1999.

[139] P. P. Craig and V. Radeka, *Stress dependence of contact potential: The ac Kelvin method*, Rev. Sci. Instrum. **41** (1970), 258.

[140] Kelvin, *Contact electricity of metals*, Philos. Mag. **46** (1898), 82.

[141] I. D. Baikie and P. J. Estrup, *Low cost PC based scanning Kelvin probe*, Rev. Sci. Instrum. **69** (1998), 3902.

[142] I. D. Baikie, P. J. S. Smith, D. M. Porterfield, and P. J. Estrup, *Multitip scanning bio-Kelvin probe*, Rev. Sci. Instrum. **70** (1999), 1842.

[143] I. R. Peterson, *Kelvin probe liquid-surface potential sensor*, Rev. Sci. Instrum. **70** (1999), 3418.

[144] S. Hamma and P. R. i Cabarrocas, *Determination of the mobility gap of microcrystalline silicon and of the band discontinuities at the amorphous microcrystalline silicon interface using in situ Kelvin probe technique*, Appl. Phys. Lett. **74** (1999), 3218.

[145] S. W. Howell, *Electrostatic force microscopy studies of nanoscale systems*, Ph.D. thesis, Purdue University, 2001.

[146] J. M. R. Weaver and D. Abraham, *High-resolution atomic force microscopy potentiometry*, J. Vac. Sci. Technol. B **9** (1991), 1559.

[147] R. Wiesendanger, *Scanning probe microscopy and spectroscopy*, Cambridge University Press, New York, 1994.

[148] J. W. Hong, K. H. Noh, S. Park, S. Kwun, and Z. Khim, *Surface charge density and evolution of domain structure in triglycine sulfate determined by electrostatic-force microscopy*, Phys. Rev. B **58** (1998), 5078.

[149] T. D. Krauss and L.E. Brus, *Charge, polarizability, and photoionization of single semiconductor nanocrystals*, Phys. Rev. Letters **83** (1999), 4840.

[150] D. Schaadt, E. Yu, S. Sankar, and A. Berkowitz, *Charge storage in Co nanoclusters embedded in SiO_2 by scanning force microscopy*, Appl. Phys. Lett. **74** (1999), 472.

[151] J. Jones, P. Bridger, O. Marsh, and T. McGill, *Charge storage in CeO_2/Si/CeO_2/Si(111) structures by electrostatic force microscopy*, Appl. Phys. Lett. **75** (1999), 1326.

[152] M. Nonnenmacher, M. P. O'Boyle, and H. K. Wickramasinghe, *Kelvin probe force microscopy*, Appl. Phys. Lett. **58** (1991), 2921.

[153] C. H. Lei, A. Das, M. Elliott, and J. E. Macdonald, *Conductivity of macromolecular networks measured by electrostatic force microscopy*, Appl. Phys. Lett. **83** (2003), 482.

[154] S. C. Fain Jr, K. A. Barry, M. G. Bush, B. Pittenger, and R. N. Louie, *Measuring average tip-sample forces in intermittent-contact (tapping) force microscopy in air*, Appl. Phys. Lett. **74** (2000), 930.

[155] D. Sarid, *Scanning force microscopy*, Oxford University Press, 1994.

[156] Y. Martin, D. W. Abraham, and H. K. Wickramasinghe, *High-resolution capacitance measurement and potentiometry by force microscopy*, Appl. Phys. Lett. **52** (1988), 1103.

[157] J. R. Matey and J. Blanc, *Scanning capacitance microscopy*, J. Appl. Phys. **57** (1985), 1437.

[158] P. Muralt and D. W. Pohl, *Scanning tunneling potentiometry*, Appl. Phys. Lett. **48** (1986), 514.

[159] C. Ballif, H. R. Moutinho, and M. M. Al-Jassim, *Cross-sectional electrostatic force microscopy of thin-film solar cells*, J. Appl. Phys. **89** (2001), 1418.

[160] M. Drndić, R. Markov, M. V. Jarosz, M. G. Bawendi, M. A. Kastner, N. Markovic, and M. Tinkham, *Imaging the charge transport in arrays of CdSe nanocrystals*, Appl. Phys. Lett. **83** (2003), 4008.

[161] M. Tachiki, Y. Kaibara, Y. Sumikawa, M. Shigeno, H. Kanazawa, T. Banno, K. S. Song, H. Umezawa, and H. Kawarada, *Characterization of locally modified diamond surface using Kelvin probe force microscope*, Surf. Sci. **581** (2005), 207.

[162] B. Rezek and C. E. Nebel, *Kelvin force microscopy on diamond surfaces and devices*, Diamond Relat. Mater. **14** (2005), 466.

[163] C. Toma, A. Volodin, G. Bogdan, W. Deferme, K. Haenen, M. Nesládek, and C. Van Haesendonck, *Tip voltage controlled local modification of hydrogenated diamond surface with an atomic force microscope*, Phys. Stat. Sol. (A) **204** (2007), 2920.

[164] A. Volodin, C. Toma, G. Bogdan, W. Deferme, K. Haenen, M. Nesládek, and C. Van Haesendonck, *Electrostatic force microscopy mapping of electrical conductivity of hydrogen-terminated diamond films*, Appl. Phys. Lett. **91** (2007), 142111.

[165] L. F. Thompson, C. G. Willson, and M. J. Bowden, *Introduction to microlithography*, American Chemical Society, Washington, 1983.

[166] D. J. Elliott, *Integrated circuit fabrication technology*, McGraw-Hill, New York, 1989.

[167] W. M. Moreau, *Semiconductor lithography: Principles, practices and materials*, Plenum Press, New York, 1998.

[168] IBM, *IBM research demonstrates path for extending current chip-making technique*, 2006.

[169] E. J. Van Leonen, D. Dijkkamp, A.J. Hoeven, J.M. Lenssinck, and J. Dieleman, *Direct writing in Si with a scanning tunneling microscope*, Appl. Phys. Lett. **55** (1989), 1312.

[170] S. Xu and G. Y. Liu, *Nanometer-scale fabrication by simultaneous nanoshaving and molecular self-assembly*, Langmuir **13** (1997), 127.

[171] B. A. Wacaser, M. J. Maughan, I. A. Mowat, T. L. Niederhauser, M. R. Linford, and R. C. Davies, *Chemomechanical surface patterning and functionalization of silicon surfaces using an atomic force microscope*, Appl. Phys. Lett. **82** (2003), 808.

[172] J. F. Liu, J. R. Von Her, C. Baur, R. Stallcup, J. Randall, and K. Bray, *Fabrication of high-density nanostructures with an atomic force microscope*, Appl. Phys. Lett. **84** (2004), 1359.

[173] R. D. Piner, J. Zhu, F. Xu, S. H. Hong, and C. A. Mirkin, *Dip-pen nanolithography*, Science **283** (1999), 661.

[174] S. Ginger, H. Zhang, and C. A. Mirkin, *The evolution of dip-pen nanolithography*, Angew. Chem. Int. Ed. **43** (2004), 30.

[175] E. W. Müller, *Abreißen adsorbierter Ionen durch hohe elektrische Feldstärken*, Naturwissenshaften **29** (1941), 533.

[176] M. Lutwyche, C. Andreoli, G. Binnig, J. Brugger, U. Drechsler, W. Haeberle, H. Rohrer, H. Rothuizen, and P. Vettiger, *Microfabrication and parallel operation of 5×5 2D AFM cantilever arrays for data storage and imaging*, Proc. IEEE **MEMS98** (1998), 8.

[177] B. W. Chui, T. D. Stowe, T. W. Kenny, H. J. Mamin, B. D. Terris, and D. Rugar, *Low-stiffness silicon cantilevers for thermal writing and piezoresistive readback with the atomic force microscope*, Appl. Phys. Lett. **69** (1996), 2767.

[178] R. P. Ried, H. J. Mamin, B. D. Terris, L. S. Fan, and D. Rugar, *6-MHz 2-N/m piezoresistive atomic-force-microscope cantilevers with incisive tips*, J. Microeletromech. Syst. **6** (1997), 294.

[179] H. P. Lang, R. Berger, C. Andreoli, J. Brugger, M. Despont, P. Vettiger, Ch. Gerber, J. K. Gimzewski, J. P. Ramseyer, E. Meyer, and H. J. Guntherodt, *Sequential position readout from arrays of micromechanical cantilever sensors*, Appl. Phys. Lett. **72** (1998), 383.

[180] H. Sugimura, T. Uchida, N. Kitamura, and H. Masuhara, *Scanning tunneling microscope tip-induced anodization for nanofabrication of titanium*, J. Phys. Chem. **98** (1994), 4352.

[181] J. A. Dagata, J. Schneir, H. H. Harary ans C. J. Evans, M. T. Postek, and J. Bennett, *Modification of hydrogen-passivated silicon by a scanning tunneling microscope operating in air*, Appl. Phys. Lett. **56** (1990), 2001.

[182] H. C. Day and D. R. Allee, *Selective area oxidation of silicon with a scanning force microscope*, Appl. Phys. Lett. **62** (1993), 2691.

[183] M. Yasutake, Y. Ejiri, and T. Hattori, *Modification of silicon surface using atomic force microscope with conducting probe*, Jap. J. Appl. Phys. **32** (1993), L1021.

[184] E. S. Snow and P. M. Campbell, *Fabrication of Si nanostructures with an atomic-force microscope*, Appl. Phys. Lett. **64** (1994), 1932.

[185] T. Hattori, Y. Ejiri, K. Saito, and M. Yasutake, *Fabrication of nanometer-scale structures using atomic force microscope with conducting probe*, J. Vac. Sci. Technol. A **12** (1994), 2586.

[186] N. Kramer, *Nanolithography on silicon*, Ph.D. thesis, University of Twente, 1996.

[187] S. C. Minne, H. T. Soh, Ph. Flueckiger, and C. F. Quate, *Fabrication of 0.1μm metal oxide semiconductor field-effect transistors with the atomic force microscope*, Appl. Phys. Lett. **66** (1995), 703.

[188] E. S. Snow and P. M. Campbell, *AFM fabrication of sub-10-nanometer metal-oxide devices with in-situ control of electrical-properties*, Science **270** (1995), 1639.

[189] K. Matsumoto, S. Takahashi, M. Ishii, M. Hoshi, S. Ichimura A. Kurokawa, and A. Ando, *Application of STM nanometer-size oxidation process to planar-type MIM diode*, Jap. J. Appl. Phys. **34** (1995), 1387.

[190] K. Matsumoto, *STM/AFM nano-oxidation process to room-temperature-operated single-electron transistor and other devices*, Proc. IEEE **85** (1997), 612.

[191] J. Shirakashi, K. Matsumoto, N. Miura, and Makoto Konagai, *Single-electron transistors (SETs) with Nb/Nb oxide system fabricated by atomic force microscope (AFM) nano-oxidation process*, Jap. J. Appl. Phys. **36** (1997), L1257.

[192] R. Garcia, M. Calleja, and F. Pérez-Murano, *Local oxidation of silicon surfaces by dynamic force microscopy: Nanofabrication and water bridge formation*, Appl. Phys. Lett. **72** (1998), 2295.

[193] R. Held, T. Vancura, T. Heinzel, K. Ensslin, M. Holland, and W. Wegscheider, *In-plane gates and nanostructures fabricated by direct oxidation of semiconductor heterostructures with an atomic force microscope*, Appl. Phys. Lett. **73** (1993), 262.

[194] R. Held, S. Lüscher, T. Heinzel, K. Ensslin, and W. Wegscheider, *Fabricating tunable semiconductor devices with an atomic force microscope*, Appl. Phys. Lett. **75** (1999), 1134.

[195] Y. Gotoh, K. Matsumoto, and T. Maeda, *Room temperature coulomb diamond characteristic of single electron transistor made by AFM nano-oxidation process*, Jap. J. Appl. Phys. **41** (2002), 2578.

[196] Y. Takemura and J. Shirakashi, *AFM lithography for fabrication of magnetic nanostructures and devices*, J. Magn. Magn. Materials **304** (2006), 19.

[197] M. Tachiki, T. Fukuda, K. Sugata, H. Seo, H. Umezawa, and H. Kawarada, *Control of adsorbates and conduction on CVD-grown diamond surface, using scanning probe microscope*, Appl. Surf. Sci. **159-160** (2000), 578.

[198] K. Sugata, M. Tachiki, T. Fukuda, H. Seo, and H. Kawarada, *Nanoscale modification of the hydrogen-terminated diamond surface using atomic force microscope*, Jap. J. Appl. Phys. **41** (2002), 4983.

[199] M. Ishibashi, S. Heike, and T. Hashizume, *Combining atomic force microscopic lithography with photolithography*, Jap. J. Appl. Phys. **39** (2000), 7060.

[200] E. J. Bae, E. R. Kim, and H. Lee, *Nano-patterning of polythiophene derivatives containing electron transporting moiety by using AFM lithography*, J. Korean Phys. Soc. **37** (2000), 1026.

[201] W. Lee, Y. Oh, E. R. Kim, and H. Lee, *Nanopatterning of self-assembled monolayers on Si-surfaces with AFM lithography*, Synth. Met. **117** (2001), 305.

[202] L. J. van der Pauw, *A method of measuring specific resistivity and Hall effect of discs of arbitrary shape*, Philips Res. Rep. **13** (1958), 1.

[203] J. A. Garrido, T. Heimbeck, and M. Stutzmann, *Temperature-dependent transport properties of hydrogen-induced diamond surface conductive channels*, Phys. Rev. B **71** (2005), 245310.

[204] C.E. Nebel, F. Ertl, C. Sauerer, M. Stutzmann, C.F.O. Graeff, P. Bergonzo, O.A. Williams, and R.B. Jackman, *Low temperature properties of the p-type surface conductivity of diamond*, Diamond Relat. Mater. **11** (2002), 351.

[205] W.L. Wang, K.J. Liao, and B.B. Wang, *Magnetoresistance effect of p-type diamond films in various doping levels at different temperatures*, Diamond Relat. Mater. **9** (2000), 1612.

[206] Y. Mori, H. Yagi, M. Deguchi, T. Sogi, Y. Yokota, N. Eimori, H. Yagyu, H. Ohnishiand, M. Kitabatake1, K. Nishimura, A. Hatta, T. Ito, T. Hirao, T. Sasaki, and A. Hiraki, *Characterization of homoepitaxial diamond films grown from carbon monoxide*, Jap. J. Appl. Phys. **32** (1993), 4661.

[207] M. Malfait, *Magnetic and transport properties of $Ga_{1-x}Mn_xAs$ diluted magnetic semiconductors*, Ph.D. thesis, Katholieke Universiteit Leuven, 2005.

[208] W. Deferme, K. Haenen, G. Tanasa, C. F. Flipe, and M. Nesládek, *Compositional and electrical characterization of the hydrogen-oxygen terminated diamond (100) surface*, Phys. Stat. Sol. (A) **203** (2006), 3114.

[209] R. E. Thomas, R. A. Rudder, and R. J. Markunas, *Atomic hydrogen adsorption on the reconstructed diamond (100)-*(2×1) *surface*, J. Chem. Vap. Depos. **1** (1992), 6.

[210] M. Cannaerts, M. Nesládek, Z. Remes, C. Van Haesendonck, and L. M. Stals, *Scanning tunneling microscopy and spectroscopy of non-doped hydrogen terminated CVD diamond*, Phys. Stat. Sol. (A) **181** (2000), 77.

[211] M. Cannaerts, M. Nesládek, K. Haenen, L. De Schepper, L. M. Stals, and C. Van Haesendonck, *Influence of annealing on the electronic properties of chemical vapor deposited diamond films studied by high vacuum scanning tunneling microscopy and spectroscopy*, Diamond Relat. Mater. **11** (2002), 212.

[212] A. J. Mayne and G. Dujardin, *STM characterization of hydrogenated diamond surfaces*, New Diamond Front. Carbon Technol. **15** (2005), 265.

[213] L. Hellner, A. J. Mayne, R. Bernard, and G. Dujardin, *Hydrogenated diamond crystal C(100) conductivity studied by STM*, Diamond Relat. Mater. **14** (2005), 1529.

[214] Sung-Gi Ri, H. Watanabe, M. Ogura, D. Takeuchi, S. Yamasaki, and H. Okushi, *Hydrogen plasma etching mechanism on (001) diamond*, J. Cryst. Growth **293** (2006), 311.

[215] A. Podesta‘, M. Salerno, V. Ralchenko, M. Bruzzi, S. Sciortino, R. Khmelnitskii, and P. Milani, *An atomic force microscopy study of the effects of surface treatments of diamond films produced by chemical vapor deposition*, Diamond Relat. Mater. **15** (2006), 1292.

[216] R.E. Rawles, S.F. Komarov, R. Gat, W.G. Morris, J.B. Hudson, and M.P. D'Evelyn, *Mechanism of surface smoothing of diamond by a hydrogen plasma*, Diamond Relat. Mater. **6** (1997), 791.

[217] J. Ristein, F. Maier, M. Riedel, J. B. Cui, and L. Ley, *Surface electronic properties of diamond*, Phys. Stat. Sol. (A) **181** (2000), 65.

[218] J. Ristein, F. Maier, M. Riedel, M. Stammer, and L. Ley, *Diamond surface conductivity experiments and photoelectron spectroscopy*, Diamond Relat. Mater. **10** (2001), 416.

[219] O. A. Williams, M. D. Whitfield, R. B. Jackman, J. S. Foord, J. E. Butler, and C. E. Nebel, *Carrier generation within the surface region of hydrogenated thin film polycrystalline diamond*, Diamond Relat. Mater. **10** (2001), 423.

[220] K. Haenen, J. F. Rouleau, M. Nesládek, J. Goyette, L. M. Stals, and T. K. Bose, *Dielectric measurements on oxidized and hydrogenated chemical vapor deposited diamond films*, J. Appl. Phys. **91** (2002), 6670.

[221] D. Bonnell, *Scanning probe microscopy and spectroscopy: Theory, techniques, and applications*, Wiley-VCH, New York, 2000.

[222] J. Colchero, A. Gil, and A. M. Baro, *Resolution enhancement and improved data interpretation in electrostatic force microscopy*, Phys. Rev. B **64** (2001), 245403.

[223] B. Rezek and C. E. Nebel, *Electronic properties of plasma hydrogenated diamond surfaces: A microscopic study*, Diamond Relat. Mater. **15** (2006), 1374.

[224] P. E. Viljoen, E. S. Lambers, and P. H. Holloway, *Reaction between diamond and titanium for ohmic contact and metallization adhesion layers*, J. Vac. Sci. Technol. B **12** (1994), 2997.

[225] A. Hoffmann, S. Prawer, and R. Kalish, *Structural transformation of diamond induced by 1-keV ar-ion irradiation as studied by auger and secondary-electron spectroscopies and total-secondary-electron-yield measurements*, Phys. Rev. B **45** (1992), 12736.

[226] K. P. Loh, X. N. Xie, Y. H. Lim, E. J. Teo, J. C. Zheng, and T. Ando, *Surface oxygenation studies on (100)-oriented diamond using an atom beam source and local anodic oxidation*, Surf. Sci. **505** (2002), 93.

[227] M. W. Xu, T. Hantschel, and W. Vandervorst, *Reliable 2-D carrier profiling with SSRM on INP-based devices*, Proceedings of the 2001 International Conference on Indium Phosphide and Related Materials, Nara, Japan, 2001, p. 541.

[228] J. Osterman, A. Hallén, and S. Anand, *Carrier profiling of Al-doped 4H-SiC by scanning spreading resistance microscopy*, Appl. Phys. Lett. **81** (2002), 3004.

[229] R. S. Gi, K. Tashiro, S. Tanaka, T. Fujisawa, H. Kimura, T. Kurosu, and M. Iida, *Hall effect measurements of surface conductive layer on undoped diamond films in* NO_2 *and* NH_3 *atmospheres*, Jap. J. Appl. Phys. **38** (1999), 3492.

[230] N. Mott, *The electrical properties of liquid mercury*, Philos. Mag. **13** (1966), 989.

[231] N. Mott, M. Pepper, S. Pollitt, R. H. Wallis, and C. J. Adkins, *The Anderson transition*, Proc. Roy. Soc. (London) A **345** (1975), 169.

[232] B. L. Altshuler, D. Khmel'nitzkii, A. I. Larkin, and P. A. Lee, *Magnetoresistance and Hall effect in a disordered two-dimensional electron gas*, Phys. Rev. B **22** (1980), 5142.

[233] G. Bergmann, *Electron scattering by electron holograms: The physical interpretation of the Coulomb anomaly in disordered electron systems*, Phys. Rev. B **35** (1987), 4205.

[234] P. W. Anderson, *Absence of diffusion in certain random lattices*, Phys. Rev. **109** (1958), 1492.

[235] A. Kawabata, *Theory of negative magnetoresistance in three-dimensional systems*, Solid State Commun. **34** (1980), 431.

[236] B. L. Altshuler and A. G. Aronov, *Electron-electron interactions in disordered conductors*, Electron-electron interactions in disordered systems (A. L. Efros and M. Pollak, eds.), vol. 10, North-Holland, Amsterdam, 1985, p. 1.

[237] B. L. Altshuler and D. E. Khmelnitskiĭ, *Fluctuation properties of small conductors*, Sov. Phys. J.E.T.P. Lett. **42** (1985), 359.

Publications

1. C. Toma, A. Volodin, G. Bogdan, W. Deferme, K. Haenen, M. Nesládek, and C. Van Haesendonck, *Tip voltage controlled local modification of hydrogenated diamond surface with an atomic force microscope*, Phys. Stat. Sol. A **204(9)**, 2920 (2007).
2. A. Volodin, C. Toma, G. Bogdan, W. Deferme, K. Haenen, M. Nesládek, and C. Van Haesendonck, *Electrostatic force microscopy study of electrical conductivity of hydrogen-terminated CVD diamond films*, Phys. Stat. Sol. A **204(9)**, 2915 (2007).
3. A. Volodin, C. Toma, G. Bogdan, W. Deferme, K. Haenen, M. Nesládek, and C. Van Haesendonck, *Electrostatic force microscopy mapping of electrical conductivity of hydrogen-terminated diamond films*, Appl. Phys. Lett. **91**, 14211 (2007).

Curriculum Vitae

Cristina Toma
Born on 12 November 1977 in Abrud, Romania

1992-1996 Studies in Mathematics-Physics, Horea, Cloşca şi Crişan High School, Abrud, Romania

1996-2001 B.Sc. studies in Physics, Babeş-Bolyai University, Cluj-Napoca, Romania
Diploma: "Ultrasound propagation velocity in K_2SO_4 and Na_2SO_4 solutions"

2001-2002 M.Sc. studies in Physics, University of Oradea, Romania
Dissertation: "Spectroscopic and magnetic studies of some Cu (II) complexes in beta-dicetone"

2002-2008 Ph.D. studies in Physics, Laboratory of Solid-State Physics and Magnetism, Katholieke Universiteit Leuven, Belgium
Thesis: "Nanoscale characterization and modification of the electronic properties of hydrogen terminated diamond surfaces"